Multifunctional Iron and Gold Nanostructures for biomedical applications

Sara C. Freitas
Mestrado em Física Médica
Departamento de Física e Astronomia
2020/21

Orientador
Doutor João H. Belo, Faculdade de Ciências da Universidade do Porto e IFIMUP

Coorientador
Doutora Célia Sousa, Faculdade de Ciências da Universidade do Porto e IFIMUP

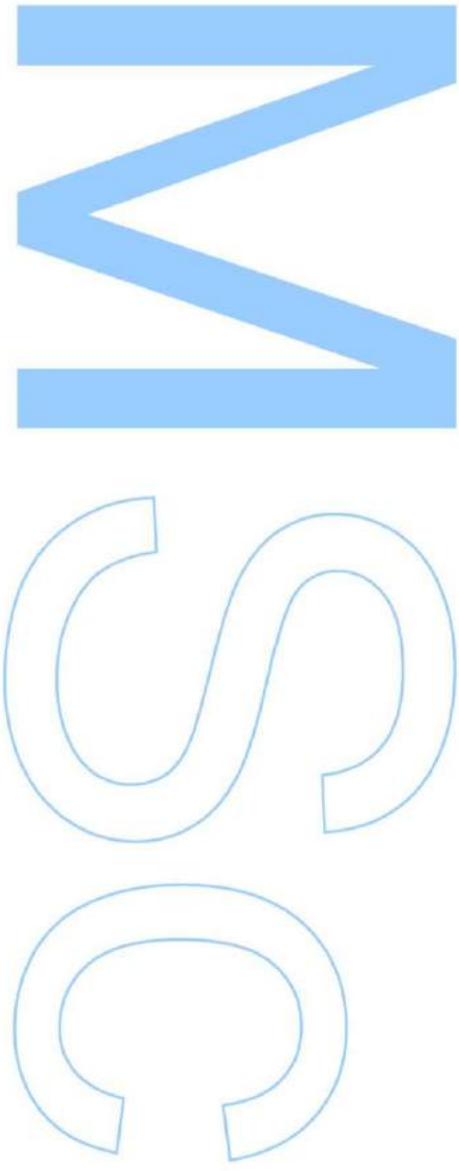

U.PORTO

FACULDADE DE CIÊNCIAS
UNIVERSIDADE DO PORTO

Todas as correções determinadas pelo júri, e só essas, foram efetuadas.

O Presidente do Júri,

Porto, _____/_____/_____

UNIVERSIDADE DO PORTO

MASTERS THESIS

Multifunctional Iron and Gold Nanostructures for Biomedical Applications

Author:
Sara C. FREITAS

Supervisor:
Doutor João H. BELO

Co-supervisor:
Doutora Célia SOUSA

A thesis submitted in fulfilment of the requirements
for the degree of MSc. Medical Physics

at the

Faculdade de Ciências da Universidade do Porto
Departamento de Física e Astronomia

December 6, 2021

"Out of clutter, find simplicity. From discord, find harmony. In the middle of difficulty lies opportunity"

Albert Einstein

Acknowledgements

Em primeiro lugar tenho de agradecer ao meus orientadores Doutor João Horta e Doutora Célia Sousa, pelo voto de confiança, companheirismo, dedicação e oportunidades proporcionadas ao longo deste ano. Sem dúvida que me tornaram numa pessoa mais confiante, proativa e com vontade de continuar a melhorar enquanto pessoa e jovem investigadora. Da mesma forma agradeço à minha familia e amigos que sempre me apoiaram e deram força nos momentos mais difíceis. Agradeço também à Ana, ao Miguel à Andreia, pela companhia e ajuda em tudo o que precisei ao longo deste trabalho.

UNIVERSIDADE DO PORTO

Abstract

Faculdade de Ciências da Universidade do Porto
Departamento de Física e Astronomia

MSc. Medical Physics

Multifunctional Iron and Gold Nanostructures for Biomedical Applications

by Sara C. FREITAS

Cancer is one of the leading causes of death in Europe accounting for about 20% of deaths on that continent. In recent years, hyperthermia emerged as a promising treatment approach in oncology consisting in raising the temperature of cancer cells to 40-45ºC to reach apoptosis i.e., programmed cell death. One way to reach local and controlled hyperthermia is via functionalizable nanostructures that are activated by external stimuli, such as magnetic fields or electromagnetic radiation. In this context, gold nanostructures (Au-NS) have been the subject of attention in the academic and clinical environment, due to their biocompatibility and high absorption of electromagnetic radiation in the near-infrared range caused by its surface plasmon resonance. In parallel, magnetic nanostructures based on iron (Fe-NS) have also been gaining attention, since they can combine the diagnostic (as contrast agents for MRI) and therapy (magnetic hyperthermia) properties. Although Fe-oxide NS are the most reported in the literature, Fe-NS are a promising alternative, since its high magnetic moment can improve the heat dissipation phenomena produced by the magnetic hysteresis, due to the irreversible magnetization/demagnetization processes induced by an applied alternating magnetic field.

The primary goal of this work was to combine the "best of both worlds" producing multifunctional Iron-Gold nanostructures (Fe-Au-NS) with high heating performance when stimulated with radiation (500-1000 nm) and with alternating magnetic fields, for applications in controlled and localized hyperthermia. The nanostructures were produced through the ablation of Iron and Gold targets with a femtosecond pulsed laser in liquids (ethanol, acetone and ultra-pure water). The technique proved to be effective regarding the production of spherical-shaped nanoparticles particularly in the thin-film

targets ablation case that allowed the synthesis of nanoparticles composed simultaneously by the two elements. The Fe-Au-NS have been characterized with scanning electron microscopy (SEM), UV-Vis spectral analysis and superconducting quantum interference device (SQUID) techniques.

The second part of this work included a detailed analysis of the heating performance of gold nanorods (AuNRs) during exposure to NIR radiation. Throughout the experiments several parameters were taken into account, including the laser output power, laser spot area, AuNRs concentration and the volume of the aqueous solution in which the latter were suspended. Measurements were acquired using a continuous wave laser operating at 808 nm, aligned to focus on the AuNR solution. The NR dimensions were 41 nm in length and 10 nm in diameter. The ratio between these dimensions is approximately 4, thus corresponding to the ideal proportion to have maximum absorption in the wavelength of this laser. The photo-induced heating tests revealed, in all cases, a significant increase of temperature in solutions containing the nanorods, when compared to just an aqueous solution irradiated under the same conditions. It was also verified that, regardless of the used concentration, the maximum reached temperature was similar. Finally, the laser output power proved to the key parameter regarding the heating of the sample.

Keywords: Magnetic hyperthermia, photothermal therapy, gold nanorods, iron nanoparticles, core-shell, nanostructures, laser ablation in liquids, femtosecond, theranostic, cancer

UNIVERSIDADE DO PORTO

Resumo

Faculdade de Ciências da Universidade do Porto
Departamento de Física e Astronomia

Mestrado em Física Médica

Nanoestruras multifuncionais de Ferro e Ouro para aplicações biomédicas

por Sara C. FREITAS

O cancro é uma das principais doenças causadoras de morte na Europa, sendo responsável por cerca de 20% das mortes nesse continente. Nos últimos anos, a hipertermia surgiu como uma abordagem de tratamento promissora em oncologia, que consiste em elevar a temperatura das células cancerigenas até 40-45ºC para atingir a apoptose, ou seja, morte celular programada. Uma forma de alcançar a hipertermia local e controlada é através de nanoestruturas funcionalizáveis que são ativadas por estímulos externos, tais como campos magnéticos ou radiação eletromagnética. Neste contexto, as nanoestruturas de ouro têm sido alvo de atenção no meio académico e clínico, devido à sua biocompatibilidade e alta absorção de radiação eletromagnética na faixa próxima ao infravermelho, causada pela ressonância plasmónica de superfície. Em paralelo, nanoestruturas magnéticas à base de ferro também sido alvo atenção dado que podem combinar as propriedades diagnósticas (como agentes de contraste em ressonância magnética) e terapêuticas (em hipertermia magnética). Apesar do óxido de Ferro ser o elemento mais relatado na literatura, o Ferro aparenta ser uma alternativa promissora dado que seu momento magnético pode melhorar os fenómenos de dissipação de calor produzidos pela histerese magnética, devido aos processos irreversíveis de magnetização/desmagnetização induzidos pela aplicação de um campo magnético alternado.

O principal objetivo deste trabalho foi combinar o "melhor dos dois mundos" produzindo nanoestruturas multifuncionais de Ferro-Ouro (Fe-Au-NS) com alto desempenho de aquecimento quando estimulados com radiação (500-1000nm) e com campos magnéticos alternados, para aplicações na hipertermia controlada e localizada. As nanoestruturas foram produzidas através da ablação de alvos de Ferro e Ouro, com um laser pulsado

de femtossegundos, numa solução liquida (etanol, acetona e água ultrapura). A técnica mostrou-se eficaz na produção de nanopartículas de formato esférico, principalmente no caso de ablação de alvos de filmes-finos. O último permitiu a síntese de nanopartículas compostas simultaneamente pelos dois elementos.

A segunda parte deste trabalho incluiu uma análise detalhada do desempenho de aquecimento de nanorods de ouro, durante a sua exposição à radiação próxima do infravermelho. Ao longo das experiências efetuadas, vários parâmetros foram considerados, incluindo a potência e área do spot do laser, a concentração de nanorods e o volume da solução aquosa em que os últimos se encontram suspensos. As medições foram feitas recorrendo a um laser contínuo que opera nos 808 nm, alinhado de modo a incidir lateralmente na solução aquosa com nanofios de ouro, cujas dimensões são 41 nm de comprimento e 10 nm de diâmetro. A razão entre essas dimensões é aproximadamente 4, correspondendo desta forma à proporção ideal para ter o máximo de absorção no comprimento de onda deste laser. Os testes de aquecimento revelaram, em todos os casos, um aumento significativo de temperatura nas soluções com nanofios quando comparadas a apenas uma solução aquosa irradiada nas mesmas condições. Foi também verificado que, independentemente da concentração utilizada, a temperatura máxima atingida foi semelhante e a potência do laser revelou-se como o parâmetro chave no aquecimento global da amostra.

Palavras-Chave: Hipertermia magnética, terapia fototérmica, nanofios de ouro, nanopartículas de ferro, core-shell, nanoestruturas, ablação laser em líquidos, femtosegundo, cancro

Contents

List of Figures

List of Tables

Chapter 1

Introduction

The aging and growth of the population has been leading to a rapidly growing incidence of cancer and mortality worldwide. Only for the year of 2018, WHO (World Health Organization) predicted 18.1 million new cases and 9.6 million deaths [1].

Although cancer is one of the leading causes of death, the treatment options are limited. Radiotherapy remains one of the main therapy strategies due to its proven ability to kill cells and shrink tumors through the irreparable damage induced in the DNA of injured cells by ionizing radiation [2]. However, the efficiency of radiotherapy also depends on the healthy surrounding tissues whose radiation exposure should be avoided in order to provide the patient an improved quality of life in the medium and long term future [3].The recent radiotherapy techniques aim to reduce the dose in adjacent tissues while holding the therapeutic dose to the tumor, but the dose typically has to be reduced below the curative level to spare vital surrounding tissue [2, 3].

A method to specifically deliver the dose to the cancerous tissue would be beneficial and therefore biomedical research has been devoted to this subject in order to kill and control tumors at cellular level, resorting to targets or markers that are able to identify and selectively attach to tumor cells, allowing a more localized treatment with a significant reduction of the induced secondary effects on healthy tissues. Nanotechnology plays a key role in both biotechnology and medicine disciplines since it provides new approaches to overcome the limitations of conventional medicine and the use of nanometric materials, is currently an prominent topic with a wide range of applications for medical diagnosis and treatment [4]. Nanostructures are particles that have at least one dimension in the nanometer size range, up to $\sim$100 nm, and are categorized by high surface-area-to-volume ratio. Progress in nanotechnology field, particularly in the nanoparticle (NP) research

area, has allowed the synthesis of NPs with precise morphology with the possibility to modify particle surfaces and manipulating their characteristics for precise applications [3, 5] .

1.1 Magnetic nanostructures and their biomedical applications

Generally, magnetic nanostructures (MNS) are classified in three major categories: pure metals, metal oxides and magnetic nanocomposites. In the biomedical field, the most popular ones are Co, Fe, Ni, iron oxides and some ferrites. Among them, iron oxide nanoparticles, usually Fe_3O_4 or Fe_2O_3, are one of the most reported due to their zero remanence. In other words, this means that these iron oxide MNS only exhibit magnetic moment during the application of the external magnetic field [6] . This concept will be explained later in Chapter 2, but briefly it consists in an important requirement as it prevents the structures from agglomerating when dispersed in a solution.

Among all nanomaterials with biomedical applications, MNS are one of the most frequently used due to their nontoxicity, biocompatibility and the fact that, when placed in the desired location and combined with an external magnetic field, they can interact with the local environment and perturb it by delivering heat. Beyond hyperthermia, that will be individually discussed in chapter 3, these magnetic nanostructures can be employed in order to achieve different purposes, namely as a tool to separate and purify cell populations, as contrast agents in magnetic resonance imaging (MRI) or for cellular therapy with cell labeling and targeting [6, 7] .

1.1.1 Cell manipulation and separation

An efficient isolation of specific cells from heterogeneous populations is essential in multiple areas like cell and molecular biology, biochemistry, immunology and clinical research. Until this moment different cell isolation techniques have been developed, being the filtration, density gradient centrifugation and sedimentation the standard procedures. Yet, these procedures are not always effective as they mainly depend on characteristics like the density or size of the cells. What I mean is, in the event of different cells having similar sizes or densities, these techniques would not be able to perform an efficient separation. Hence, other methods, who resort to magnetic nanostructures, should overcome this problem. If a nonmagnetic matrix is filled with magnetic nanoparticles with specific

antibodies for the surface of the target cells, the required cells of the heterogeneous population will be attached to the magnetic nanoparticles and therefore, efficiently isolated by applying an external magnetic field [6] .

1.1.2 Contrast agents in MRI

MRI is a non-invasive diagnostic technique whose fundamental principle involves the precession of nuclear magnetic moments of a given sample that is under the influence of an external magnetic field. These magnetic moments, once randomly oriented, tend to align themselves in the direction of the applied magnetic field, leading to the generation of a net magnetization called longitudinal magnetization [6] .

The longitudinal magnetization is tipped out of alignment through the application of a properly adjusted radiofrequency pulse, originating a transverse magnetization component. Removing the radio frequency pulse, the process of relaxation begins and both components of the magnetization return to their previous states, only in the presence of the applied magnetic field. The relaxation process leads to the production of a weak RF signal that is detected and subsequently processed in order to produce an image [6].

The MRI technique has several advantages, including the use of non-ionizing radiation, high spatial resolution and great anatomic detail but its major drawback is the limited sensitivity of its probes [6]. Hereupon, contrast agents are often employed in order to enhance imaging sensitivity, increasing the contrast of the acquired images to facilitate the distinction between different tissues. Although in clinical practice the most used contrast agents are Gd^{3+}-complexes they have raised toxicity concerns and therefore superparamagnetic iron oxides nanoparticles (SPIONs) have been developed as a viable alternative [6, 8] . Being superparamagnetic, such nanoparticles are restricted by the superparamagnetic limit, implying a maximum diameter per particle in order to maintain zero remanance, fundamental property that prevents particles' aggregation in absence of magnetic field. These nanostructures have various advantages, such as biocompatibility, ability to be metabolized, relatively high saturation magnetic moments and easiness of surface functionalization [6, 7].

1.1.3 Cell labeling and targeting

The current chemotherapy treatments can be successful for certain types of cancer. However, they also present major drawbacks such as the lack of sufficient selectivity and

limited bioaccessibility of drugs to the tumor and the frequent emergence of multiple drug resistance. Hereupon the drug attacks both target and non-target cells causing toxicity to healthy tissues and the limited bioaccessibility of drugs to the tumor tissues demands higher drug doses.

Such problems demanded for a new delivery system, and in this regard, nanoparticles as targeted carriers of drugs are being developed as alternative non-biological carriers to overcome the limitations of the current treatment regimen [9, 10].

Magnetic nanoparticles parameters like material, size, shape or surface coating can determine if they are adequate to be manipulated for a specific purpose. For example the size determines if the MNP can get through barriers, such as blood vessel walls or cell membranes to the required area. This way, and adding the fact that the drugs are usually loaded on the particles' surface, the targeted approach is achieved on one hand by the magnetic materials that act as carriers, and on another by the surface coating molecules that recognizes and attaches to another molecule which is specific to the disease area [11].

Due to their specific magnetic properties, the MNPs can be precisely placed in a desired location by applying magnetic field and furthermore, MNPs are being developed for hyperthermia and heat-activated drug release as a result of their heating ability in high-frequency magnetic fields [4, 6].

Chapter 2

Magnetism Overview

In order to understand some fundamental concepts and processes that will be mentioned along this work, it is important to make a magnetism overview. Hereupon this chapter includes a brief description of the different magnetic behaviors in the macro and nanoscale and the heat dissipation mechanisms associated with magnetic losses in the form of thermal energy.

Electrons, in atoms, are negatively charged particles that have an intrinsic spin and an associated magnetic moment. Typically these moments are macroscopically summed to zero since they are randomly oriented in the absence of an applied magnetic field. When an external magnetic field, **H**, is applied to a material, there is a change in its magnetic dipoles leading to a macroscopic moment ordering and consequently a non-zero net magnetization, **M**. Magnetic induction, **B**, is the result of the material's magnetization itself and the applied external field. The relationship between these three fields **(B, H** and **M)** is given by the equation below, where μ_0 is vacuum permeability equal to $4\pi \times 10^{-7}$ H/m [12]:

$$\mathbf{B} = \mu_0(\mathbf{H} + \mathbf{M}) \tag{2.1}$$

The materials can be divided into different magnetism classes according to the orientation and behavior of their magnetic moments in the presence of the external magnetic field. These classes are: diamagnetic, paramagnetic, ferromagnetic, antiferromagnetic and ferrimagnetic. The concept of magnetic susceptibility, which is the degree of the material's magnetization response to an applied magnetic field, is useful in order to differentiate the different magnetic behaviors [12]. The magnetic susceptibility, χ_m, is a dimensionless constant defined as:

$$\chi_m = \frac{M}{H} \tag{2.2}$$

Magnetic susceptibility is measured resorting to magnetometers and its measurement is done by changing the intensity of an applied magnetic field while measuring the material's magnetization isothermally, M(H) measurements. These measurements are performed at constant temperature. The magnetic susceptibility is temperature dependent and its effect will be individually detailed for each magnetic behavior.

The relative permeability, μ_r, which is the ratio of the permeability in a material to the permeability in the vacuum, μ_0, is represented as:

$$\mu_r = \frac{\mu}{\mu_0} \tag{2.3}$$

and it is related to the magnetic susceptibility as follows [13]:

$$\chi_m = \mu_r - 1 \tag{2.4}$$

2.1 Magnetic Properties

The magnetic properties of magnetic nanostructures can be generally classified into intrinsic and extrinsic. The intrinsic properties result from interactions on an atomic length scale and are determined by chemical composition and crystal structure being independent of grain size, shape, and microstructure. On the other hand, extrinsic properties result from long-range interactions and are dependent on the microstructural factors [14]. The intrinsic magnetic properties include the saturation magnetization, the Currie temperature and the magnetocrystalline anisotropy. The saturation magnetization,M_S, is described as the maximum magnetization quantity (induced magnetic moment) of a certain material, which can be obtained at temperatures below the Curie Temperature (T$<$ T_C) when exposed to a sufficiently large magnetic field. Thus, the magnitude of Ms is considered as a function of temperature, M_S(T). In its turn, Curie temperature, T_C, corresponds to the temperature at which certain magnetic material withstand a great change in their magnetic susceptibility, leading to loss of intrinsic magnetization [14]. Lastly, magnetic anisotropy is defined as the dependency of magnetic properties on a preferred crystallographic direction. In other words, it is the energy required to deflect the magnetic moment in a single crystal from the easy to the hard direction of magnetization and

is given by:

$$E(\theta) = K_{eff} V \sin^2(\theta) \tag{2.5}$$

where K_{eff} is the anisotropic constant and θ is the angle between the magnetization and an easy axis (Figure 2.1). The energy barrier, E_A, between two easy axis corresponds to the product of the material anisotropic constant, K, and the domain volume, V [15].

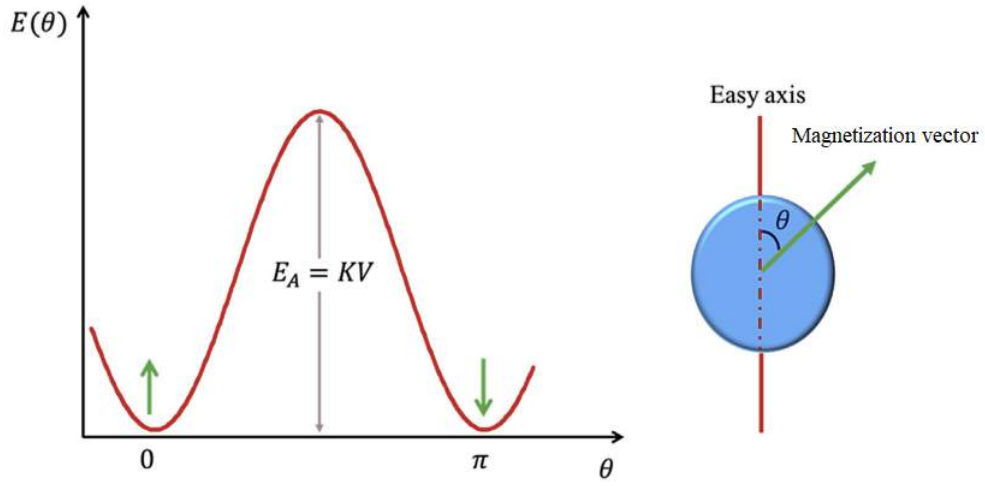

FIGURE 2.1: Schematic illustration of the energy curve versus θ, the angle between the magnetization vector and an easy axis. Adapted from [15].

The extrinsic magnetic properties include the coercivity and remnant magnetization. Remnant magnetization corresponds to a residual magnetization value where the material remains magnetized, i.e. its magnetization is non-zero, without application of an external field and coercivity is associated with the field value required to achieve null magnetization [14]. Both of these properties will be discussed in the next sections .

2.2 Macromagnetism

This section is dedicated to the different magnetic behaviors found in bulk materials when under the influence of an external magnetic field. These behaviors are categorized as diamagnetic, paramagnetic, ferromagnetic, antiferromagnetic and ferrimagnetic.

2.2.1 Diamagnetism

Diamagnetism is a very weak type of magnetism that is induced by a change in the orbital motion of electrons due to an applied magnetic field. This form of magnetism is

non-permanent, persisting only under the influence of the applied external magnetic field. The magnitude of the induced magnetic moment is very small with opposite direction to the applied field (Figure 2.2) [13]. The relative permeability values of diamagnetic materials are slightly less than one ($\mu < 1$), and their magnetic susceptibility is negative [16]. Some examples of diamagnetic compounds are water, silver, mercury and bismuth.

2.2.2 Paramagnetism

Paramagnetism occurs primarily in materials whose atoms possess a permanent magnetic dipole moment. In the absence of an external magnetic field, these magnetic moments are randomly oriented leading to no net macroscopic magnetization. The influence of an external magnetic field tends to guide the moments in its direction, giving rise to a relative permeability slightly bigger than one ($\mu >1$), and to a relatively small but positive magnetic susceptibility. Hereupon, paramagnetic materials are weakly attracted to magnets and in addition, they do not retain any magnetization at zero magnetic field. Paramagnetic materials, like the diamagnetic ones, only exhibit magnetization in the presence of an external field [13]. Some examples include aluminum, **gold**, and copper.

The magnetic susceptibility, is dependent on the applied magnetic field and temperature, as:

$$\chi_m = \frac{M}{H} = \frac{C}{T} \tag{2.6}$$

where C is the Curie constant of the material and T the temperature [16]. By analyzing equation 2.6 it is noticeable that the susceptibility increases inversely proportional with the magnetic field and decreases with increasing temperature.

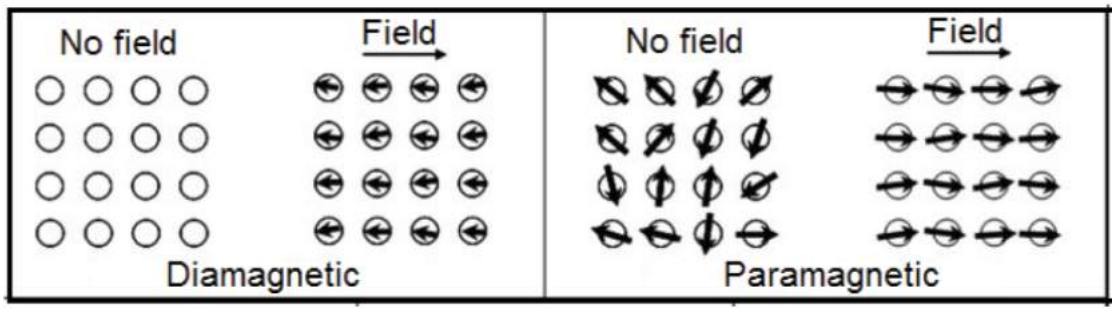

FIGURE 2.2: Magnetic behavior of diamagnetic and paramagnetic materials without and in the presence of an applied external magnetic field [17].

2.2.3 Ferromagnetism

Ferromagnetic materials possess a permanent magnetic moment, even in the absence of an external field, and exhibit very large saturation magnetization. The spontaneous magnetization can be several orders of magnitude bigger than the applied magnetic field, causing ferromagnetic materials to have very high permeabilities. When the external magnetic field is removed, a part of the induced domain alignment can be preserved causing the body to act as a permanent magnet [13].

Spontaneous magnetization results on the alignment of uncompensated electron spins by the strong quantum mechanical "exchange" force. In a molecule, covalent bonding causes the electrons' wave-function to overlap between atoms, which means that electrons have a non-zero probability of exchange its position with another electron of the molecule. Exchange interaction is a purely quantum-mechanical phenomenon as it affects electrons in an atom or in close-neighbor atoms. When the exchange interaction affects close-neighbor atoms it is referred to as direct exchange. Examples of ferromagnetic elements are **Iron**, Cobalt and Gadolinium.

2.2.3.1 Hysteresis loop

Ferromagnetic materials, at temperatures below T_C, are composed of multiple small-volume regions called domains, in which there is an alignment in the same direction of all magnetic moments (Figure 2.3). Adjacent domains are separated by domain boundaries or Bloch walls, across which the direction of magnetization gradually changes. Although each domain is magnetized, the material as a whole will have zero magnetization so that, in order to give the material a net magnetization, one direction must predominate in all domains.

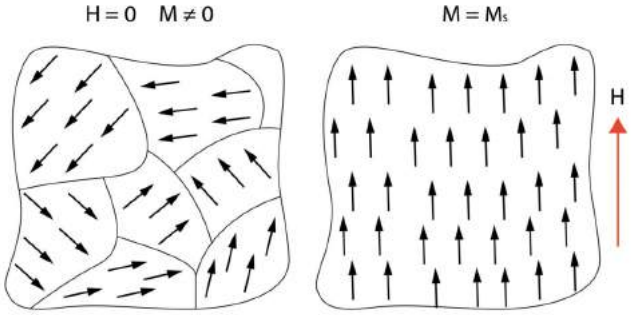

FIGURE 2.3: Schematic illustration of the magnetic domains and the spin orientations in zero and externally applied magnetic field H [18].

When a ferromagnetic material is magnetized in one direction, it will not relax back to zero magnetization simply by removing the applied magnetic field. It must be driven back to zero by applying a field in the opposite direction. If a magnetic field is varied from a maximum positive to its symmetric negative value and then back to its maximum positive value, its magnetization will trace out a loop called a hysteresis, that represents the irreversible behavior of M as a function of H.

By applying a field to an initially demagnetized material, it will follow the dotted curve until reaching a constant level called saturation magnetization (M_S) (Figure 2.4). This means that the magnetic moments, of a multi-domain ferromagnetic material, that are parallel to the applied magnetic field will grow, whereas the others will shrink when exposed to an applied magnetic field [15]. Reducing the field from this value, M decreases slowly following a different path, given by the arrow, up to a residual magnetization value given for a null field called remanant magnetization (M_R), where the material remains magnetized without application of field. Inverting the direction of the field, the curve follows the same direction until M becomes null for a given field value called coercive field (H_C). If we continue to vary the module of the field we will again reach a region of saturation and repeating the cycle in the opposite direction we obtain a closed curve which is called the hysteresis [19, 20].

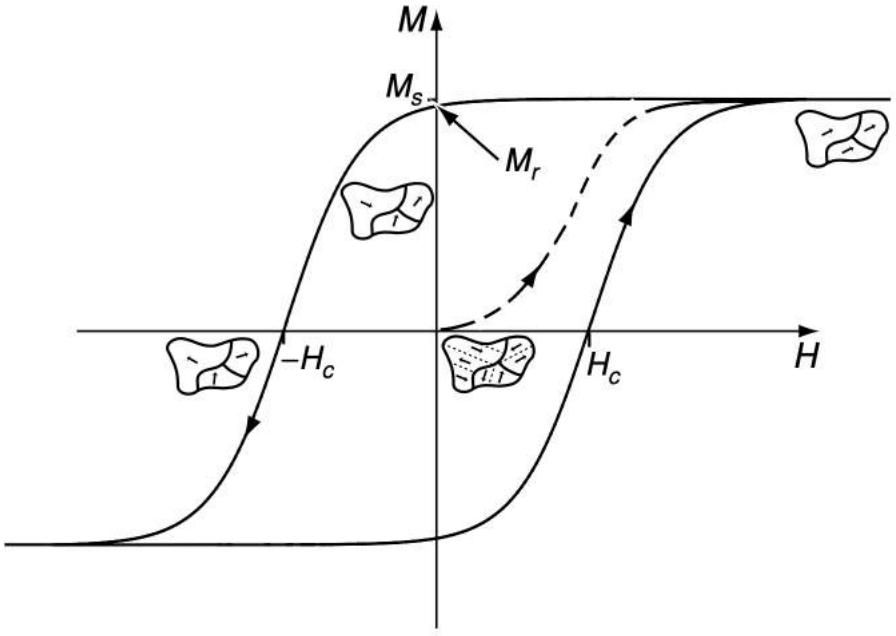

FIGURE 2.4: Hysteresis loop of a ferromagnetic material. Adapted from [20].

2.2.3.2 Temperature effect

The spontaneous magnetization coming from the alignment of the atomic magnetic moments depends on temperature, in a way that it falls hastily to zero at the Curie temperature (Figure 2.5). At temperatures above T_C, the ferromagnetic order collapses and the material becomes paramagnetic, so that the susceptibility follows the Curie–Weiss law given by:

$$\chi_m = \frac{C}{T - T_C} \tag{2.7}$$

The Curie temperatures of the ferromagnetic metals, **iron**, cobalt and nickel, are $1044K$, 1388 K and 628 K, respectively, being cobalt the known single-element with the highest Curie temperature [20]. The susceptibility and permeability of ferromagnetic materials are both large and positive [16].

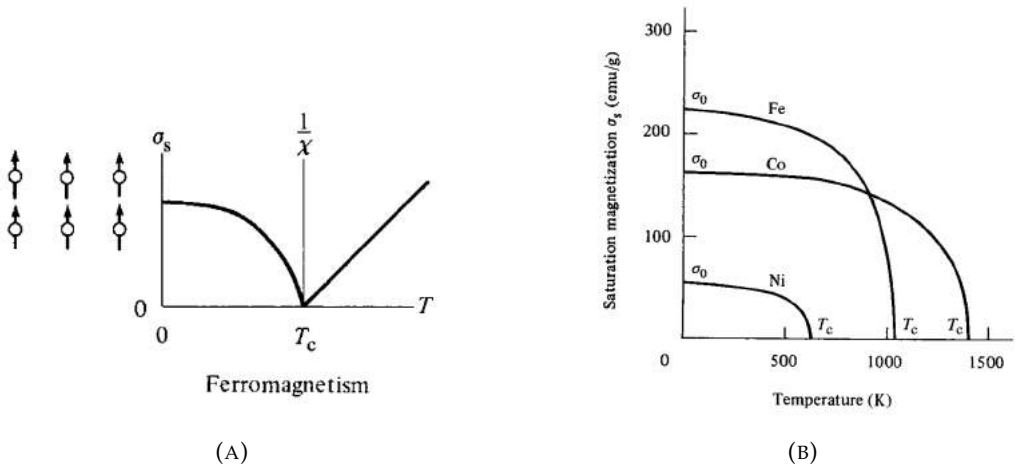

(A) (B)

FIGURE 2.5: (A) Magnetization and susceptibility curves below and above the Curie temperature, Tc, for ferromagnetic materials. (B) Saturation magnetization of iron, cobalt, and nickel as a function of temperature [16].

2.2.4 Antiferromagnetism

The characteristic spontaneous magnetization coming from the parallel alignment of the magnetic moments of a ferromagnetic material is not the only type of magnetic order. In an antiferromagnetic material, the atomic moments form two equivalent but with opposite directions magnetic sublattices. Examples of antiferromagnetic materials are hematite (Fe_2O_3), chromium and nickel oxide.

Antiferromagnetic substances, have a small positive susceptibility and a permeability slightly bigger than one ($\mu > 1$) at all temperatures. The dependence on the temperature is given by the equation below:

$$\chi_m = \frac{C}{T - T_N} \tag{2.8}$$

where T_N is a maximum critical temperature called the Néel temperature. The susceptibility increases with the temperature until this critical point, and above T_N, similarly to ferromagnets, the antiferromagnets follow the Curie–Weiss behavior becoming paramagnetic [16, 20].

2.2.5 Ferrimagnetic

Ferrimagnetic materials, like ferromagnetics, are composed of magnetically saturated domains, exhibit a substantial spontaneous magnetization at room temperature and present magnetic saturation and hysteresis [16]. When under the influence of an applied magnetic field, the moments align themselves, some parallel, as in ferromagnetism, and others antiparallel, as in antiferromagnetism (Figure 2.6) [21]. Their spontaneous magnetization also disappears above a critical temperature, T_C, becoming paramagnetic. The most important ferrimagnetic substances are certain double oxides of iron and ferrites

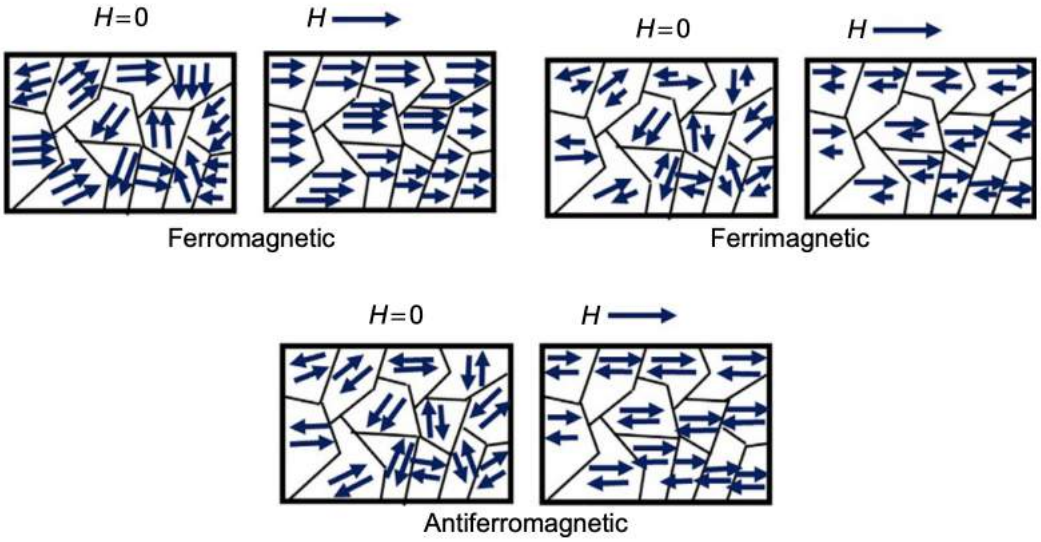

FIGURE 2.6: Different types of magnetic behavior for ferromagnetic, ferrimagnetic and antiferromagnetic materials [21].

2.3 Nanomagnetism

This section is dedicated to the magnetic behavior found in ferromagnetic nanoparticles, covering their features when reduced below a critical size and the associated finite-size and temperature effects.

2.3.1 Single Domain and Superparamagnetism

The domain structure of a ferromagnetic material is influenced by the size, being the two most studied finite-size effects in nanoparticles the single domain and superparamagnetic limits [22]. As previously mentioned, "large" ferromagnetic particles have a multidomain structure with regions of uniform magnetization separated by domain walls. However, when the particle is reduced to a critical size, the formation of a domain wall is not energetically favorable and the particle becomes a single domain. This means that there is a critical volume below which it costs more energy to create a domain wall than to support the external magnetostatic energy of the single-domain state. The critical diameter,D_C, for spherical particles typically lies in the range of a few tens of nanometers depending on the material and it is given by:

$$D_c = 18\frac{\sqrt{AK_{eff}}}{\mu_0 M_s^2} \tag{2.9}$$

where A is the exchange constant, K_{eff} is the anisotropy constant, μ_0 the vaccum permeability and M_s the saturation magnetization [5].

Material	D_c (nm)
fcc Co	7
Ni	55
Fe_3O_4	128
Fe	**15**

TABLE 2.1: Estimated single-domain size for different spherical particles [5]

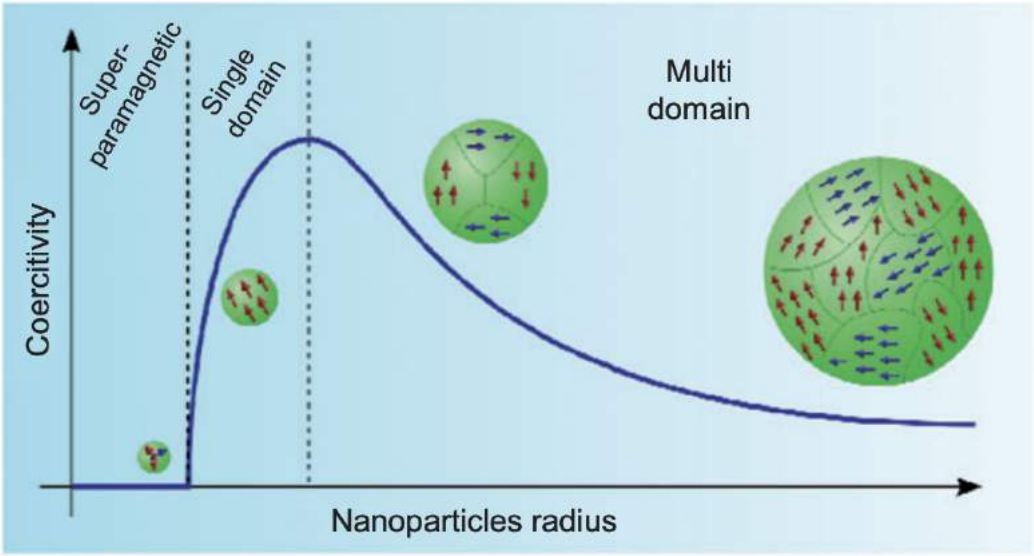

FIGURE 2.7: Schematic illustration of the coercivity-size relation for nanoparticles [22].

In terms of response to an applied alternating magnetic field, a ferromagnetic material describes an hysteresis loop, characterized by two parameters called remanence and coercivity. The coercivity is related to the width of the curve and it is strongly size-dependent (Figure 2.8). As the particle size is reduced, the coercivity decreases toward zero as shown in Figure 2.7 and such particles become superparamagnetic. The remanent magnetization, in its turn, can be described as a residual magnetism "left behind" in ferromagnetic materials when the external magnetic field is removed.

The superparamagnetic behavior can be beneficial over ferromagnetism for some biomedical applications, as superparamagnetic NPs show an insignificant coercivity and remanence at room temperature offering the advantage of reduced risk of particle aggregation [23, 24].

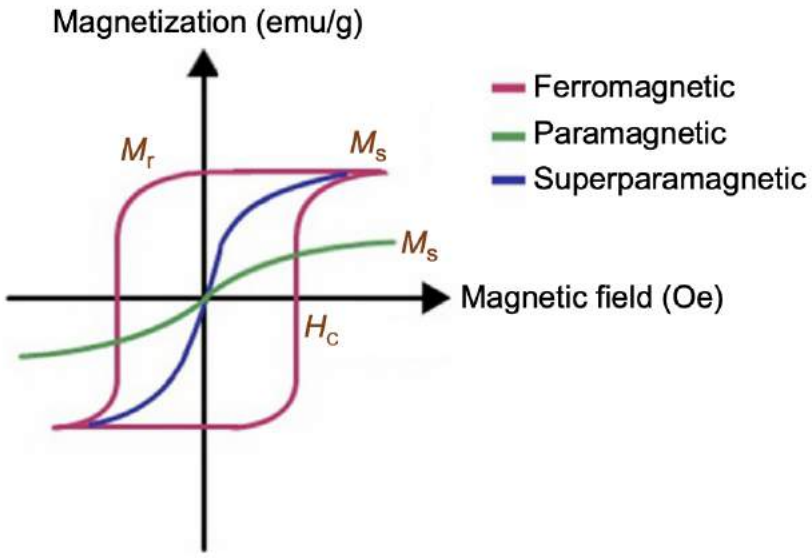

FIGURE 2.8: Hysteresis curve magnetization of ferromagnetic, paramagnetic, and superparamagnetic particles [21].

2.3.2 Temperature effects

The different behavior of magnetic nanoparticles can be explained by comparing two limit cases regarding the thermal energy, K_BT, and the magnetic anisotropic energy, E_A. In the first, if $E_A >> K_BT$, the orientation of the magnetic moment is "fixed" to the easy axis of the ferromagnetic particle and, if the particle is free to rotate, the particle and the magnetic moment align with the magnetic field [15, 25].

The reduction of the NP size leads to a decrease in the anisotropy energy and for a particle size inferior to a critical value, it may become lower than the thermal energy. This leads to the second limit case, $E_A << K_BT$, where the thermal energy exceeds the energy barrier that separates two energetically equivalent easy directions of magnetization. In this case, for sufficiently small nanoparticles, the magnetization can randomly flip its direction under the influence of temperature and the nanoparticles are superparamagnetic. Here the external magnetic field is capable to magnetize the superparamagentic NPs, but their magnetic susceptibility is much larger in comparison to paramagnets. [13, 15, 25].

In the case of a noninteracting single-domain nanoparticle with uniaxial magnetic symmetry, the relaxation time, τ, is given by the Arrhenius law:

$$\tau = \tau_0 e^{\frac{K_{eff}V}{K_BT}} \tag{2.10}$$

where τ_0 is on the order of 10^{-9}s. Depending on the context, this equation is also known as the Néel–Brown relaxation law [5, 26].

2.4 Heat Dissipation Mechanisms

The application of an alternating magnetic field on magnetic particles causes the dissipation of magnetic energy in the form of thermal energy, and the magnetic losses are associated with the magnetization/demagnetization cycling. This energy converted into heat during magnetization reversal is caused by different processes that occur in the particle system: hysteresis losses, Néel or Brown relaxation and eddy currents. The contribution of each mechanism depends on MNP size, magnetic anisotropy and fluid viscosity.

2.4.1 Eddy currents

Eddy currents are based on Faraday law of induction, which states that a potential difference is induced in a material subject to a temporal variation of magnetic field flux. The induced voltage is proportional to the rate of change over time of the magnetic flux. Therefore, when a material is under the influence of an alternating magnetic field, a voltage will be induced in it producing circular currents called Eddy currents. These currents will react back, by creating a magnetic field whose direction is such that counteracts the external magnetic flux variation, wasting magnetic energy as heat. The Eddy current loss is given by the equation:

$$PE = Ef^2 H_{max} d^2 \tag{2.11}$$

where E is the eddy current coefficient, f is the frequency, H_{max} is the maximum flux density, and d is the particle size. Since PE increases with d^2, the eddy current heating becomes negligible on the nanoscale range. [15, 27].

2.4.2 Magnetic Hysteresis

When multi-domain ferromagnetic NPs are exposed to an applied magnetic field, all the magnetic moments tend to align in its direction. The magnetic domains whose moments are parallel to the magnetic field will grow, whereas the others will shrink in a way that saturation magnetization (M_S) is reached. As previously mentioned, the magnetization is associated with an irreversible displacement of the domain walls and when the

magnetic field is removed, the magnetization does not completely disappears, retaining a remanent value (M_R). These remanence and the coercive field are the origin of hysteresis behavior in magnetic materials.

The energy change per hysteretic cycle is proportional to the hysteresis loop area and to the field frequency, as:

$$P = \mu_0 f \oint M\,dH \tag{2.12}$$

where μ_0 and f are, respectively, vacuum magnetic permeability and applied frequency [15].

2.4.3 Néel and Brown Relaxation

For single domain NPs, under the superparamagnetic behavior, the magnetic induction heating has a significant contribution of both Néel relaxation and Brownian motion. In the Néel relaxation mechanism, the physical position of MNP is kept fixed, while the spin rotates and orients parallelly to the applied field (Figure 2.9). The Néel relaxation time, τ_N, is described using the equation:

$$\tau_N = \frac{\tau_0}{2}\sqrt{\pi\frac{K_B T}{KV}}e^{\frac{KV}{K_B T}} \tag{2.13}$$

where τ_0, the relaxation time, is on the order of 10^{-9}s, K and V are, respectively, the anisotropy constant and volume of the MNP, and K_B is the Boltzmann constant and T the absolute temperature [15].

Brownian motion refers to the rotation of the magnetic particle as a whole because of the torque exerted on the magnetic moment by the external AC magnetic field (Figure2.9). The Brownian relaxation time, τ_B, is described using the equation:

$$\tau_B = \frac{3\eta V_H}{K_B T} \tag{2.14}$$

where, η is the viscosity of the surrounding medium, V_H is the particle hydrodynamic volume, that includes the magnetic core, coating and hydration layers, K_B is the Boltzmann constant and T the absolute temperature [15].

Both Neél and Brownian mechanisms occur simultaneously for particles so that the total relaxation losses, τ_{eff}, due to both processes can be calculated by the following equation:

$$\frac{1}{\tau_{eff}} = \frac{1}{\tau_N} + \frac{1}{\tau_B} \tag{2.15}$$

The power generation consequent of magnetization change in an AC magnetic field is displayed in equation:

$$P = \pi \mu_0 \chi_0 H_0^2 f \frac{2\pi f \tau_{eff}}{1 + (2\pi f \tau_{eff})^2} \tag{2.16}$$

where μ_0 is the vacuum permeability, χ_0 is the magnetic susceptibility, H_0 is the external magnetic field amplitude and f is the external magnetic field frequency [28]. By analyzing the previous equation it is noticeable that the power generation is proportional to the frequency and to the square of field strength.

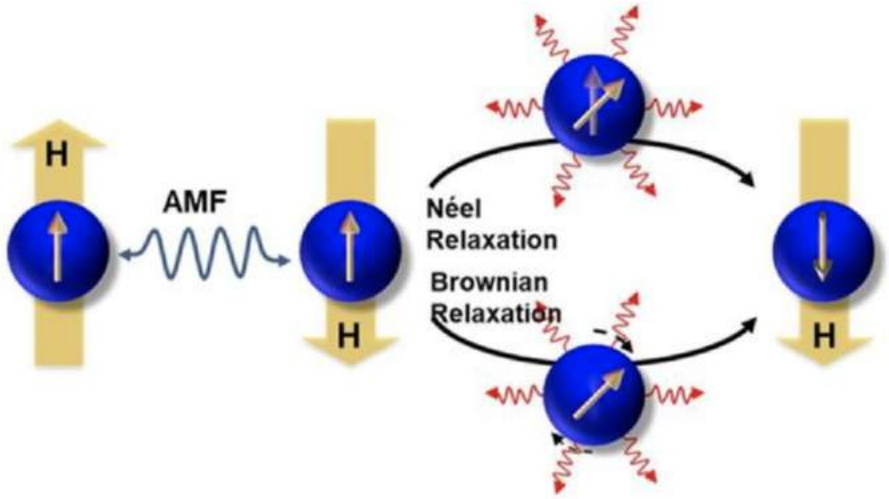

FIGURE 2.9: Néel and Brownian relaxation mechanisms [29].

Chapter 3

Hyperthermia as form of treatment

As previously mentioned, the conventional cancer treatment methods such as radiotherapy, chemotherapy and surgery have many limitations and an efficient method for localized cancer therapy is still desired [30]. In this context, hyperthermia emerged as a promising treatment approach in oncology consisting in artificially raising the temperature of cancer cells to 40-45ºC to reach apoptosis i.e., programmed cell death [31].

Along with thermal ablation, hyperthermia can be regarded as one of the specific subtypes of thermal therapy. In its core, hyperthermia is the process in which the temperature is raised a few degrees above physiological level, usually lasting between 15 to 60 minutes. Thermal ablation, in its turn, requires extreme temperatures (above 45 ºC) for direct damage or destruction of the tumor tissues [32].

The conventional hyperthermia, that involves an external source that creates a temperature gradient with a maximum value on the body's surface that promptly decreases with distance, has several disadvantages not only because the energy is dissipated in the healthy tissues located between the surface and the tumor, but also due to the fact that there is no differentiation between targeted and the surrounding normal tissues (Figure 3.1). The nanotechnology development significantly contributed to an appropriate way for heat delivery and one way to reach local and controlled hyperthermia is via functionalizable nanostructures that are activated by **external stimuli**, such as **magnetic fields** or **electromagnetic radiation** (Figure 3.1). In this context, considering the "Inside-out hyperthermia", the nanoparticles concentrated inside the tumor can absorb the energy coming from various external sources to enhance locally the effects of hyperthermia [30].

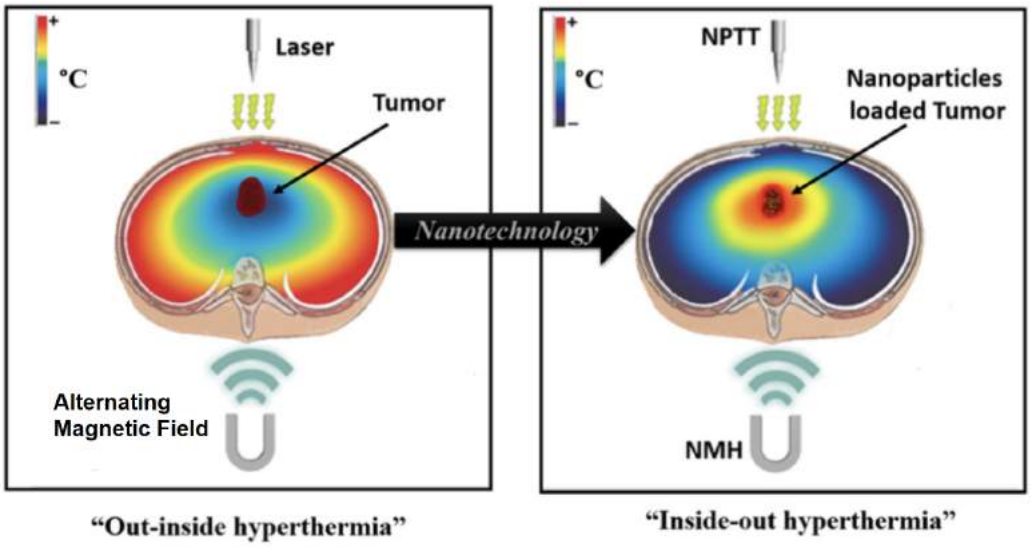

FIGURE 3.1: "Out-inside" and "Inside-out" hyperthermia; Abbreviations: NPTT: NanoPhotoThermal Therapy; NMH: NanoMagnetic Hyperthermia; Adapted from [30].

A breakthrough in the application of magnetic nanostructures for cancer therapy was accomplished by Scarberry *et al* that pointed out the possibility of tagging cancer cells with magnetic nanoparticles, that were functionalized with a receptor-specific ligand, by transporting them to different parts of the body under the influence of an applied magnetic field [33]. Another method that employs nanoparticles for cancer therapy is known as hyperthermia-mediated drug release. In the latter, the ability of MNS to generate heat upon magnetic stimulation is explored to detached a chemo-drug from the nanoparticle and an intracellular chemo-drug release is achieved [33].

In addition, the hyperthermia treatment can also act as a complementary therapy to the conventional methods. Considering that the oxygen is a universal radio sensitizer that enhances the biological effect of radiation and that, in tumors, hypoxia corresponds to a slow reduction in tissue oxygenation that is directly related to tumor growth, the elevation of the tissues' temperature promotes a change in the vascular permeability and an increase in the blood flow that eventually leads to tumor re-oxygenation where the cytotoxic effects will be intensified. In other words, the hyperthermia treatment can act as an adjuvant therapy for cancer by reducing the tissue hypoxia and therefore making it more susceptible when concomitantly applied with radiation or anti-cancer drugs. A review published by Jaber Beik *et al* report that several clinical experiments for different kinds of tumors demonstrated that the use of hyperthermia as a complement to radiotherapy or chemotherapy significantly improves tumor control and patient survival rates [30].

In this context, magnetic nanostructures based on iron (Fe-NS) have been gaining attention, since they can combine the diagnostic (as contrast agents for magnetic resonance imaging) and therapy (magnetic hyperthermia) properties. Although the Fe-oxide NS are the most reported in the literature, Fe-NS are a promising alternative since the high magnetic moment of Fe-NS can improve the heat dissipation phenomena produced by the magnetic hysteresis, due to the irreversible magnetization/demagnetization processes induced by an applied alternating magnetic field.

In parallel, now taking into account the electromagnetic radiation as the external stimuli, gold nanostructures (AuNS) have been the subject of much attention in the academic and clinical environment, due to their biocompatibility and high absorption of electromagnetic radiation in the near-infrared range caused by its surface plasmon resonance. Magnetic hyperthermia (MHT) and photothermal therapy (PTT), described in the next sections, are emergent state-of-the-art techniques for thermal cancer treatment and both rely on nanoparticles to achieve thermotherapy.

3.1 Heating power measurement methods

Before presenting the PTT and MHT techniques is important to introduce a figure-of-merit that is used to quantify and compare different NS heating efficiencies. It is known as the Specific Absorption Rate (SAR) or Specific Loss Power (SLP) and is defined as:

$$SAR = \frac{P}{m_{NS}} \tag{3.1}$$

where P is the heat power dissipated by the nanostructures and m_{NS} is the mass of the material. The initial temperature as a function of time slope method is the most popular approach to treat the measured data, where SAR values can be calculated resorting to the slope of the initial temperature rise (Figure 3.2). Its units are power dissipation per unit mass of element (Wg^{-1}) and is calculated using the following formula:

$$SAR = \frac{m_W C_W}{m_{NS}} \frac{dT}{dt} \tag{3.2}$$

where m_W and C_W corresponds, respectively, to the mass and specific heat capacity of the liquid media (water, C_W = 4.18 $Jg^{-1}K^{-1}$) and the component $\frac{dT}{dt}$ is the initial slope [31, 34]

.

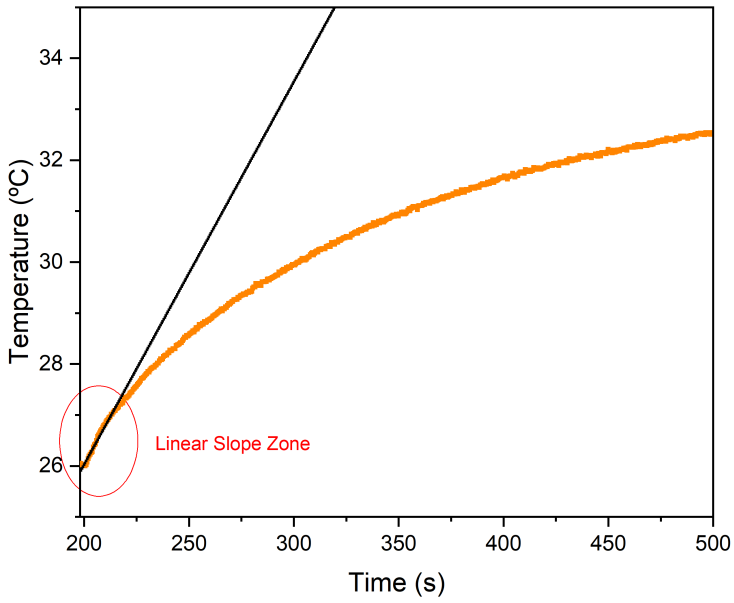

FIGURE 3.2: Demonstration of the linear slope zone on the initial temperature rise.

In the case of magnetic hyperthermia, where the external stimuli are alternating magnetic fields we can add the concept of Intrinsic Loss Power (ILP) that relates to the the SAR as:

$$ILP = \frac{SAR}{fH^2} \tag{3.3}$$

Analysing the previous equation it is possible to observe that the heat dissipated by MNPs diminishes quadratically with the strength (H) and linearly with the frequency (f) of the applied alternating magnetic field (AMF) [34].

3.2 Photothermal therapy

Photothermal therapy (PTT) is a minimally invasive local treatment modality whose goal is to convert electromagnetic radiation into heat by stimulation of photoabsorbing agents that are administrated to the body either intravenously or intratumorally [32].

Similarly to PTT, there are other treatment modalities that employ electromagnetic radiation as energy source, such as radiotherapy or Photodynamic therapy (PDT). However, they operate in different laser wavelengths ranges. Radiotherapy, for instance, operates

on very short wavelengths while Photodynamic therapy (PDT), involving the administration and excitation of photosensitizers, operates on longer wavelengths in the visible light range [35]. Laser light in the near-infrared (NIR) region (700-1100 nm) is the energy source used in PTT due to the higher tissue penetration capability and lower absorption in biological tissues [32]. This partial transparency of biological tissues in the NIR range is an advantage because it limits the heating of healthy surrounding tissues.

Another important aspect to this technique is the laser delivery mode, as it could be through a continuous-wave or pulsed-mode laser (nano or femtosecond lasers). While continuous lasers cause a higher temperature variation, the pulsed-mode ones offer a superior light-to-heat conversion with an instantaneous energy transfer at high intensities (in the femtosecond case). Short pulsed lasers, in their turn, cause less heat dissipation, therefore leading to less hazards in healthy tissues surrounding the tumor [32].

The ideal PTT photoabsorbing agents should gather certain characteristics such as low toxicity and good biocompatibility, appropriate size for tumor accumulation, ability to be eliminated through metabolic pathways in vivo, easy functionalization and excellent light-to-heat conversion efficiency. In the nanomaterials class, metallic nanoparticles, carbon-based nanomaterials and quantum dots are some examples of PTT absorbing agents that have been developed so far [32].

3.2.1 Gold Nanostructures

Gold nanostructures have been extensively explored as photothermal agents due to their biocompatibility and ability to generate heat due to the absorption of electromagnetic radiation. Yet, the photothermal conversion efficiency is highly dependent of the NS morphology. While spherical NPs have peak absorptions located in the visible light wavelength range, gold nanorods, nanoshells, and nanostars have a strong absorption in the NIR region [36].

The heat generation process, induced by the laser irradiation on the gold nanostructures, can be explained by a particular feature of metallic nanoparticles called surface plasmon ressoance (SPR). SPR is caused by the presence of conduction electrons that oscillate on the metallic nanoparticle surface. If the incident light wavelength is in resonance with the oscillating electrons, an high-energy state is reached, leading to a sequential relaxation in the form of heat. In this case, the light absorption results in optimal heat generation that ultimately dissipates from the particle to the surrounding media [32].

When compared to other geometries, gold nanorods (AuNRs) are known to have higher absorption and scattering coefficients. This is intensively described in study made by Espinosa *et al* that showed the influence of different shaped gold nanostructures with regard to peak absorption position and heat generation efficiency in different media. Among all the studied nanostuctures - gold nanostars (AuNST), gold nanorods (AuNR) and gold nanoshells (AuNS) - the gold nanorods showed the larger temperature raise, reaching an increase of approximately 20 degrees for a concentration of 0.15 $g_{Au}L^{-1}$ in an aqueous dispersion (Figure 3.3b). It is important to emphasize that the nanostructures were under the excitation conditions corresponding to the their wavelength of plasmonic resonance (808 nm for gold nanorods, nanoshells, and 85 nm nanostars, and 680 nm for the 25 nm nanostars) (Figure 3.3a) [31].

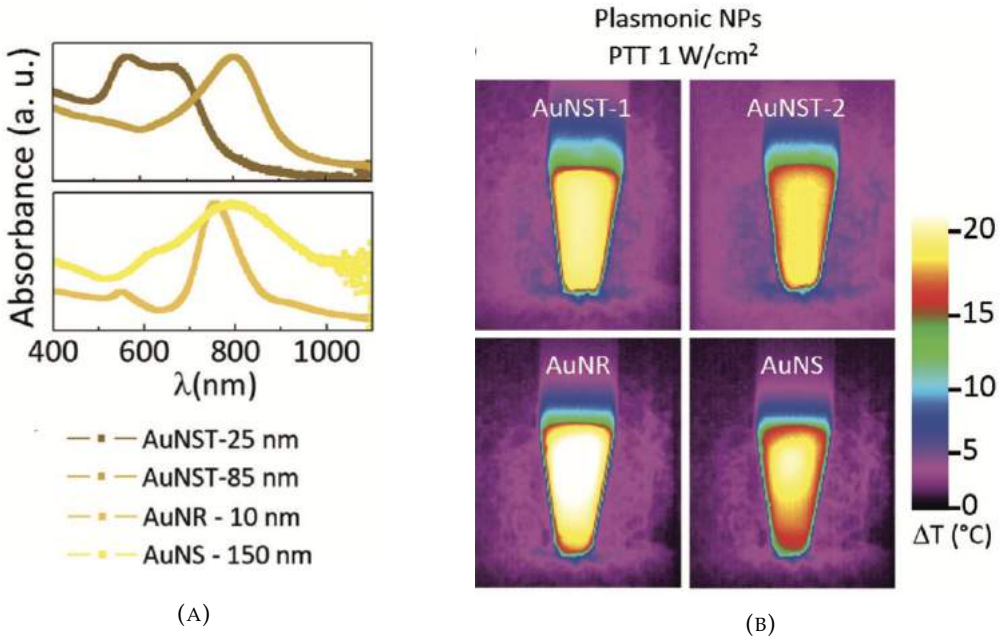

(A) (B)

FIGURE 3.3: (A) Absorbance peak for different shaped gold nanostructures; (B) Heating efficiancy of different shaped gold nanostructures [31].

In addition, by controlling the AuNR aspect ratio (AR), that corresponds to the ratio between the length and diameter of the nanorod, it is possible to tune the absorption spectra peak to match the desired laser wavelength (Figure 3.4b). For instance, to achieve optimal heat dissipation using the photothermal therapy technique with a continuous wave (CW) laser operating in 808 nm, the correspondent aspect ratio should be ≈ 4. This

AR is compatible, for example, with gold nanorods whose dimensions are, respectively, 60 and 15 nm for length and diameter [37].

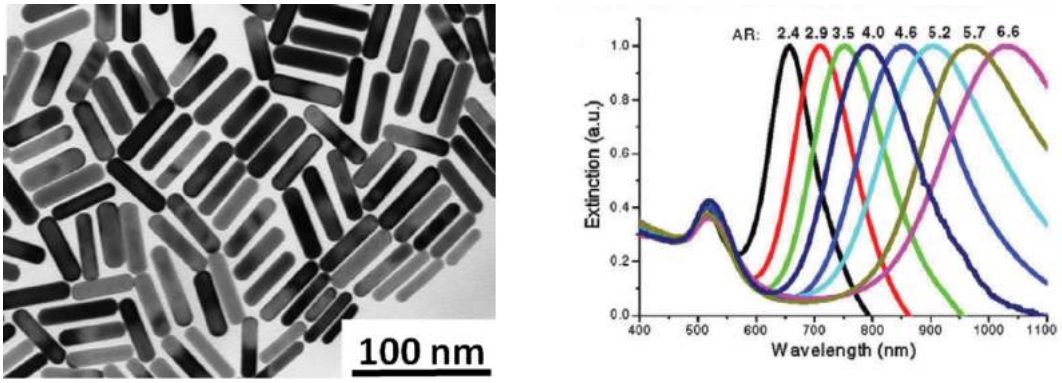

(A) (B)

FIGURE 3.4: (A) TEM image of gold nanorods with AR = 4 (length = 60 nm and diameter = 15nm) [38] ; (B) Influence of the Aspect Ratio on the absorbance peak for gold nanorods. [37]

Even though PTT mediated by AuNR has demonstrated promising results in vivo, in clinical practice hyperthermia is generally not used alone but concomitantly with other modalities like chemotherapy. This allows higher efficiencies at lower doses and subconsequently less side effects [32].

3.3 Magnetic hyperthermia

Magnetic hyperthermia (MHT) is a promising therapeutic method that relies on the use of functionalized magnetic nanoparticles (MNPs). In this approach, the MNPs are firstly injected into the tumor and then the patient is immersed in an alternating magnetic field (Figure 3.5).

As previously explained, when the MNPs are under the influence of an applied alternating magnetic field (AMF) the area of their magnetic hysteresis loop, A, corresponds to the dissipated energy. Hereupon we can elevate the tumor´s temperature by taking advantage of the behavior of MNPs and, due to their excitation, the temperature of the tumor rises. This temperature rise can improve the effectiveness of chemotherapy (T = 42–45 ^{o}C) and, if temperatures above 50°C are reached, they can directly kill the tumor cells by necrosis [39].

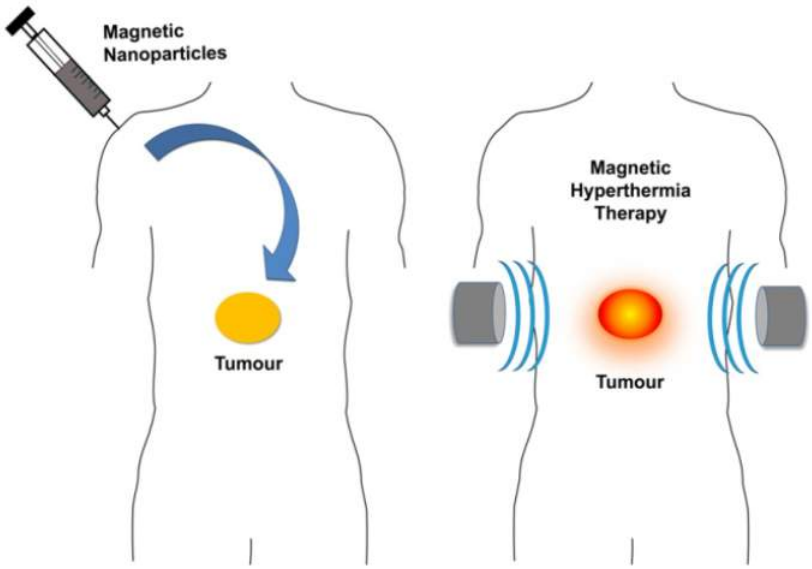

FIGURE 3.5: Illustrative representation of the magnetic hyperthermia technique [40].

The specific absorption rate (SAR), that evaluates the power generated by the MNPs, is directly proportional to the frequency of the AMF, f, as we can see by the equation below:

$$SAR = Af \tag{3.4}$$

This equation leads to the idea that one can maximize the SAR values by increasing this parameter and this way meet the needs of oncology, that requires biocompatible MNPs with large heating power. However, there is a medical limitation that prevents humans to be exposed to high frequency alternating magnetic fields and therefore there is a need to achieve optimal SAR values for specific values of the applied frequency and magnetic field. Typical values used in medical treatments so far are in the [10-1000 kHz] range [39].

The main advantage of MNPs-mediated MHT in the therapeutic field is related to the deep tissue penetration and selectively killing of cancer cells without harming the surrounding healthy tissues. In other words, the magnetic nanoparticles contribute to intracellular hyperthermia by directly delivering of the therapeutic heating to the cancer cells. This intracellular hyperthermia can be further improved by conjugating the MNPS with cell-targeting ligands. Although MNPs-MHT therapy is already in clinical trials, further research and development work are required to understand the full potential of this cancer therapy modality [29].

3.3.1 Iron nanostructures

Regarding magnetic nanoparticles developed for MHT, the Fe-oxide NS are the most reported in the literature due to their expected biocompatibility and chemical stability on the superparamagnetic domain. However, the main obstacle for clinical application is related to their low energy conversion efficiency which demands large nanoparticle doses, on the milligram level, therefore leading to toxicity concerns [41].

One way to experimentally optimize the SAR value is to increase the MNS saturation magnetization. Since iron is a material with weak anisotropy and high M_s, Fe-NS are a promising alternative that can improve the heat dissipation phenomena produced by the magnetic hysteresis, due to the irreversible magnetization/demagnetization processes induced by an applied AMF [39].

The particle size is another parameter that influences the generated heat. As mentioned in section 2.3.1, the magnetic behavior progressively changes from superparamagnetic to single-domain or multi-domain ferromagnetism, as the nanoparticle size increases (Figure 2.7). The heating performance follows a similar tendency and the relationship between nanoparticle size, number of domains and SAR is shown in Figure 3.6 where one can see that ferromagnetic single-domain nanoparticles are the best candidates and display the highest specific losses [27].

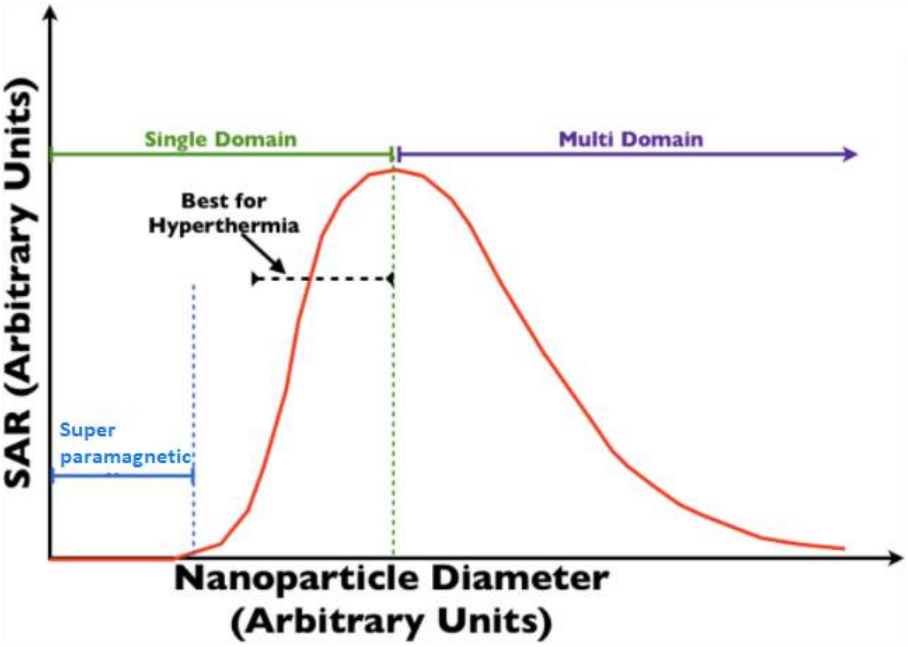

FIGURE 3.6: Dependence of SAR on nanoparticle diameter. Single-domain particles, whose size is close to the single/multi-domain transition are desirable due to high SAR and smaller size [27].

3.4 MHT combined with PTT

Even though PTT and MHT have been in clinical trials, there are some drawbacks that need to be considered, including the requirement of high NPs concentration and a significant reduction of heating capacity in a cellular environment when compared to an aqueous medium [31]. Instead of focusing on the limitations of these treatment methods individually, one can focus on taking advantage of each technique's strengths through a nanoscale combination of materials with magnetic and plasmonic properties. A multifunctional hybrid-design nanostructure seems to be a promising approach to meet the current therapeutic needs for an efficient cancer treatment. In this line of thought, the core-shell (CS) geometry allows to combine different properties simultaneously in the same nanomaterial.

The iron core-gold shell (Fe@Au CS), in particular, gathers the high magnetization of the iron with the gold tunable plasmonic properties in the NIR region. Beyond that, this complex geometry is suitable for structure stabilization as the shell layer prevents the core degradation and oxidation. Additionally, the biocompatibility of the gold shell layer provides a platform for easy functionalization [42, 43]. Hereupon, an adequate magneto-plasmonic nanostructure design can be employed to combine photothermia with magnetic hyperthermia into an efficient bimodal thermotherapy. In the past few years, it has been demonstrated that the dual-mode treatment of MNPs-MHT and PTT not only can provide the cumulative heat effect, but it can also achieve a synergic effect of 1+1>2 (Figure 3.7) [29].

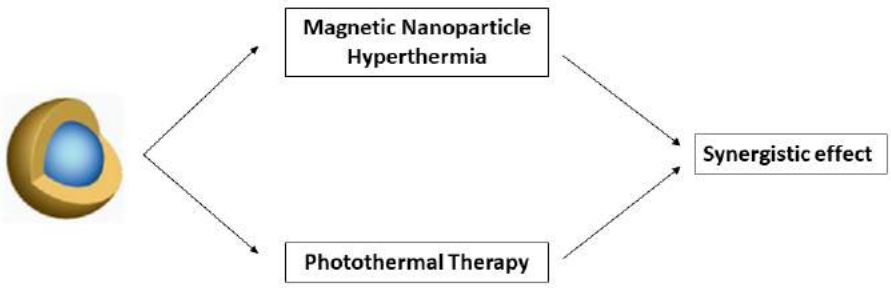

FIGURE 3.7: Synergistic effect of dual-mode treatment with nanoparticle mediated magnetic hyperthermia and phototherapy accomplished due to the complex core-shell geometry.

3.5 Motivation and Objectives

As described in the sections above, gold (plasmonic) and iron (magnetic) nanoparticles are prime candidates for the development of nanoparticle mediated thermotherapy. Hereupon the main objectives of this work are:

- To produce single Iron nanospheres and characterize them regarding their magnetic behavior and morphology
- To produce single Gold nanospheres and characterize them regarding their morphology and absorption behavior.
- To produce, and characterize as well, nanostructures with more complex morphology such as core-shell to combine the strongest points of each thermotherapy technique.
- To evaluate the heating efficiency and performance of AuNRs ($AR \sim 4$) stimulated with a continuous wave laser operating in the NIR range, regarding the influence of different parameters such as AuNR concentration, aqueous solution volume and laser spot area.

The nanospheres were produced by the Laser Ablation in Liquids (LAL) technique that will be described in the next chapter.

Chapter 4

Nanostructure Production and Characterization Techniques

This chapter is dedicated to the nanoparticles production technique known as Laser Ablation is Liquids (LAL). It will cover a general description of the procedure and the involved ablation mechanisms with the discussion of several involved parameters. Lastly, the employed nanoparticle characterization techniques are presented.

4.1 Laser Ablation in Liquids (LAL)

The pulsed laser ablation in liquids (PLAL) is continuously becoming an attractive technique for nanomaterial fabrication due to its versatility, low cost and ease of execution [44]. In simple terms, the LAL technique consists of a top-down approach in which a focused laser strikes a target of the desired particle material. This target is immersed in a liquid where the produced particles will be suspended and stored after the ablation (Figure 4.1). Some relevant advantages of this technique include the fact that it is considered an eco-friendly procedure, since it does not necessarily involve the use of chemical precursors that, in addition to being expensive, can also be toxic and result in the contamination of the colloidal solution [44, 45]. It is one of the fastest, low-priced and cleanest ways to produce colloidal nanostructures with a simple experimental set up that requires minimal manual operation [44, 46]. Furthermore, it is considered a highly versatile technique as it can be applied with a wide range of target/liquid combinations and, by laser ablating

multi-element target materials, nanostructures with complex stoichiometries can be synthesized. This last point was considered difficult or even unreachable to other techniques [45].

The shape, size distribution and structural properties of the NPs are dependent on several factors, such as the liquid in which ablation occurs and on laser parameters such as pulse width, wavelength, fluence or ablation time duration [45]. Lasers with femtosecond (fs), picosecond (ps) or nanosecond (ns) pulses at visible or near-infrared wavelengths have been exploited for NP synthesis via LAL.

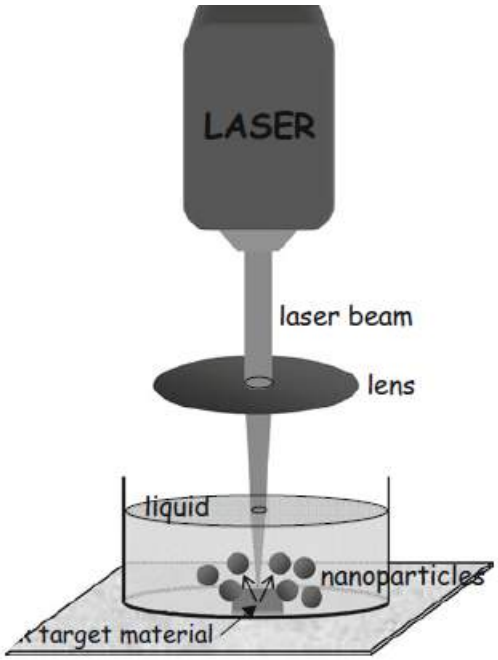

FIGURE 4.1: Schematic illustration of the simplest laser ablation in liquids set-up [45].

4.1.1 Mechanisms of Laser Ablation in Liquids

By definition, laser ablation consists in the thermal or non-thermal process of removing atoms from a solid's surface by irradiating it with an intense continuous wave (CW) or pulsed laser beam [47] . The difference between CW and pulsed laser is related to the output of the laser. Once the system is powered on, the CW laser beam presents a continuous output, while the pulsed laser presents a short time output, as illustrated in Figure 4.2. As one can see, the peak output power of a pulsed laser beam is much higher when compared to a CW laser beam, considering the same average output power [47].

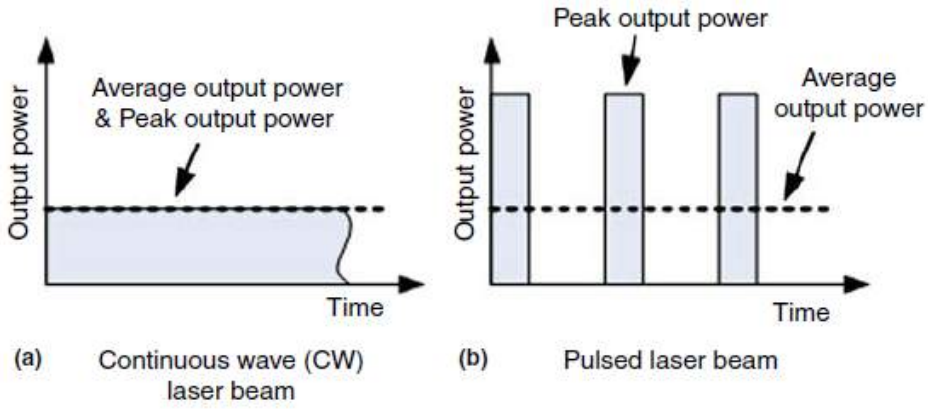

FIGURE 4.2: Illustration of the peak output power and the average output power of a CW laser beam and pulsed laser beam [47].

The laser type is precisely one of the parameters that has the most influence in the ablation mechanism. For instance, when a target's surface is irradiated by a CW laser beam or long-pulsed laser beam (nanoseconds pulsed case), the material is heated due to the absorbed laser energy (see next subsection for details). In contrast, for a short-pulsed laser (femtosecond laser case), the time duration of the laser interaction with the material is very short and the heat energy has no time to diffuse itself in the lattice. This means that the duration of the pulse is inferior when compared to the time taken by the excited molecules, atoms and electrons to release heat energy (i.e., electron–phonon relaxation time) and therefore the short-pulse laser ablation process is considered a non-thermal process [47].

4.1.1.1 Nanosecond pulsed laser ablation

As previously said, the ablation mechanism is highly dependent on the laser type. In the nanosecond pulse laser case the process involves the formation of plasma, cavitation bubbles and shockwaves [44]. The laser ablation process can be described in a series of sequential steps, presented in figure 4.3, starting when the laser pulse goes through the liquid media before reaching the target. Here the pulse should penetrate the layer of liquid, delivering the laser energy exclusively to the target [44]. Once the laser pulse hits the materials' surface, a non-equilibrium plasma plume containing the ablated material is formed and its high temperature results in the ionization and vaporization of the liquid.

The plume will then expand into the surrounding liquid, along with the emission of a shockwave. The latter is a consequence of the rapid expansion of the plume that leads to the generation of two shock waves traveling in opposite directions, one to the solid target and other through the liquid [44, 45].

During the expansion, the plasma plume temperature decreases, releasing energy to the solution. This phenomena, in its turn, leads to the generation of a cavitation bubble around the ablated material. As the bubble expands to its maximum size, its temperature and pressure decreases until the gas inside the bubble is in equilibrium with the surrounding liquid. Then, the bubble starts shrinking until collapse, creating a second shock wave [44, 45].

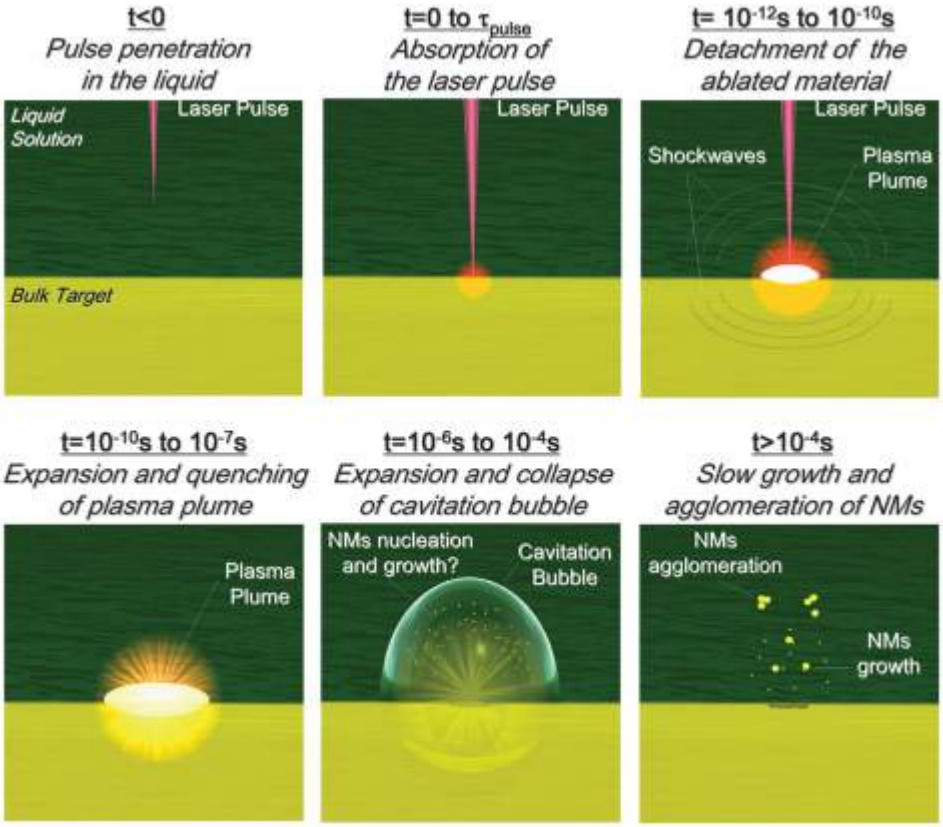

FIGURE 4.3: Sketch of the timeline of the LAL technique considering ns pulses. Nucleation and growth of the NPs are hypothesized in the 10^{-6}–10^{-4} s time range, although precise information is lacking [44].

It is important to refer that, during nanosecond laser ablation, the plasma overlaps in time with the pulse. This means that plasma will be produced during the laser pulse, in a way that the pulse can reheat the plasma. This leads to higher persistence of the plasma

for nanosecond laser ablation when compared to femtosecond laser ablation (explained in the next section).

Even though the ablation mechanism still deserves fundamental studies in order to be fully understood, the literature points out that the predominant NP formation mechanism by LAL consists in nucleation during the plasma plume cooling, followed by nuclei growth and coalescence [46]. However other mechanisms, such as boiling or explosive processes, are also observed simultaneously to the plasma formation. In fact, the coexistence of these different processes in the ablation mechanism is one of the reasons for the characteristic NP large size distributions of LAL [46].

4.1.1.2 Femtosecond pulsed laser ablation

As previously mentioned, the femtosecond pulse duration is much shorter when compared to the typical coupling times between electron and lattice. This means that the heat diffusion, material ejection and plasma plume formation will occur significantly after the interaction of the pulse with the target [48]. In fact, due to this short pulse duration, femtosecond pulses do not usually interact with the ejected material, as the laser induced plasma only occurs several picoseconds after the laser energy deposition [48].

During laser–matter interaction, regardless the duration of the pulse, the laser energy will interact with the electrons in the system. While for long pulse ns lasers the absorption process is linear and obeys the Beer-Lambert law, for ultrafast laser absorption nonlinear processes become significant due to their high peak intensities [49]. Due to negligible or non-existing thermal processes during the laser–matter interaction, the most significant contribution to femtosecond ablation comes from the generation of free electrons. It is important to refer that the absorption and ablation processes will be different depending on whether we are talking about metals or dielectrics. For instance, in metals free electrons in the conduction band absorb energy through inverse Bremsstrahlung absorption [49].

In terms of material removal and ablation, for fs laser pulses, there are two involved mechanisms that operate depending on the laser intensity. The first, known as Coulomb explosion, operates at low laser intensities near the ablation threshold. Here the excited electrons are ejected from the surface of the target, creating an electric field between the ejected electrons and the highly ionized atoms at the target surface [49]. The second, thermal vaporization, occurs for sufficiently high laser intensities above the ablation threshold. Here, the phase explosion is followed by thermal vaporization of the material and

the latter becomes the dominant mechanism for material removal [49].

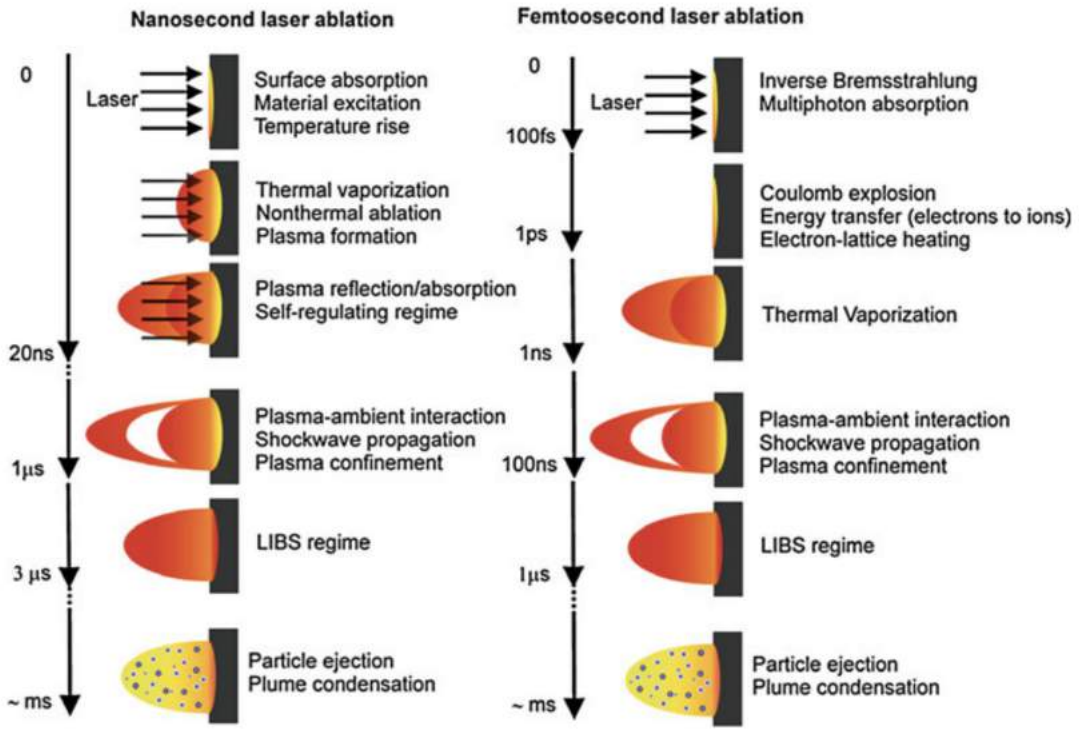

FIGURE 4.4: Approximate time scales of nanosecond and femtosecond energy absorption and laser ablation along with various processes happening during and after the laser pulse is given [49].

The femtosecond laser ablation presents some advantages when compared to the nanosecond case. Beyond the fact that peak intensity can reach much higher values, that create extreme conditions regarding the temperature and pressure that are favorable for the formation and even stabilization of metastable phases, the reduced thermal damage and heat affected zone in the target due to negligible heat conduction during the laser pulse duration prevents damaging or melting the target material (Figure 4.5) [47]. In other words, the fact that the laser interaction with target is considered a nonthermal process has influence in the hole morphology reducing or even eliminating some defects regarding the roughness of the ablation edge and large crack formation, improving the work precision of femtosecond laser ablation.

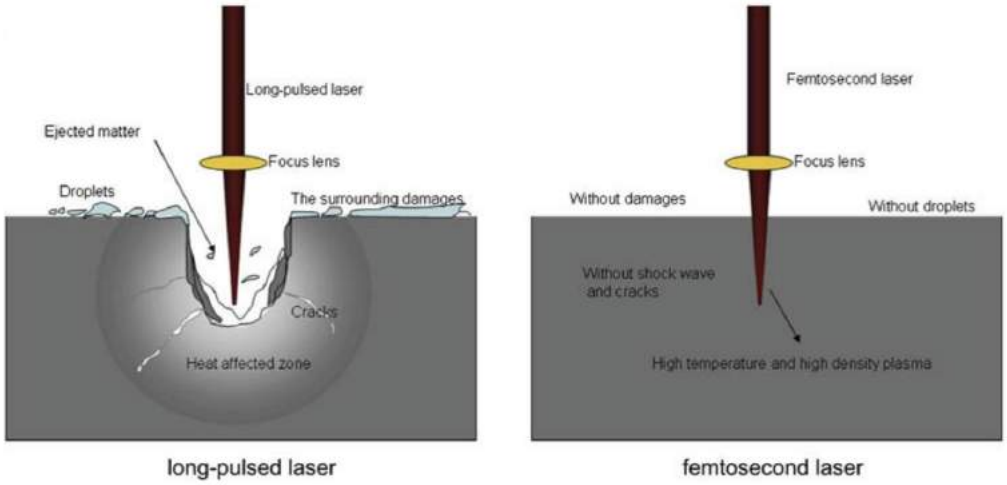

FIGURE 4.5: Differences in the hole morphology regarding the laser ablation pulse. [47]

4.1.2 Target/solution combinations

In LAL, the structure and composition of the produced nanostructures are heavily dependent on the solvent in which the ablation is performed.

In 2016, Amendola *et al* performed a systematic investigation that demonstrated that ethanol was a favourable solvent for the synthesis of single element gold and bimetallic sphere NPs by LAL [50]. Here, instead of bulk targets, the ablations were performed in thin Fe, Au/Fe and Au films composed by multilayers with different thickness and order of deposition. As one can see in Figure 4.6 the nanoparticles obtained in the ablation of the Fe thin film were involved in a low-contrast matrix that may be due to the presence of amorphous iron oxide. This hypothesis is supported by the continuous decrease in the thickness of this low contrast matrix as the amount of iron in the multilayers is reduced. However, the presence of iron in the obtained nanoparticles and on the nanoalloys is significantly higher when compared to an ablation performed in water under the same conditions [50].

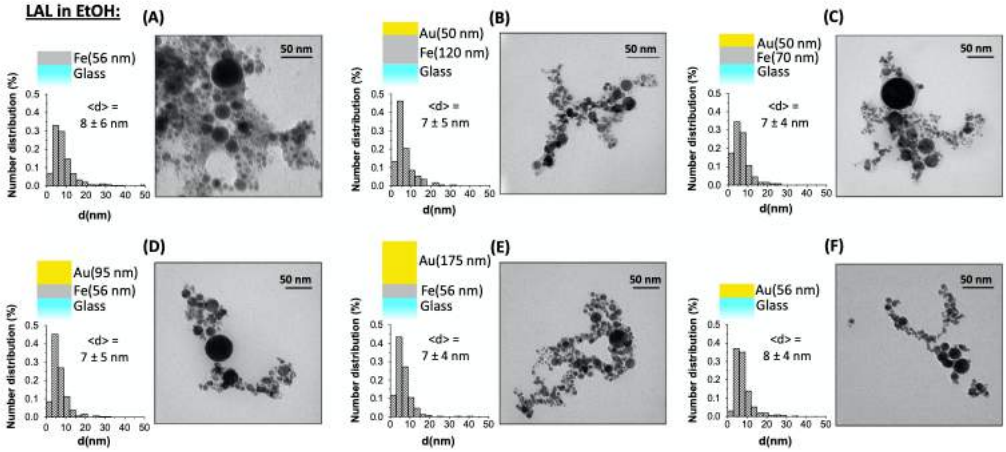

FIGURE 4.6: LAL of Au/Fe/Glass with different thickness in ethanol [50].

Later, a study lead by Tymoczko *et al*, selected acetone as the most favorable liquid for the synthesis of Fe@Au CS nanoparticles. In addition, they also report that the obtained colloids in this media exhibited excellent stability for several days, with a slow tendency to sedimentation happening only several weeks later. The ablated targets, in this case, also consisted in thin bimetallic films composed of gold and iron layers deposited in different orders above a glass substrate, or in an alloy of the two metals (Figure 4.7). The core-shell morphology was more abundant in the alloy film, followed by the Fe/Au bilayer configuration [43].

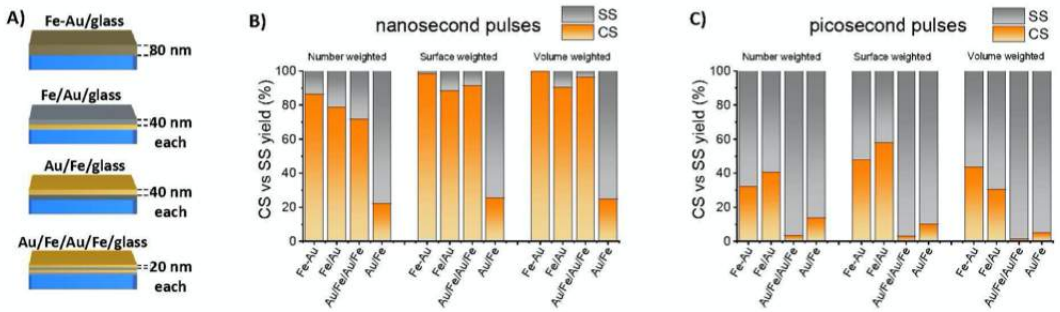

FIGURE 4.7: (A) Different types of Fe-Au films ablated in acetone; (B) Core-Shell (Core-shell) vs SS (Solid Solution) yield measured for the different film types in ns LAL; (C) Same as B but for the ps LAL case [43].

The ablations in these reports were carried out with a nano and a picosecond laser, so our objective was to perform a similar study for the femtosecond laser ablation case.

4.2 Characterization Techniques

Several techniques were used to characterize the produced nanoparticles. Scanning Electron Microscopy (SEM) and Energy Dispersion Spectroscopy (EDS) were used to study the morphology and chemical composition of the particles, Superconducting Quantum Interference Device (SQUID) to investigate their magnetic properties, UV-Vis Spectroscopy to measure the absorption spectra, and DLS to obtain information regarding particle size distribution. All of them will be briefly introduced along this section.

4.2.1 Scanning Electron Microscopy

The scanning electron microscopy (SEM) technique is considered one of the most versatile available instruments for the examination and analysis of the morphology and chemical composition of a sample. Merely, the set-up consists in an electron gun that produces a high energy electron beam that is focused by an optical system into a small target spot on the sample surface. Using a set of deflection coils, one can move the spot location on the sample surface, allowing to map the surface and construct an image of it. The obtained image is a result of the elastic and inelastic interactions between the scattered electrons and the sample surface (Figure 4.8) [51].

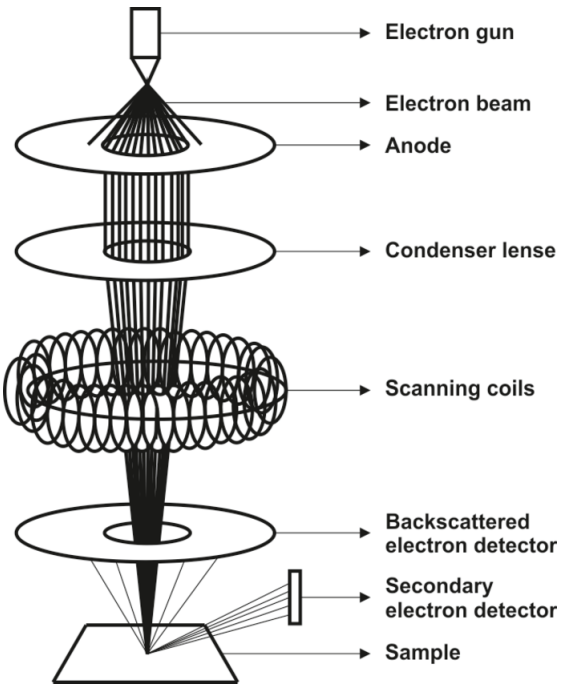

FIGURE 4.8: Schematic representation of a SEM set-up [52].

Elastic scattering comes from the deflection of the incident electron beam by the specimen atomic nucleus. This interaction is characterized by a negligible energy loss during the collision and by a wide-angle directional change of the scattered electrons. Incident electrons that bounce back from the sample through an angle larger than 90 degrees are called backscattered electrons (BSE) and yield a useful signal for imaging the sample. The BSE, in particular, allow the identification of different macroscopic phases that may be present in the sample since they are particularly sensitive to the atomic number [51] .

In the inelastic scattering case, the interactions between the incident electrons and the atoms/electrons of the sample results in a substantial energy transfer to that atom. The amount of energy loss relies on the specimen electrons excitation conditions and on the binding energy of the electron to the atom. As a result, secondary electrons (SE), which are electrons generated as ionization products, are formed, ejected from the sample and detected, providing detailed surface morphology information. In addition to these, a number of other imaging forming signals are produced when an electron beam strikes a sample, including the emission of characteristic x-rays or Auger electrons [51].

To characterize a sample, it is also important to know its components. The energy-dispersive X-ray spectroscopy (EDS), along with the secondary and backscattered electrons, is one of the SEM most commonly used modes. The EDS, usually incorporated in the SEM set-up, allows to estimate the chemical composition and proportion of the elements in the sample. As in SEM, this technique is based in the interaction between the electron beam and the sample, particularly in the resulting radiation emitted as X-rays. This occurs when an outer shell electron occupies a vacancy in an inner shell, left empty by one electron that was extracted due to the energy transferred by the incident beam (Figure 4.9). As different elements have different energy between core shells, this method allows to identify the chemical composition and proportion of atomic species in the sample, by detecting the energy and intensity, respectively, of the emitted X-Rays and comparing to already known radiation spectra. In order to characterize our samples, a FEI Quanta 400FEG high resolution (HR) SEM has been used.

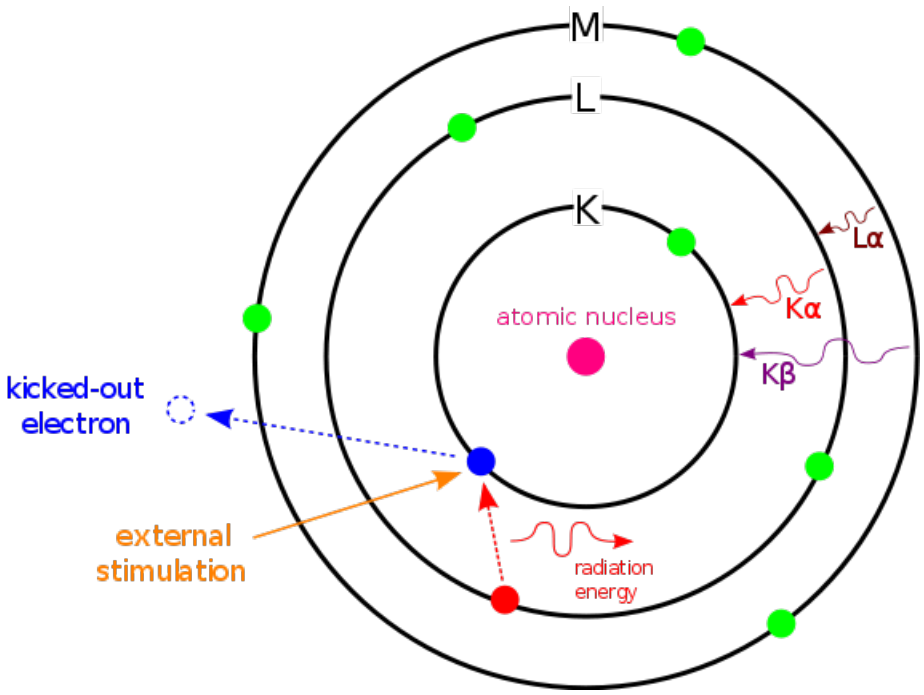

FIGURE 4.9: Illustration of the EDS spectroscopy principle [53].

4.2.2 Superconducting quantum interference device

The superconducting quantum interference device (SQUID) is a very sensitive magnetometer based on superconducting loops. The term magnetometry, in general, refers to measurement of the magnetization or the magnetic moment of a sample [54]. The superconducting state, in its turn, is a phenomena that occurs to certain materials when they are cooled below a critical temperature, close to absolute zero. Here, the material undergo a transition from normal to resistanceless behavior, meaning that, at this temperature, electrons can move freely through the material.

The operation principle of a SQUID is based on the Josephson effect. The latter is a physical effect that is manifested by the appearance of an electrical current that flows through two interconnected superconductors, separated by a very thin insulating barrier. This arrangement, known as a Josephson Junction, allows the quantum tunnelling effect to occur. This effect is influenced by magnetic fields in its vicinity, enabling the Josephson junction to be used in devices that measure extremely weak magnetic fields.

The commercially available SQUID magnetometers typically allow a fully automated measurement of the magnetization of a specimen, as a function of magnetic field and/or temperature. The M(T) measurements, for instance, are typically obtained through ZFC (Zero Field Cooled)-FC(Field-Cooled) curves that allow the estimation of the Blocking

temperature (T_B) [5]. Briefly, in the ZFC-FC protocol, the sample is cooled from the room temperature (300K) in the presence of a magnetic field (FC) and with zero magnetic field (ZFC). Once the sample is cooled to the desired temperature (5K), a small magnetic field is applied (100 Oe) and the magnetization is measured while warming [5]. As the temperature increases, the thermal energy disturbs the system and more moments acquire energy to align with the external magnetic field. The number aligned moments reaches its maximum at T_B. Above this T_B, the thermal energy itself is strong enough to randomize the magnetic moments leading to a decrease in the magnetization [5]. Figure 4.10 shows a typical curve from a ZFC-FC measurement. Here, one can see that the T_B can be determined through the temperature derivative of the difference between the FC and ZFC magnetization curves (d(M_{FC}-M_{ZFC})/dT) , with the maxima corresponding to the blocking temperature of the main size distribution. This T_B determination method is considered more precise when compared to the one that considers T_B as the maximum of the ZFC curve [55] .

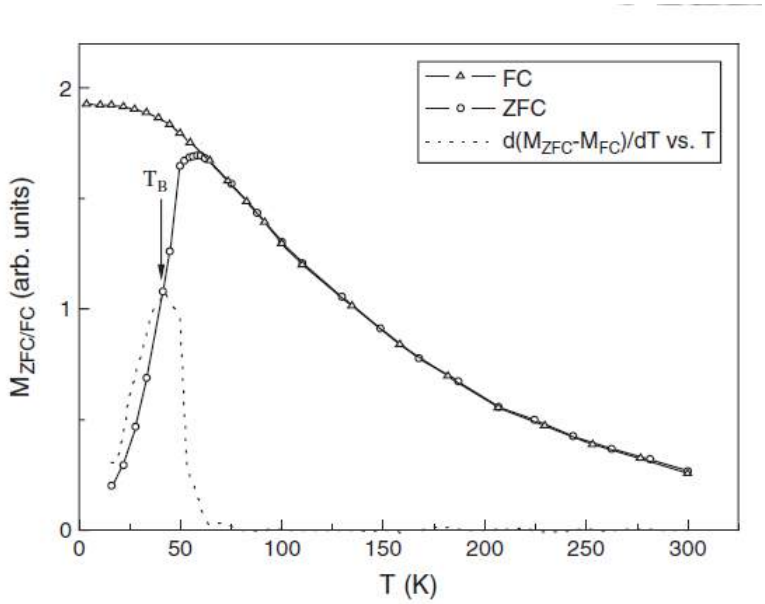

FIGURE 4.10: Typical curve obtained from a ZFC-FC measurement [55].

M(H) measurements, in its turn, allow the determination of certain parameters such as the coercivity, remanence and saturation magnetization, that help to determine the type of magnetic materials through their hysteresis loop. A typical obtained hysteresis loop is represented in Figure 4.11a. This behavior is due to the diamagnetic contribution of the sample holder and liquid in which the nanoparticles are suspended. Because of this, the linear parts of the graph have been fitted and this magnetic contribution has

been subtracted from the real magnetic behavior of the nanoparticles. The resulting loop is represented in Figure 4.11b. This process was repeated for each hysteresis loop. The SQUID used in this work is from MPMS SQUID by Quantum Design at IFIMUP-IN.

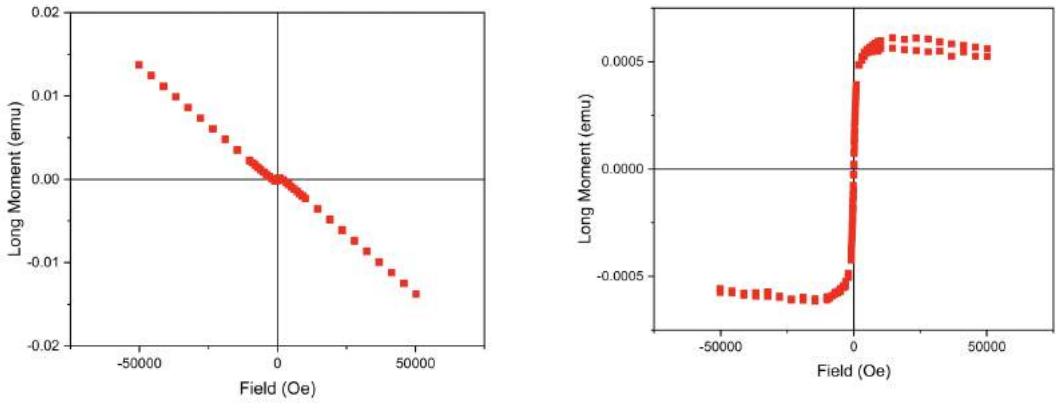

(A) (B)

FIGURE 4.11: Typical obtained hysteresis loop before (A) and after (B) the subtraction of the diamagnetic component in the magnetization.

4.2.3 UV-Vis Spectroscopy

UV-Vis spectroscopy is an analytical technique employed to obtain the absorbance spectra of sample. Hereupon, the technique indicates the wavelengths of ultraviolet (UV) or visible light that are absorbed by a sample.

The theory behind UV-vis spectroscopy is related to the wave nature of electromagnetic radiation and its interaction with matter. In other words, when an incident light beam hits matter, it can be absorbed, reflected or transmitted. Absorption occurs only when the frequency of the incoming light is equal to the energy difference between a molecule's ground (low-energy) and excited state [56, 57] . This means that the energy required for molecules to go through these transitions is electro-chemically specific depending on the energy levels of the molecule. The relationship between the energy difference and wavelength is described by the Planck equation, given by:

$$E = h\nu = hc/\lambda \tag{4.1}$$

where E is the energy required to elevate an electron from the fundamental to an excited state, h is Planck's constant, v is the wavenumber, c is the speed of light, and λ is the

wavelength [56]. By observing the equation one can see that the less energy needed to excite the electrons, the longer the wavelength of the absorption band.

The numerical value in a UV–VIS spectroscopy, typically called absorbance, A, is obtained by application of Beer-Lambert's law given by:

$$A = -log(T) = log(I_0/I) \tag{4.2}$$

where T is the transmittance and I_0 and I are, respectivelly, the intensity of the measuring beam before/after passing through the sample [57] .

4.2.4 Dynamic Light Scattering and Zeta Potential

In simple terms, the Dynamic Light Scattering (DLS) measures the Brownian motion of particles in a solution and relates it to their size. This is accomplished through the illumination of the particles with a laser, followed by a subsequent analysis of the intensity fluctuations of the scattered light over time (Figure 4.12).

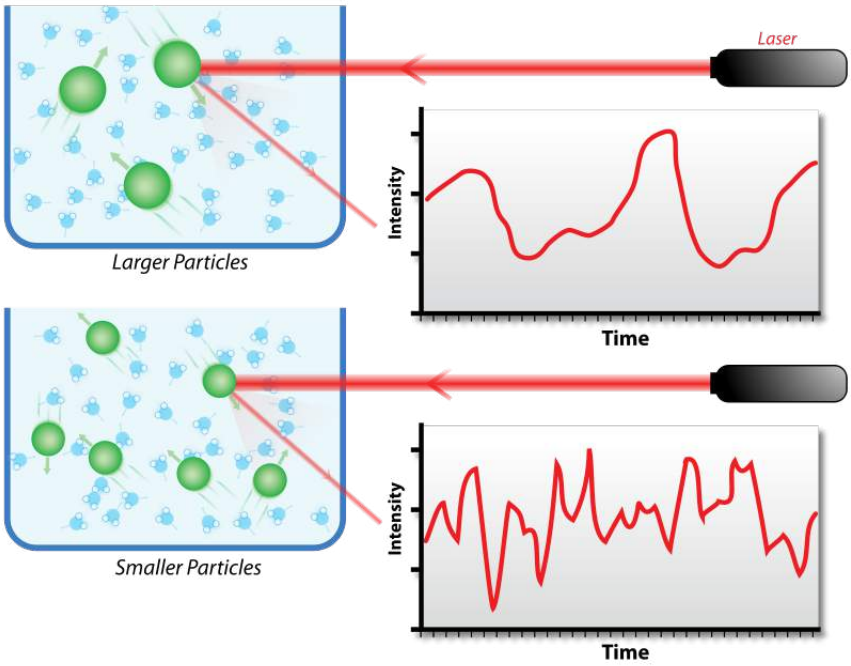

FIGURE 4.12: Illustration of dynamic light scattering technique on two samples: Larger particles on the top and smaller particles on the bottom [58].

When particles are dispersed in a liquid solution they move randomly in all directions. However, smaller particles move or diffuse the light more quickly when compared to larger particles which diffuse more slowly. The detected diffracted light from all the

particles forms a speckle pattern, shown in Figure 4.13, at a specific time. This pattern has light regions associated to constructutive interference and dark regions associted with destructive interference. As the particles are constantly in motion the speckle pattern will also appear to move and the intensity at any particular point appears to fluctuate. Then, the Zetasizer Nano system measures the rate of the intensity fluctuations and uses this to calculate the size of the particles through an autocorrelator that compares the intensity of light at each spot over time [58].

FIGURE 4.13: Example of a speckle pattern [58].

Even though the fundamental size distribution generated by DLS is an intensity distribution, it can be converted into a volume or number one. The difference between these distributions can be simply explained considering a sample that contains only two sizes of particles, with 5nm and 50nm for example, with equal numbers of each size particle.

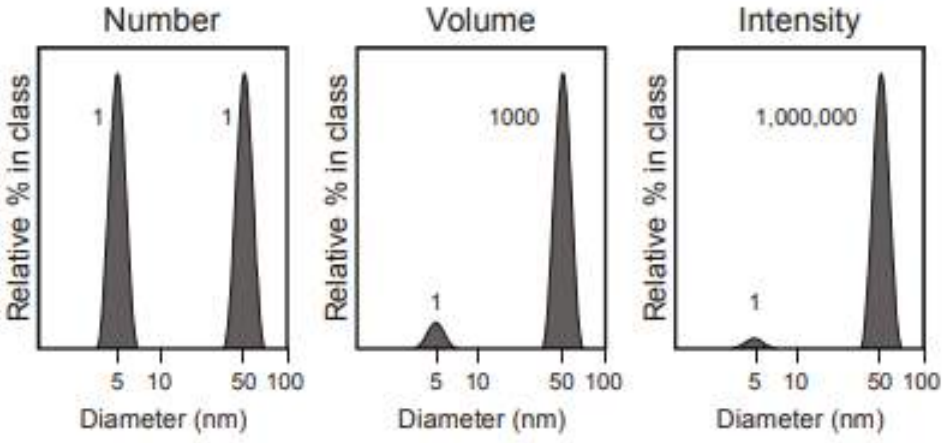

FIGURE 4.14: Different distributions generated by DLS [58].

The first graph in Figure 4.14 represents the obtained number distribution in this particular case. Here, two peaks of the same size are expected as there are equal number of particles. The second graph represents the result of a volume distribution. Since the volume of a sphere grows with r^3, the area of the peak for the 50nm particles will be

1000 times larger when compared to the peak of the 5nm. Lastly, the third graph shows the result as an intensity distribution and the area of the peak of the 50nm particles is 1,000,000 times larger than the peak for the 5nm.

Beyond DLS, the light scattering measurements also encompass the measurement of the zeta potential (ζ potential). Briefly, the zeta potential is a measure of the magnitude of repulsion or electrostatic attraction between particles, and is one of the fundamental parameters that affects a solution stability. If the particles in suspension have a large negative or positive zeta potential, they will tend to repel each other and there is no tendency to flocculate. In contrast, if the particles have low zeta potential values then there is no force preventing the particles to agglomerate. In general, particles with zeta potentials more positive than +30mV or more negative than -30mV are considered stable [58].

Chapter 5

Laser Ablation in Liquids - Experimental Results and Discussion

This chapter includes the experimental results obtained in the nanoparticle synthesis via Laser Ablation in Liquids. Along this work the ablations were performed under different conditions in order to investigate how certain parameters, such as the target kind or the used liquid media influenced the final nanoparticles morphology.

The primary goal of this work was to obtain single iron and single gold nanoparticles. This was accomplished through the ablation of bulk targets of the respective desired material. Then, in an attempt to obtain nanoparticles with more complex morphologies composed simultaneously by the two materials, we try to ablate thin-film targets that contained different layers electrodeposited above a glass substrate. In this step different gold and iron combinations were performed regarding the order of the materials deposition above the substrate. The first attempts involved a two layer combination where each had the order of material deposition changed. In other words, the tried combinations from the bottom layers to the top were: glass-iron-gold and glass-gold-iron. A three layer combination composed of glass-gold-iron-gold was also ablated.

Finally, we also investigate how the liquid media influenced the final result. Here, we compare the results obtained in the three layer combination when ablated in an ultra-pure ethanol and acetone solution. For each performed ablation, the obtained nanoparticles will be shown over SEM images.

5.1 Experimental Set-up/Details

Laser ablation for nanoparticles synthesis was carried out with a femtosecond (30 fs) pulsed laser operating at a beam wavelength of 800 nm, with a pulse repetition rate of 1KHz and a maximum pulse energy of 1 mJ. In our set-up the ablations were performed with the target lying at the bottom of a glass cuvette/beaker filled with the liquid solution. The cuvette/beaker was placed on a rotating support, in a way that during the ablation the sample was under a circular motion that prevented two consecutive laser strikes from occurring at the same point of the target. After the ablation, the solution containing the nanoparticles is stored in an eppendorf.

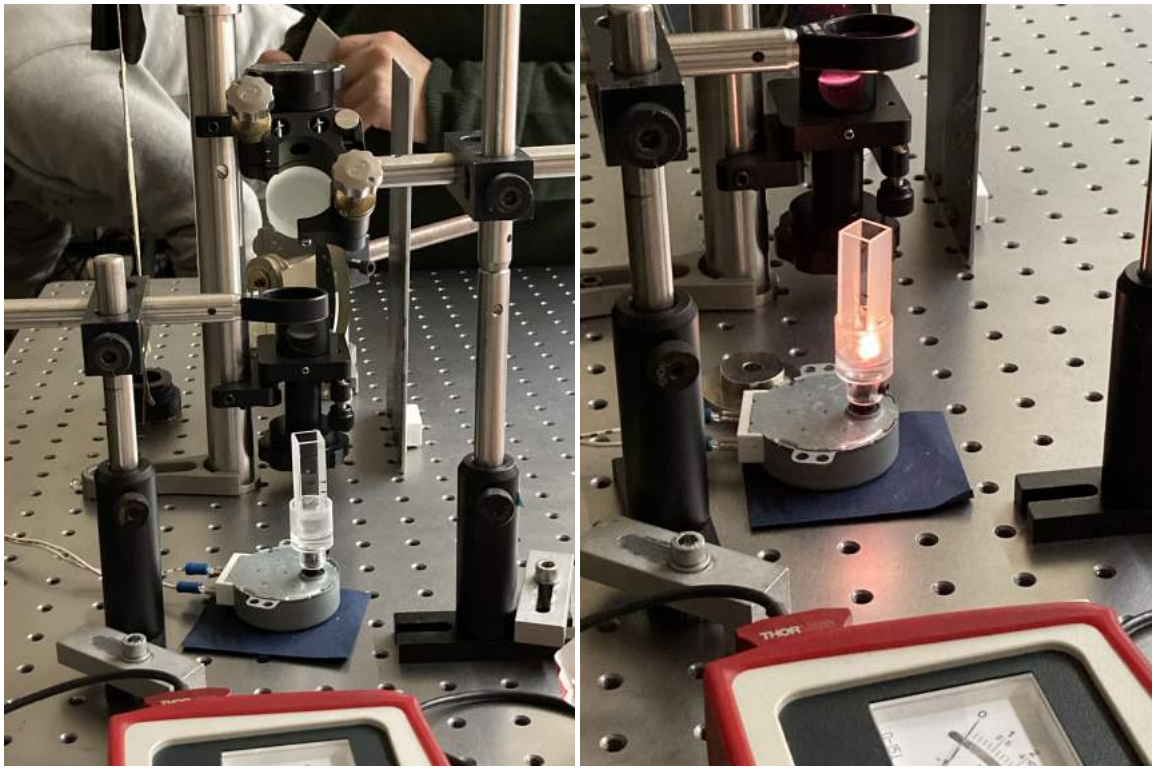

FIGURE 5.1: Laser ablation set-up.

5.1.1 Bulk target ablations

Here the used target was either a bulk piece of iron or gold. Immediately before ablation, the target surface was mechanically polished using SiC paper in order to smooth the surface and remove a possible oxide surface layer (Figure 5.2). The selected media was ethanol (99%) and the ablations were carried out during 60 minutes with a pulse energy

of $\sim$ 0.160 mJ. Note that this is the energy associated with each individual pulse. The height of the liquid above the target surface was in the 3-5 mm range.

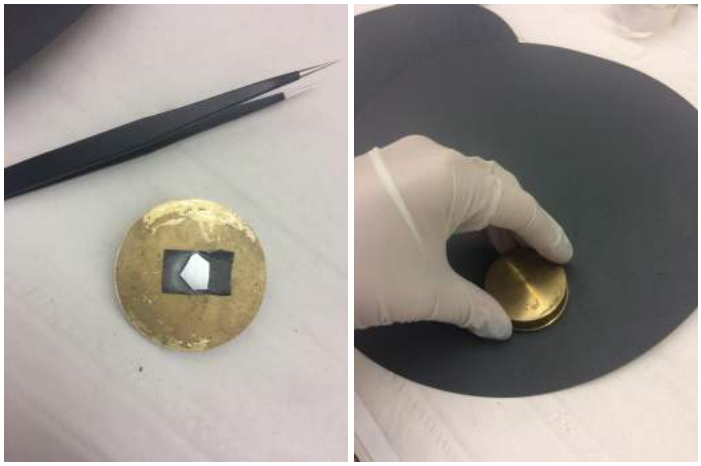

FIGURE 5.2: Polishment of the target with SiC paper before ablation.

The magnetic properties of the iron target were observed using SQUID magnetometry through a magnetization versus field, M(H), analysis performed at 300K. As one can see in Figure 5.3, SQUID measurements showed that the target had a saturation magnetization of 237.15 emu/g. This value is in agreement with the literature and the hysteresis curve presents ferromagnetic behavior, characteristic of iron [59]. The target also presented a coercivity of about 10 Oe. It is important to refer that the magnetization was normalized to the target mass (m_{target} = 0.08282g).

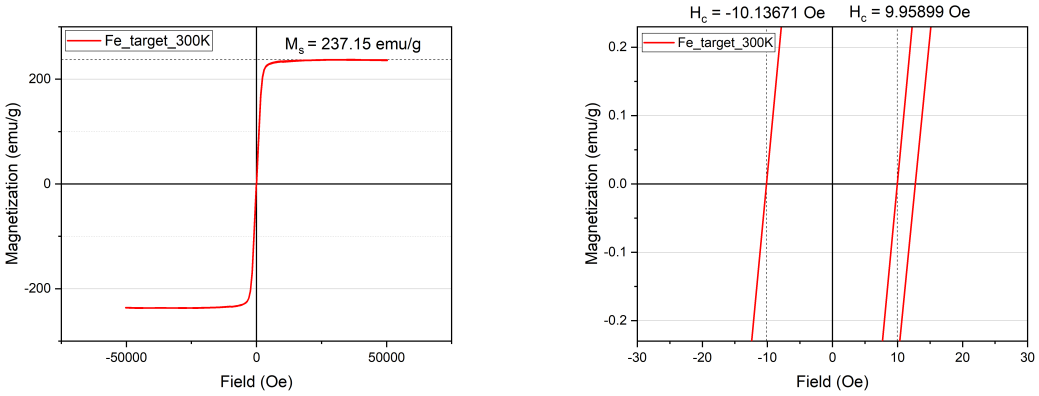

FIGURE 5.3: SQUID characterization of the bulk iron target at 300K.

5.1.1.1 Single Iron Nanoparticles

The ablation was carried with 5mm of ethanol (99%) during 60 minutes with a pulse energy of 0.160 mJ. In Figure 5.4 one can see the appearance of the solution stored in the eppendorf, after the ablation. Even though the solution did not obtain a significant color, when a magnetic field post-LAL was applied with an iman, it was possible to observe the particles traveling and following its direction.

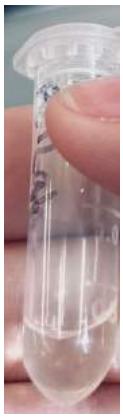

FIGURE 5.4: Post-LAL single-iron solution stored in an eppendorf.

Scanning electron microscopy (SEM) was used to obtain information regarding the nanoparticle morphology. The obtained nanoparticles along with their size distribution are presented, respectively, in Figures 5.5 and 5.6 where one can see that we successfully produced iron nanospheres. Their average size, estimated resorting to a Gaussian Fit applied to the distribution, was 368.5 nm with a standard deviation of 211.1 nm.

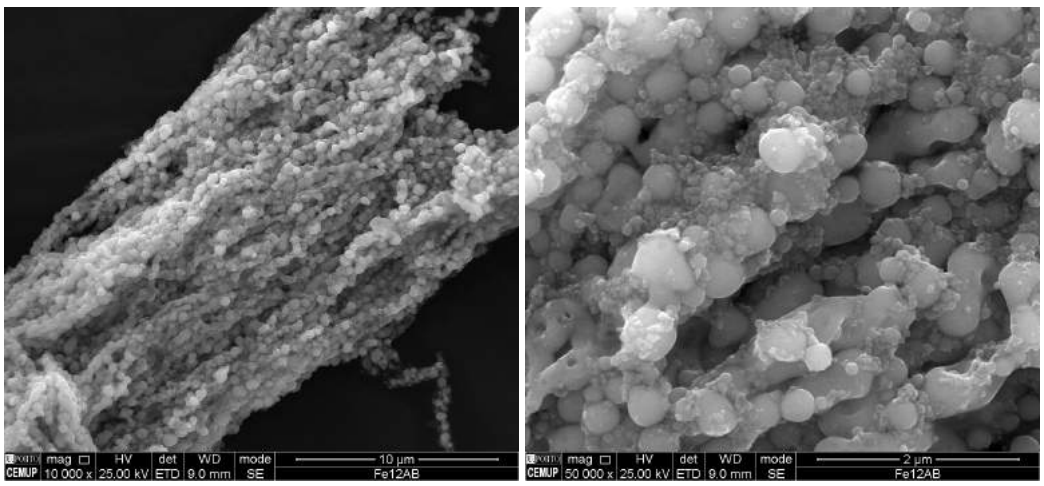

FIGURE 5.5: Fe-NPs synthetized through the ablation of an Iron target with a femtosecond laser in ethanol.

The histogram was obtained resorting to ImageJ, in which a manual and individual measure of the nanoparticles size was performed. This process was repeated for each histogram presented along this work.

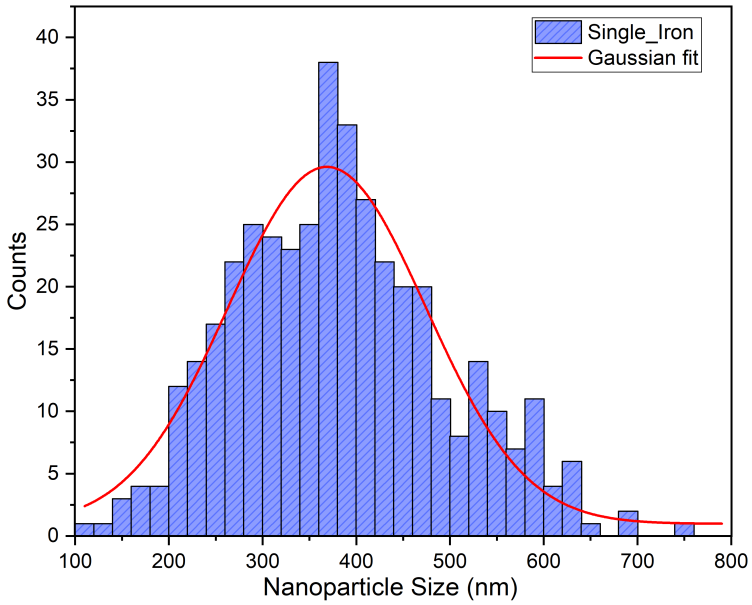

FIGURE 5.6: Size distribution of the single-iron nanoparticles produced by fs LAL with an applied Gaussian Fit. The particles presented an average size of 368.5 $\pm$ 211.1 nm.

The appearance of the iron target after the ablation, along with SEM images with different magnifications (100x, 1000x, 2500x,15000 and 40000x), can be seen in Figure 5.7.

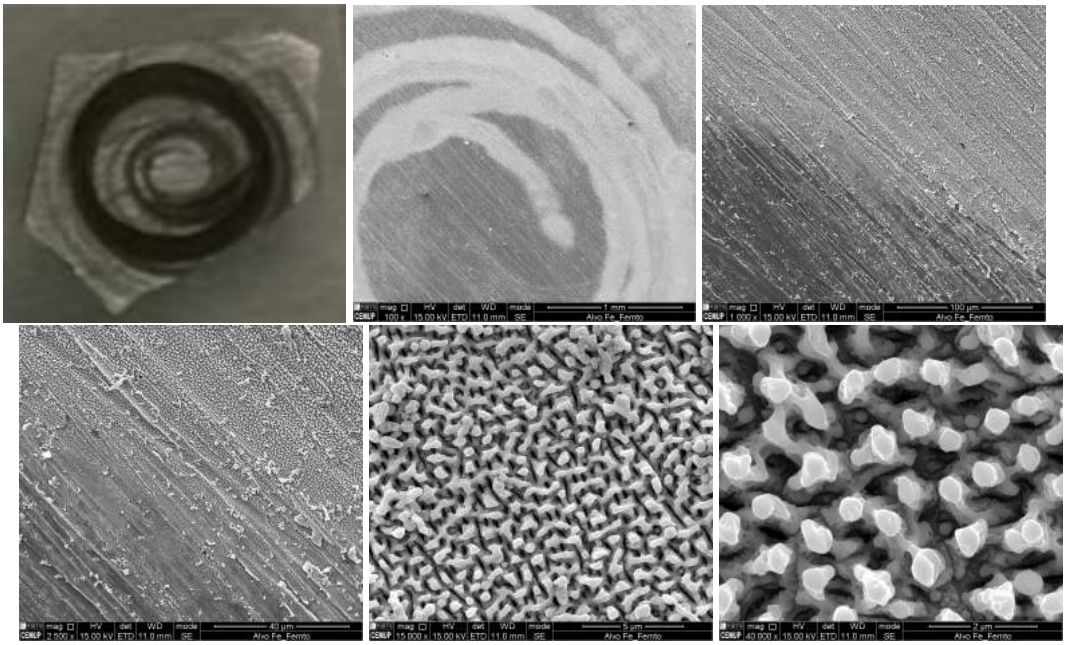

FIGURE 5.7: Appearance of the iron bulk target after the fs LAL. SEM images of the same with different magnifications (100x, 1000x, 2500x,15000 and 40000x).

5.1.1.2 Single Gold Nanoparticles

The ablation was carried with 3mm of ethanol (99%) during 60 minutes with a pulse energy of 0.167 mJ. In Figure 5.8a the appearance of the solution stored in the eppendorf after the ablation is presented. It is clear that the colloid presented a very evident purple tone, however only 2 days after the ablation, all the content was sedimented at the bottom of the eppendorf (Figure 5.45b).

(A) (B)

FIGURE 5.8: (A) Resulting solution obtained immediately after the fs LAL of a gold bulk target in ethanol; (B) Same solution 2 days later presenting sedimentation.

The obtained nanoparticles, along with the histogram of the same are presented, respectively in Figures 5.9 and 5.10. Gold nanospheres with an average size of 24.007 nm were successfully obtained. Here, the histogram was fitted with a LogNormal function.

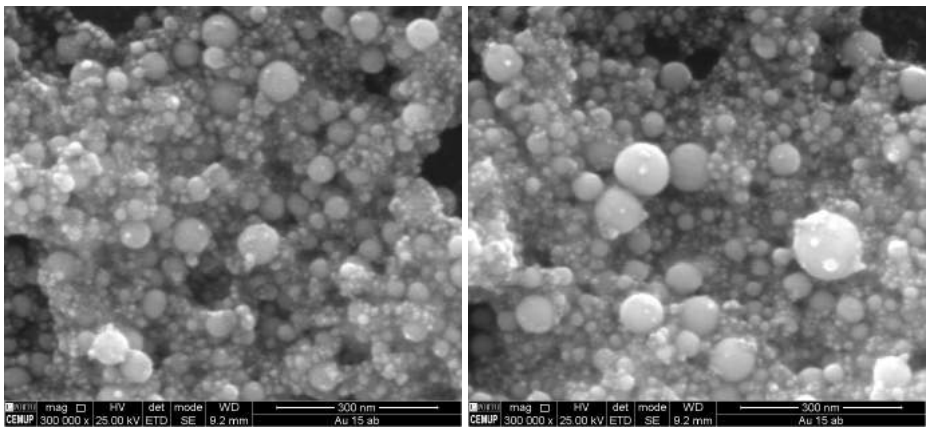

FIGURE 5.9: SEM images of the Au-NPs synthetized via fs LAL of a gold target in ethanol.

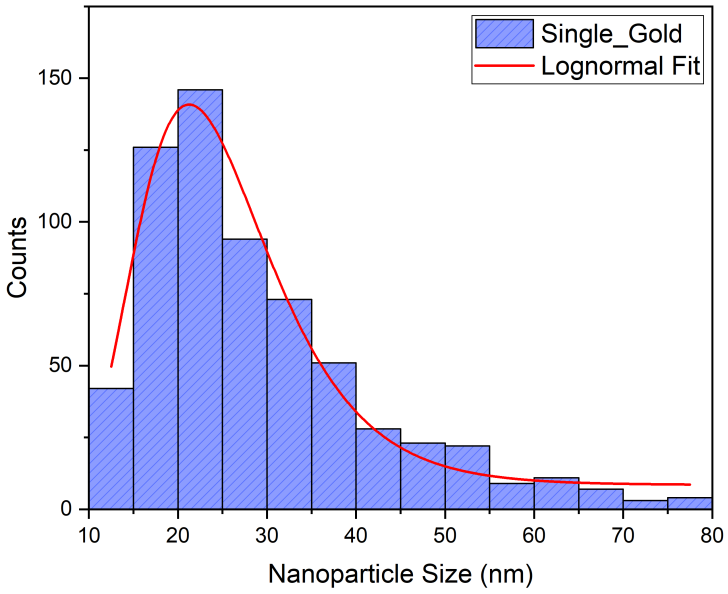

FIGURE 5.10: Size distribution of the single gold nanoparticles produced by fs LAL fitted by a logNormal function. The particles had an average size of 24 nm $\pm$15 nm.

5.1.1.3 Single Iron Nanoparticles with β-CicloDextrins

Even though we successfully produced single-iron nanospheres, their average size is one order of magnitude bigger than the ideal for applications in magnetic hyperthermia. As described in section 3.3.1, single-domain nanoparticles are the best candidates and, for iron, the critical size in which the nanoparticles become single domain is around 15 nm . In an attempt to reduce the nanoparticle size range, we try to ablate the bulk iron target in a solution containing β-cyclodextrins.

Cyclodextrins (CD) are one kind of oligosaccharides composed of glucose subunits. The molecule has a ring-shaped format and the number of subunits defines their type. The three main types of cyclodextrins are the α, β and γ containing, respectively, 6, 7 and 8 glucose monomers. In the literature there are several reports that demonstrated a significant improvement in size reduction and stability of nanoparticles in a colloidal when CD are employed [60].Although most of these reports are related to the production of gold nanoparticles, we decide to reproduce the experiment with an iron target hoping we achieve a size reduction as well. β-CD, being the most effective regarding size reduction, were the ones used in the ablation [60]. In this stage the ablation was carried out with the same bulk target, polished and cleaned again, during 60 minutes with a pulse energy

$\sim$0.160 mJ. The selected media, instead of ethanol, was ultra-pure water containing 10 mM de β-CD, as the protocol suggested [60]. Immediately after the ablation the solution presented a yellowish tone which remained stable for several days (Figure 5.11).

FIGURE 5.11: Resulting solution obtained immediately after the fs LAL of iron target in pure water with β-CD (left); The same solution 12 days later (right).

The resulting particles are shown in Figure 5.12. As it is possible to observe, the obtained SEM images in this experiment were not so clear as the ones presented before. This is related to the fact that the particles were involved in a non-identifiable matrix that we suspected to be the CDs themselves. Since the contour of the nanoparticles was neither so clear nor well defined, the measurement of their sizes could not be done in such detail. In fact, a significant number of the smallest observable particles are not included in the histogram due to the blur in their contours. However, even taking into account only the measured particles we can state that we successfully synthesized spherical iron nanoparticles with significantly smaller dimensions, with an average size of 43 nm and standard deviation of 25 nm. Their size distribution is presented in Figure 5.13.

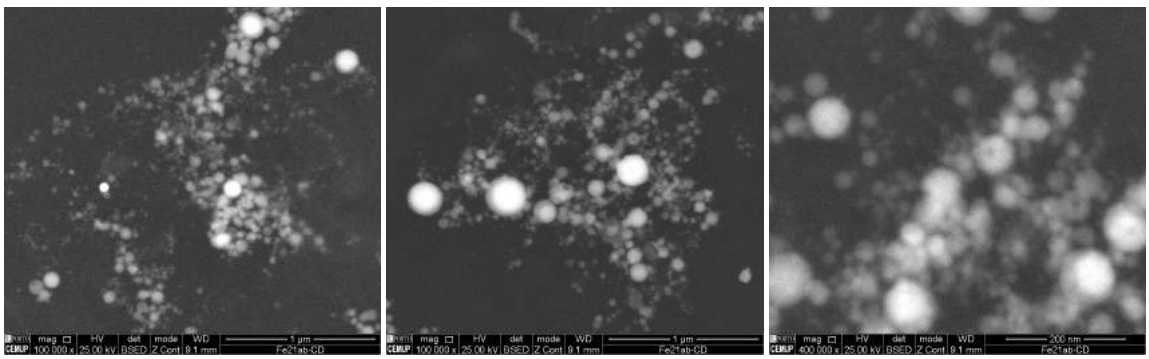

FIGURE 5.12: SEM images of the Fe-NPs synthetized by fs LAL of an Iron target in a ultra-pure water solution containing β-CD.

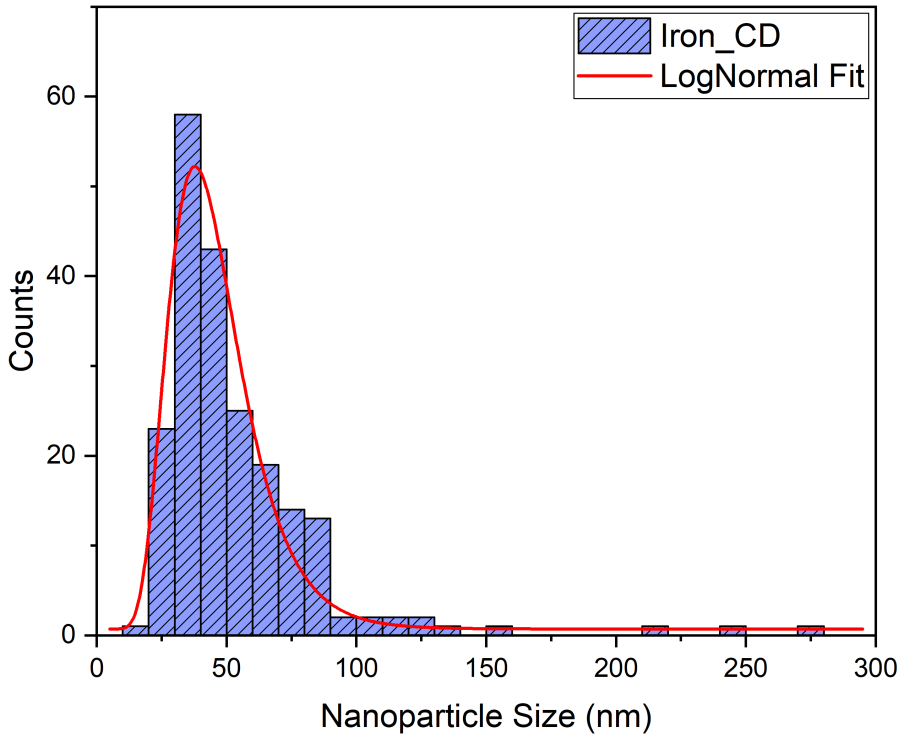

FIGURE 5.13: Size distribution of the iron nanoparticles produced by fs LAL in ultra-pure water with β-CD fitted by a logNormal function. The nanoparticles presented an average size of 43$\pm$25 nm.

Taking into account the results of the experiment, we can affirm that the use of β-CD during ablation allowed to successfully reduce the size of the particles. Compared to the previous ablation on the iron target in ethanol, the mean particle size was an order of magnitude smaller. Although we did not obtained a large number of nanoparticles with the ideal 15 nm, their dimensions are already quite close to this value, at least in the same order of magnitude.

In order to investigate the magnetic behavior of such nanoparticles SQUID M(H) measurements were acquired covering temperatures from 5K to 300K. The results are presented in Figures 5.14 and 5.15.

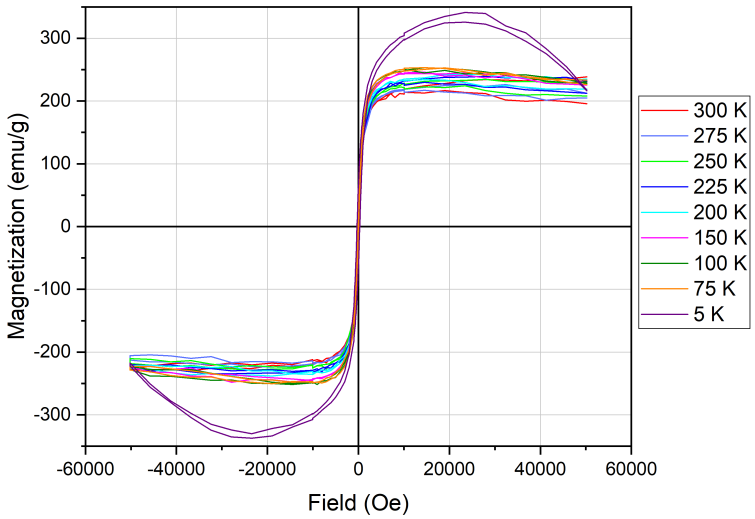

FIGURE 5.14: M(H) SQUID measurements obtained for the iron nanoparticles produced by fs LAL in ultra-pure water with β-CD.

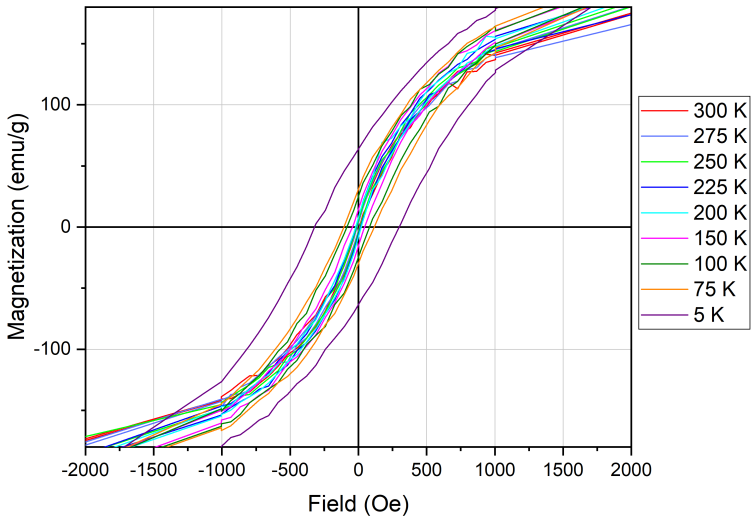

FIGURE 5.15: M(H) SQUID measurements obtained for the iron nanoparticles produced by fs LAL in ultra-pure water with β-CD.

Here, the magnetization values are normalized to the mass of the nanoparticles. As its mass could not be measured directly, a value was estimated taking into account their saturation magnetization, in emu Since the latter depends on the amount of iron present in the sample, the nanoparticle mass was estimated by:

$$1\ g \rightarrow 273.15\ emu \tag{5.1}$$

$$x\ g \rightarrow 6.737 \times 10^{-4}\ emu \tag{5.2}$$

$$x\ g = \text{Nanoparticle estimated mass} = \frac{6.737 \times 10^{-4}\ emu \cdot 1\ g}{237.15\ emu} = 2.841 \times 10^{-6}\ g \tag{5.3}$$

where 237.15 emu is a known value for iron's saturation magnetization (the one obtained in the bulk target), 6.737×10^{-4} emu is the saturation magnetization of the nanoparticles and x, the unknown value, is the estimated nanoparticle mass. The estimated value, used to normalize the magnetization, was 2.841×10^{-6} g. Another feature noticeable on Figure 5.14 is the fact that the 5K curve behaves differently from the others from $\sim$ 2000 Oe onwards. Here the eliminated diamagnetic component must contain some non-linear contribution that we cannot explain based on the obtained data alone.

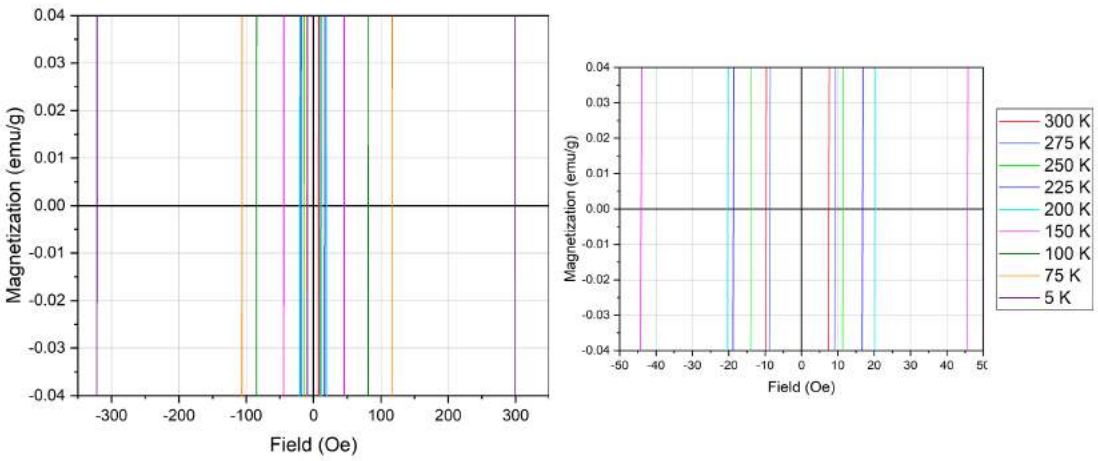

FIGURE 5.16: M(H) SQUID measurements.

The coercive fields obtained for the different temperatures are presented in Figure 5.16. Analyzing the figure one can see that the H_c field decreases as the temperature increases. The remnant magnetization, M_R, in its turn, follows a similar tendency, decreasing its

value with temperature (Figure 5.15). All the obtained values were organized in Table 5.1 and plotted in Figure 5.17.

Temperature (K)	H_c (Oe)	M_R (emu/g)
5	299.28	63.77
75	116.99	30.58
100	81.75	24.77
150	45.82	14.12
200	18.22	7.91
225	15.89	7.47
250	11.43	5.31
275	8.92	3.29
300	7.39	3.86

TABLE 5.1: Coercive Field and Remnant Magnetization values for each covered temperature.

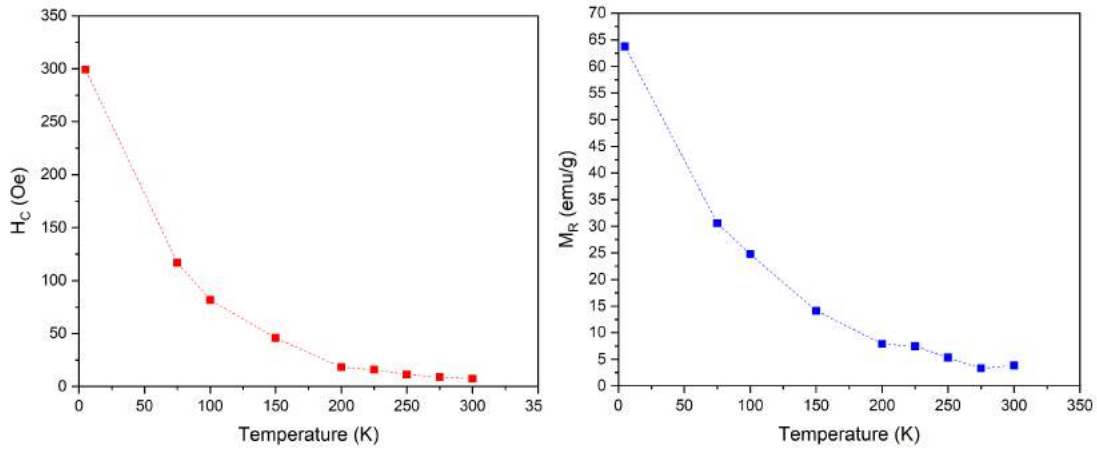

FIGURE 5.17: Coercive field and remanent magnetization values plotted as a function of temperature.

The fact that M(H) measurements present coercive fields and remnant magnetization in all the acquired temperature range suggests that the nanoparticles are ferromagnetic and the superparamagnetic state was not reached. This is an expected result as in the size

distribution histogram one can see that the nanoparticles have dimensions superior to the single domain limit around 15 nm for iron.

5.1.1.4 Single Gold Nanoparticles with β-CicloDextrins

Here the ablation was performed replicating the conditions of the previous one, but with the gold target, that was also polished and cleaned before the ablation. Once more the ablation was carried out with a fs laser, during 60 minutes with a pulse energy of $\sim$ 0.160 m J. The selected media was ultra-pure water containing 10 mM of β-CD. Immediately after the ablation the solution presented an intense reddish tone that remained stable for several days (Figure 5.18). Two months after the ablation, the only verified change was a slight darkening of the liquid solution.

FIGURE 5.18: Resulting solution obtained immediately after fs LAL of a gold target in ultra-pure water with β-CD (left); the same solution one week later (in the middle) and two months later (right).

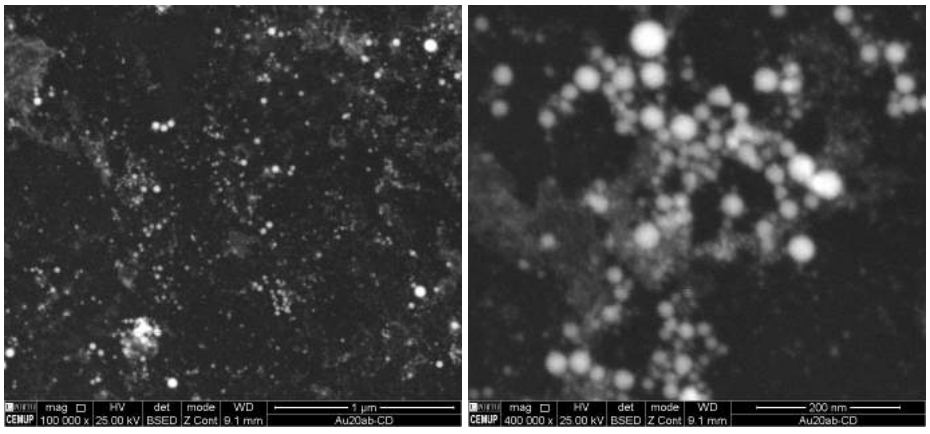

FIGURE 5.19: SEM images of the Au-NPs synthesized via fs LAL of a gold target in pure water with β-CD.

The produced nanoparticles can be seen in the SEM images presented above on Figure 5.19. Just like the nanoparticles obtained in the ablation of the iron target with CD, these ones were also involved in the same matrix that prevented a fully clean view of their contours. However, it is possible to observe that sphere nanoparticles were successfully achieved. Their size distribution, along with the spectrum obtained by UV-Vis analysis are presented in Figure 5.20.

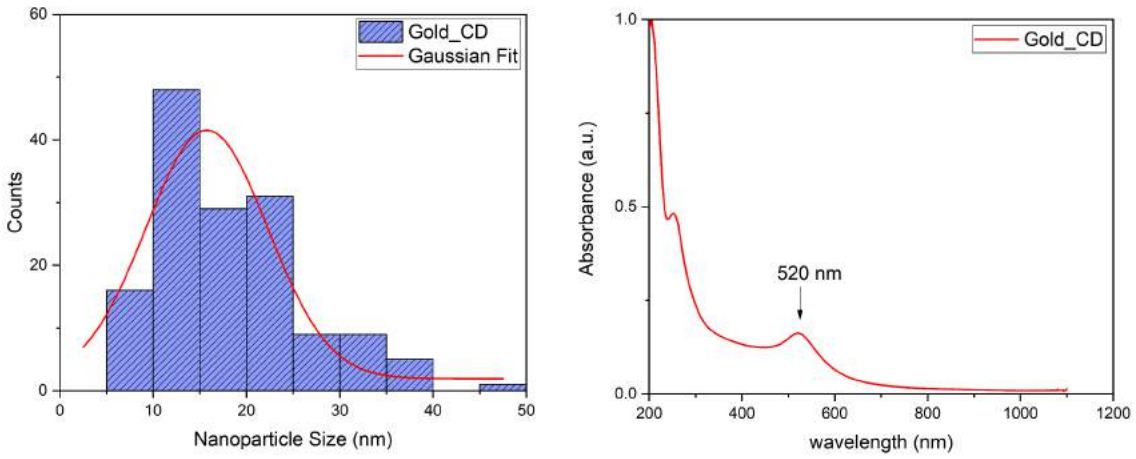

FIGURE 5.20: Size distribution of the gold nanoparticles produced by fs LAL in ultrapure water with β-CD. The histogram has a Gaussian fit and the nanoparticles presented an average size of 16±13 nm (left) ; Nanoparticles UV-Vis spectrum showing a SPR peak at 520 nm (right).

The gold nanoparticles presented an average size of 15.754±13.052 nm, smaller when compared to the one obtained in the ablation of the gold target in ethanol (∼24 nm). The UV-Vis analyses showed that they strongly absorb light around 520 nm, due to the presence of a resonant surface plasmon excitation. This SPR value is in agreement with the literature, being related to a gold chemically stable colloid with nanoparticle dimensions inferior to 30 nm [61].

5.1.2 Thin-films target ablations

As shown in the previous sections, the goal of producing single iron and gold nanoparticles has been successfully fulfilled. Then, following the work plan, we move on to the next objective, which was the production of nanoparticles with more complex morphologies. For this, instead of ablating a bulk target of each material, we started to ablate a thin-film targets whose deposited layers had different arrangements of gold and iron, above a glass substrate.

In order to deposit the gold layers the used technique was DC Sputtering electrodeposition. Here, deposition took place in several sessions of 300 seconds until reaching the desired thickness. The deposition rate was about 0.058 nm/s, so that with two consecutive sessions of 300s a film of approximately 35 nm thickness was obtained. For every two 300s sessions in a row, an interval of one hour had to be taken before the next deposition. The iron, on the other hand, was deposited using the thermal evaporator in the clean-room of the Micro and Nanofabrication Unit (MNTEC) facilities. In the latter, the deposition rate was about 0.019 nm/s.

In this step, different numbers of layers and material deposition orders were tested. The ablation was carried out with the target laying on the beaker that was filled with $3-5$ m m of ultra-pure ethanol or acetone. In this case, as we intended to ablate the entire substrate, instead of using the rotating support, we manually controlled the support where the ablation was taking place. What I mean by this is that we manually moved the position of the beaker until the laser had traveled across the entire surface of the target. As the laser hit the target, the thin-film material was visually extracted so the ablation ended up when the target only contained the glass substrate layer with minimal deposited material (Figure 5.21). This procedure took about 10 minutes. The energy of the laser pulse was also reduced, becoming approximately one third of those ablations related to the bulk target. To sum up, the ablations were carried out in thin-film targets with a fs laser with a pulse energy $\sim$0.050 mJ during $\sim$10 minutes in 3-5 mm of ethanol and acetone.

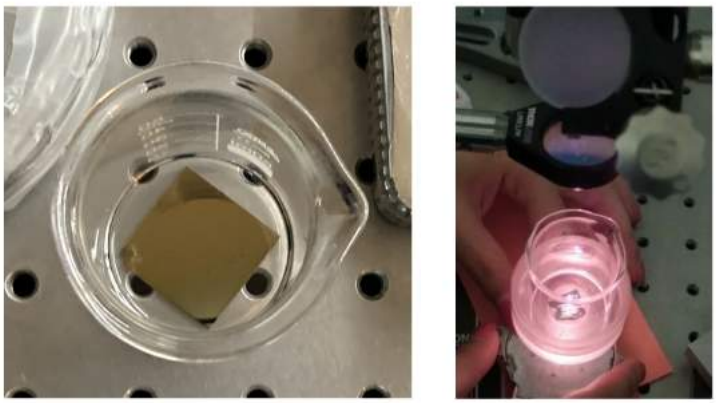

FIGURE 5.21: Thin-film target in the beaker (left); LAL with a manual control of the target position (right).

5.1.2.1 Iron and Gold - Two layer combinations

The first tests with thin-film targets were made with two layers of deposited material, whose order of deposition of iron and gold was alternated. In order to be easier to identify the type of target used in each case, relatively the order of deposition, a nomenclature will be fixed. From the top to the bottom layers, the configurations used were Gold-Iron-glass (Au-Fe-Glass) and Iron-Gold-glass (Fe-Au-Glass) (Figure 5.22). In both cases four sessions of 300s of gold were deposited, making a thickness of about 70 nm, and 150 nm of Iron.

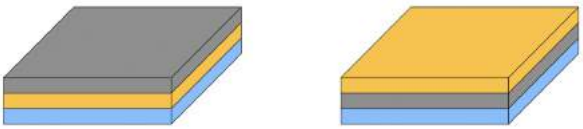

FIGURE 5.22: Thin-film targets: Iron-Gold-Glass (FeAu) and Gold-Iron-Glass (AuFe); The layer thickness was, respectively, ∼70 nm and ∼150 nm for the gold and the iron.

5.1.2.2 Gold-Iron-Glass

Here the ablation was carried out in 3mm of ethanol (99%) with a pulse energy of 0.048 mJ. In this particular case, during ablation, it was noticed that as the laser swept across the surface of the thin-film, only the top layer of gold was ablated. As many times as the laser stroked the iron layer, which at this time was already exposed, the material was not ablated. This can be seen in Figure 5.23.

(A) (B) (C) (D)

FIGURE 5.23: (A) Thin-film target immediately before ablation; (B) Thin-film target after the ablation with the iron layer still practically intact; (C)Resulting Solution presenting a pink/reddish tone; (D) Air exposed target reveling signs of oxidation only a few minutes post LAL.

Figure 5.23 presents, on the left side, the appearance of the target immediately before the ablation. The target was already positioned in the beaker and immersed in ethanol. Immediately after ablation it is possible to see that the solution acquired a pink/reddish tone. However, looking carefully at the target one can see that the iron layer remained practically intact regardless the number of times it was hit by the laser (Figure 5.23b). The resulting solution was then removed from the beaker and stored in an eppendorf (Figure 5.23c). Just a few minutes after ablation, the air exposed target showed signs of oxidation represented by the acquired orange tone (Figure 5.23d).

As can be seen in the SEM images related to this experiment (Figure 5.24), this order of deposition did not allow the synthesis of nanoparticles. Instead, the images lead to the idea that material was extracted in several splinter-shaped pieces. Observing the flakes with a larger magnification (20000x), it is possible see some particles still semi-aggregated to the material.

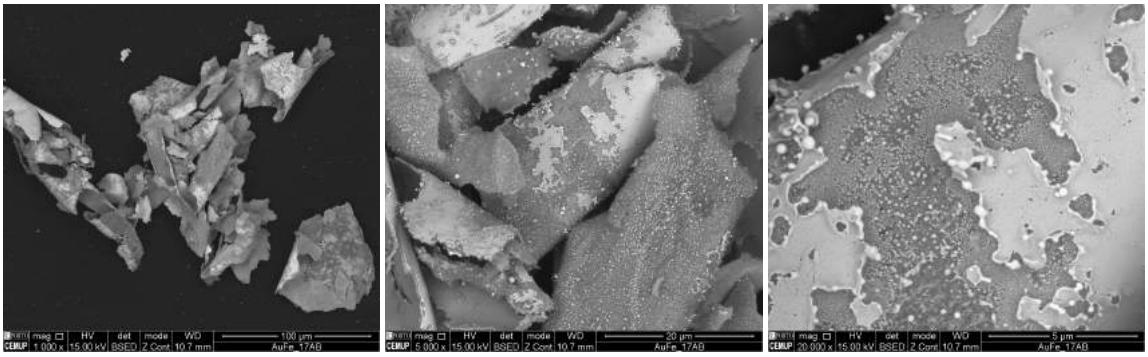

FIGURE 5.24: SEM images showing the results of the fs LAL of a thin-film target (Gold-Iron-Glass) in ethanol.

5.1.2.3 Iron-Gold-Glass

At this stage, the conditions of the previous experience were replicated. The only difference was related to the target that had the materials deposition order reversed. From the top layer to the bottom, the order of deposition was Iron-Gold-Glass. The shape of the target was also different, instead of ablating an well-defined square target, we successively ablate 4 irregularly contoured pieces that had the same deposited material (150 nm of Iron on top of 75 nm of Gold). The solution remained the same for the four ablations and the target was replaced as soon as the deposited material had already been removed by the fs laser. In Figure 5.25 one can see the appearance of the targets immediately after their ablations. Contrary to the results of the previous experience, immediately after the

ablation the targets already presented an almost totally transparent look. This means that both layers were successfully ablated leaving only the glass substrate layer.

FIGURE 5.25: Appearance of the thin-film (Iron-Gold-Glass) targets post-LAL.

After the ablation of each target, a small magnet was placed next to the beaker (Figure 5.26). With this it was possible to observe the particles travelling in its direction and crowding right above it.

FIGURE 5.26: Placing a magnet next to the beaker in order to visualize the particles traveling towards it.

The final solution, gathering the materials of the four ablations, is presented in Figure 5.27a, revealing an intensive red and grey tone. As the days went by, the same material that we saw traveling towards the magnet during the ablation was depositing at the bottom of the eppendorf (Figure 5.27b). The placement of a magnet post-LAL next to the solution enhanced the sedimentation process at the bottom of the eppendorf and, as the material was deposited, the solution acquired a stronger pink tone. Here, the gray undertone that came from the magnetic particles still being suspended in the solution was vanishing over time (Figure 5.27c).

(A) (B) (C)

FIGURE 5.27: (A) Resulting solution obtained by the fs LAL of a thin-film (Iron-Gold-Glass) target immediately after the ablation; (B) Same solution 24 hours later with some sedimentation due to placing a magnet next to the eppendorf; (C) Same solution one week later presenting an enhanced pink/reddish tone.

The SEM images related to this experiment are shown in Figure 5.28. Here it is possible to see that even though flakes were also obtained (left), nanoparticles were successfully synthesised (right).

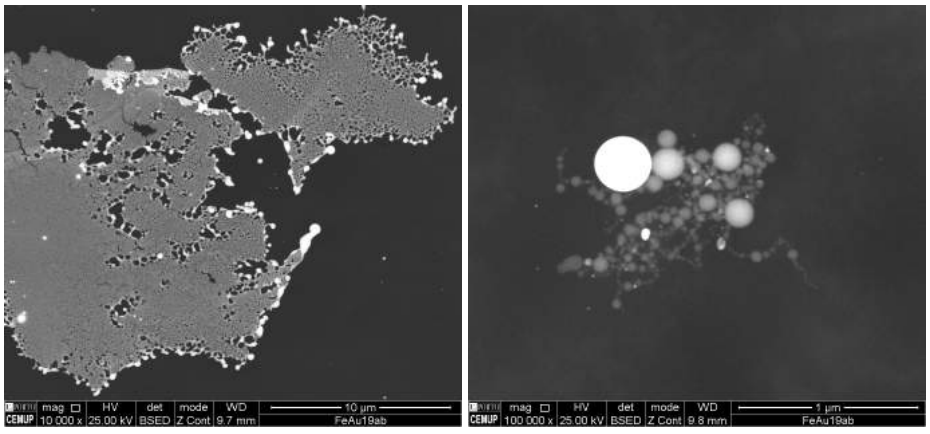

FIGURE 5.28: Results of the femtosecond laser ablation of a thin-film target in ethanol.

The histogram of size distribution of the nanoparticles, along with the spectrum obtained by UV-Vis analysis, are presented in Figure 5.29. The nanoparticles presented an average size of 42 nm. The UV-Vis analyses, in its turn showed that they strongly absorb light around 540 nm, due to the presence of a resonant surface plasmon excitation.

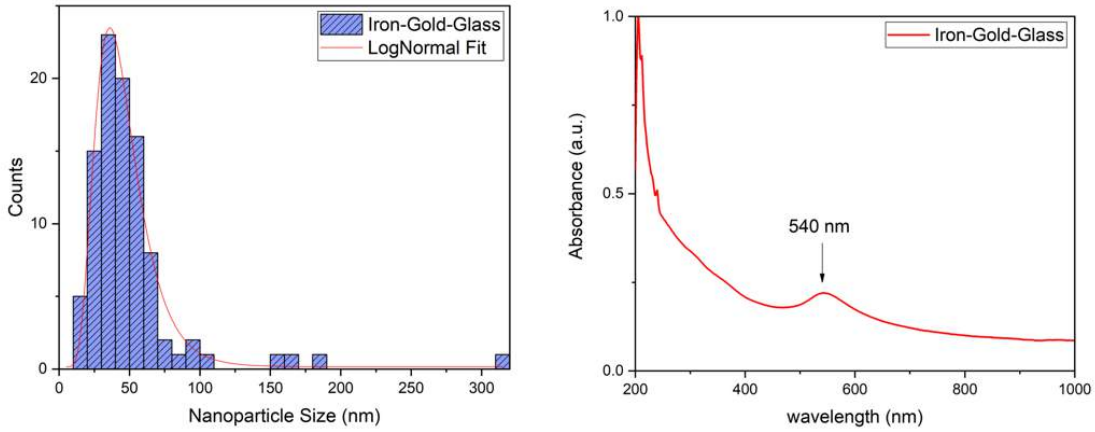

FIGURE 5.29: Size distribution of the particles produced by fs LAL of thin-film (Iron-Gold-Glass) target fitted by a logNormal function. The particles presented an average size of 42 nm (left); UV-Vis spectrum showing an SPR peak at 540 nm (right).

5.1.2.4 Three layer combinations

At this stage the ablation was performed in a thin-film target with three layers of material deposited on top the glass substrate. Here, the chosen deposition order was based on the results obtained in the previous two-layer ablations. As shown, placing the iron layer directly on top of the glass was not a viable option, since it demonstrated a very high adhesion to the substrate that the laser was unable to remove. On the other hand, the iron layer exposed directly to the air showed rapid signs of oxidation. In parallel to this, the synthesis of nanoparticles was only possible when the iron was on top of the gold layer and, with this configuration, all the material was removed from the substrate. Taking all these points into account, the chosen order of deposition was Gold-Iron-Gold-Glass (Figure 5.30). In this way the iron is not directly on top of the substrate and at the same time is protected from oxidation by gold. In this case all the three layers had the same thickness of $\sim$ 40 nm.

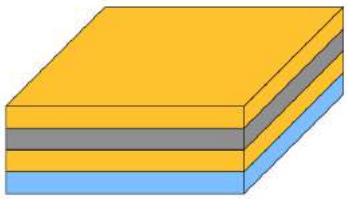

FIGURE 5.30: Thin-film target with e deposited layers (Gold-Iron-Gold). Each layer had 40 nm of thickness.

As in previous thin-film experiments, the ablations were carried out with a fs laser with a pulse energy of ∼0.050 mJ during ∼10 minutes. At this time, in an attempt to also evaluate the influence of the liquid solution on the morphology of the synthesized nanoparticles, two ablations were performed with the same experimental conditions, varying only the liquid solution. The selected media were acetone (99%) and ethanol (99%) with a thickness of 3 mm above the target.

5.1.2.5 Gold-Iron-Gold in ethanol

SEM images relative to the LAL of the three layers in ethanol are shown in the Figure 5.31, where one can see that numerous spherical nanoparticles were synthesized with this Gold-Iron-Gold configuration. By looking carefully at the images, it is quite visible that a significant number of the nanoparticles present simultaneously two shades, a whiter/-clear and a gray/darker tone. Since the contrast in the SEM images, using the backscattered eletrons mode, is related to the difference in atomic number of the specimens, this means that there is a possibility that we have successfully synthesized nanoparticles composed simultaneously of the two elements.

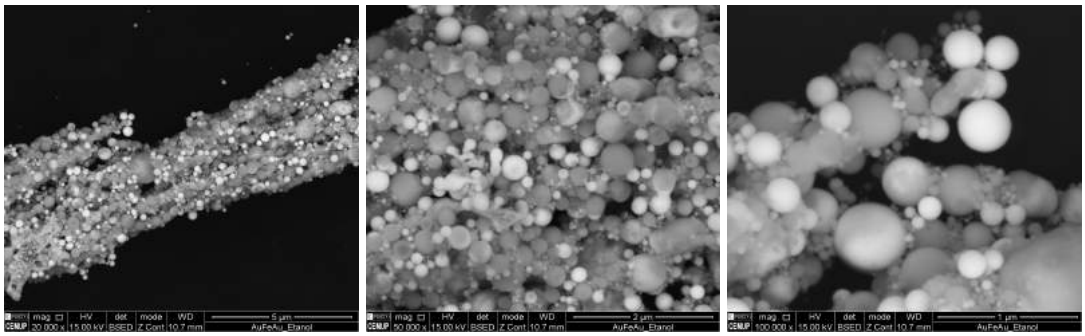

FIGURE 5.31: SEM images of the nanoparticles synthesized by fs LAL of a thin film target (Gold-Iron-Gold) in ethanol.

This hypothesis was supported by the EDS analysis. In Figure 5.32 it is possible to see that the same particle presented two peaks, one relative to the presence of gold and the other to iron. Although it is not possible to infer regarding the morphology of the obtained nanoparticles, i.e if they are under the alloy or core-shell regime, we can state that it was possible to synthesize nanoparticles composed simultaneously of the two elements. In the EDS graphics it is also possible to see that the measured nanoparticles have different fractions of iron and gold. For a more detailed analysis of their structure, we would have to resort to other characterization techniques such as transmission Electron Microscopy

(TEM) which unfortunately we did not have access to. In the EDS analysis graphs a small peak that indicates the presence of copper in the sample is also observable, indicating a slightly contamination. The carbon peak comes from the carbon tape used in sample preparation.

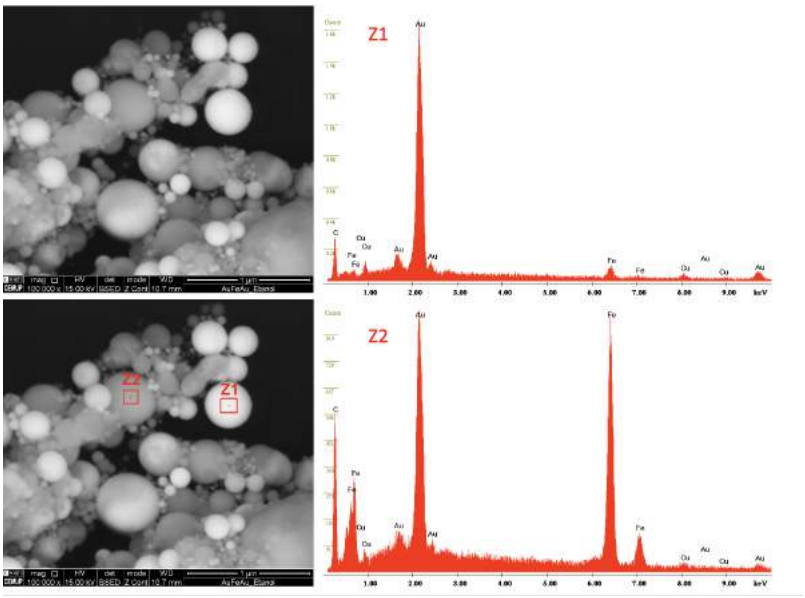

FIGURE 5.32: EDS analysis of the nanoparticles synthesized by fs LAL of a thin-film target (Gold-Iron-Gold) in ethanol.

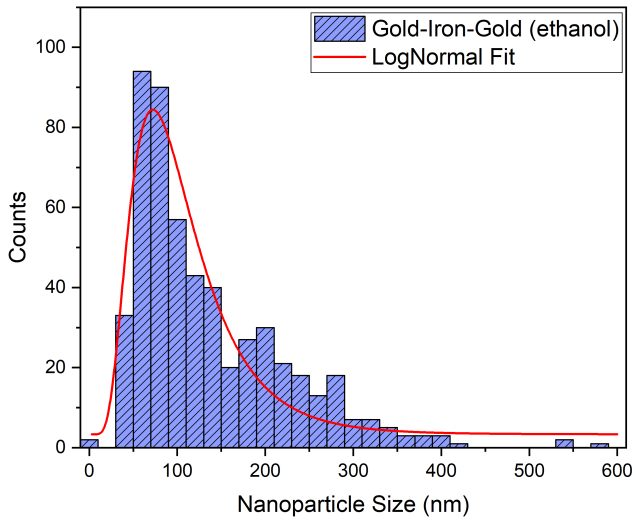

FIGURE 5.33: Size distribution of the particles produced by fs LAL on thin-film (Gold-Iron-Gold) target in ethanol fitted by a logNormal function. The particles presented an average size of $95 pm 58$ nm

The size distribution of the nanoparticles is presented in Figure 5.31. Their average size was 95 nm with a standard deviation of 58 nm.

Immediately after the ablation, the solution presented a pink/reddish tone similar to the one already seen in the previous experiments (Figure 5.34). Once more the application of a magnet post-LAL allow the visualization of the magnetic particles travelling in its direction. However, just 8 days after the ablation, all color had faded. This means that, under these experimental conditions, ethanol did not prove to be an ideal solution with regard to the temporal stability of the sample. In fact, when the UV-Vis analysis of this sample was performed, no SPR peaks were detected. Note that while SEM images were obtained 4 days after ablation, the UV-Vis spectrum was obtained several days later with the already transparent solution.

It is also important to refer that before each UV-Vis measurement or sample preparation for SEM, the solution was placed on the vortex during 1-2 minutes. This process was not carried out only in SQUID measurements, as it was favorable to gather as much magnetic material as possible. Since this magnetic material was normally deposited at the bottom of the eppendorf due to placing a magnet on its side, to prepare the SQUID sample we only tried to remove as much of the liquid solution as possible, leaving only a few drops surrounding the material.

FIGURE 5.34: Resulting solution obtained immediately after fs LAL on thin-film (Gold-Iron-Gold) target in ethanol; The same solution 8 days later.

A picture of the thin-film target after the ablation is presented in Figure 5.39 . Here one can see that all the three deposited layers were easily removed from the glass substrate with the femtosecond laser.

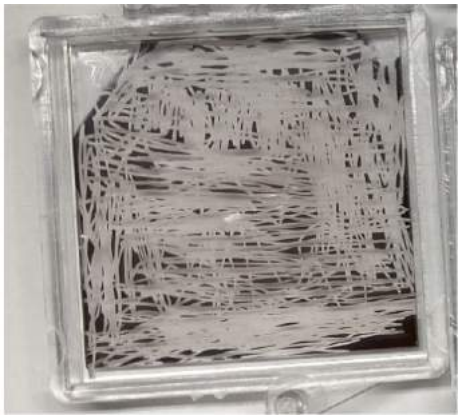

FIGURE 5.35: Appearance of the target post LAL.

Lastly, to investigate the magnetic behaviour of the obtained nanoparticles, SQUID M(T) measurements were acquired for a 100 Oe field. Here, the measurement of the magnetization as a function of temperature was done following the zero-field-cooling (ZFC) and field-cooling (FC) protocol. As describe in section 4.2.2 this kind of analysis provides information regarding the blocking temperature (T_B) and particle size distribution. The results are presented in Figure 5.36.

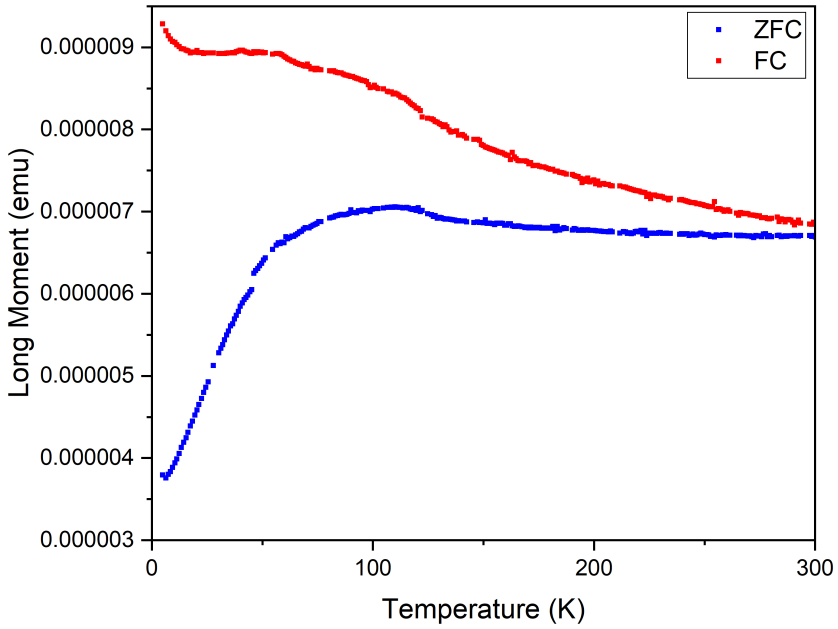

FIGURE 5.36: Temperature dependence of the magnetization (ZFC and FC) over the temperature range 5-300K with H=100Oe for the nanoparticles synthesized by fs LAL of thin-film (Gold-Iron-Gold) target.

In order to estimate the T_B value, the next step was to plot the d(M_{FC}-M_{ZFC})/dT as a function of temperature and see what was the temperature related to the maxima of the obtained function.

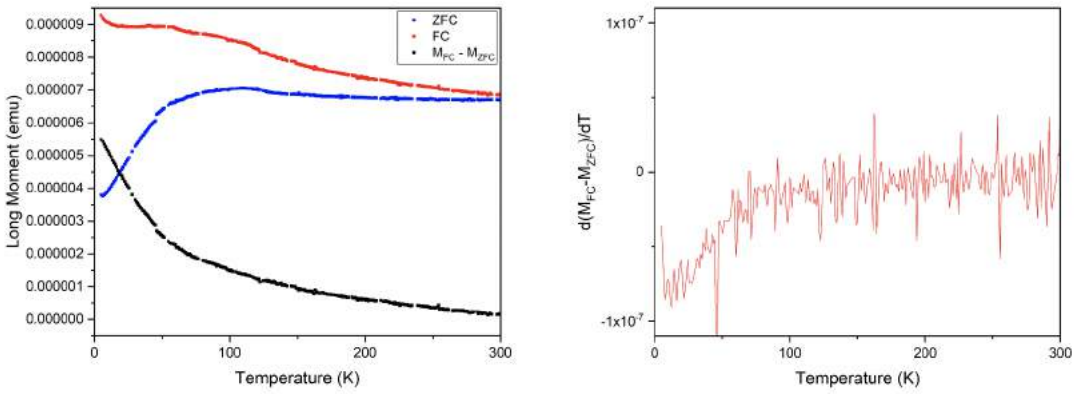

FIGURE 5.37: Determination of the blocking temperature (T_B) by the temperature derivative of the difference between the FC and ZFC magnetization curves.

However, as it can be seen in Figure 5.37, the results did not allow to obtain this maxima peak value. On one hand the results show that the sample remains in the block state until room temperature (300K), as indicated by the non-convergence of the FC and ZFC curves. On the other hand, the fact that there is not a peak representing the T_B can be possibly explained by the wide size distribution of these nanoparticles (Figure 5.33) When nanoparticles have a large size distribution, they will also consequently have a wide distribution regarding the blocking temperature. This means that, unlike the narrow size distribution case where all the particles have similar dimensions and are unblocked in a small temperature interval that can be represented by a peak, a larger temperature range that encompasses the entire distribution is needed. In fact, taking into account the size distribution histogram, it is actually expected to not have a blocking temperature peak because the sufficiently small dimensions to pass to superparamagnetic regime were not reached. If this regime had actually been reached, in the ZFC curve zone after T_B, the magnetization would drop to zero since for temperatures above this threshold the thermal energy would be enough to disturb the system randomizing the spins and therefore reducing the magnetization.

5.1.2.6 Gold-Iron-Gold in acetone

Here, the ablation was performed replicating the experimental conditions of the former experiment, changing only the liquid solution in which the target was immersed. Just to recall, the ablation was carried out in a three layer (Gold-Iron-Gold) thin-film target with a fs laser with a pulse energy of ∼0.050 mJ during ∼10 minutes. The liquid solution was acetone (99%).

Similarly to the ablation performed on ethanol, the resulting solution obtained immediately after the ablation present a pink/reddish tone and, once more, the application of a magnet post-LAL allowed the visualization of the magnetic particles travelling in its direction. However, contrary to the same, the acetone solution remained stable over time without any color fading (Figure 5.38). The appearance of the thin-film target after the ablation is presented in Figure 5.39, where it is possible to see that all the three deposited layers were also easily removed from the glass substrate with the femtosecond laser.

FIGURE 5.38: Resulting solution obtained immediately after fs LAL on thin-film (Gold-Iron-Gold) target in acetone (left); The same solution 8 days later (middle); The same solution 12 days later (right).

FIGURE 5.39: Appearance of the target post LAL.

SEM images of the produced nanoparticles are presented in Figure 5.40. Just like the ones obtained in ethanol, the nanoparticles presented two shades suggesting that they are

composed simultaneously of the two materials.

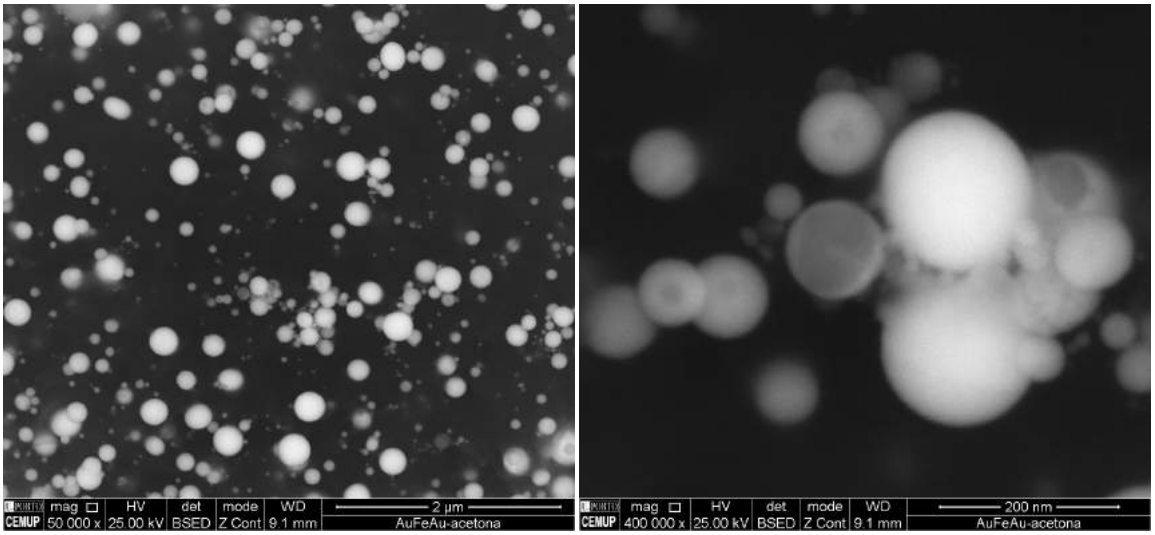

FIGURE 5.40: SEM images of the nanoparticles synthesized by fs LAL of a thin film target (Gold-Iron-Gold) in acetone.

The size distribution of the particles, along with their UV-Vis analysis are presented in Figure 5.41. In this case, the nanoparticles presented an average size of 109.86 nm. The UV-Vis analyses, in its turn, showed that they strongly absorb light around 560 nm, due to the presence of the SPR peak.

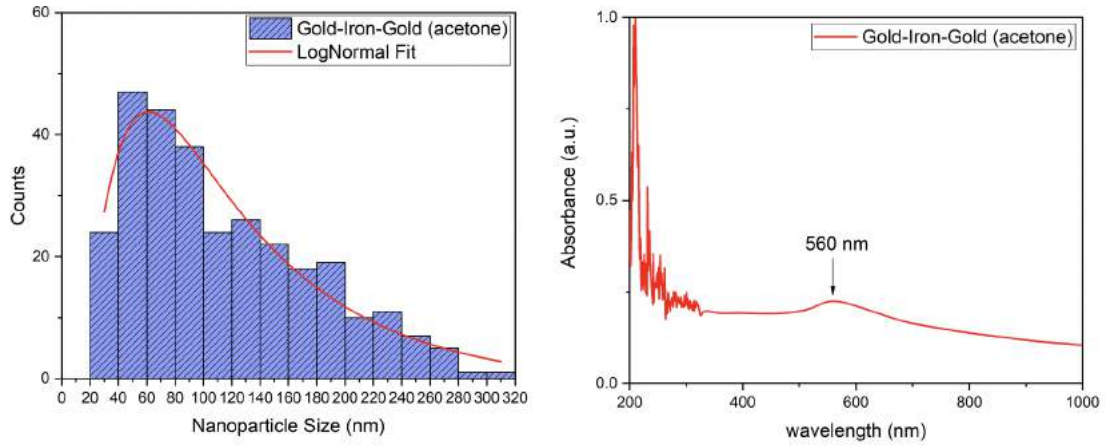

FIGURE 5.41: Size distribution of the particles produced by fs LAL of thin-film (Iron-Gold-Glass) target fitted by a logNormal function. The particles presented an average size of 109 nm and a standard deviation of 159 nm (left); UV-Vis spectrum showing an SPR peak at 560 nm (right).

Lastly, SQUID measurements were obtained to infer about the magnetic behavior of the synthesized nanoparticles. Here both M(H) and M(T) measurements were acquired. The M(H) measurements are presented in Figure 5.42 where one can see the hysteresis loop of such nanoparticles in the 5-300K temperature range. On the left, the magnetization values are still presented in emu, and the saturation magnetization value for the 300K curve (M_s = 4.37×10^{-4} emu) was used to obtained the mass of the synthesized magnetic material as previously explained in section 5.1.1.3. This value (m=1.843×10^{-6}) was then used to normalize the magnetization. The obtained coercive fields and the remnant magnetization values are organized on the table 5.2 and can be seen with more detail in in Figure 5.43.

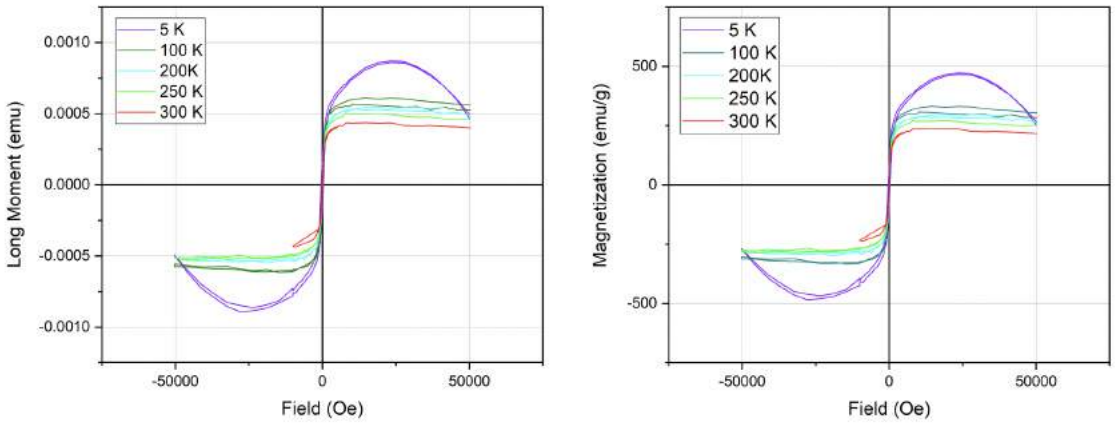

FIGURE 5.42: M(H) SQUID obtained measurements.

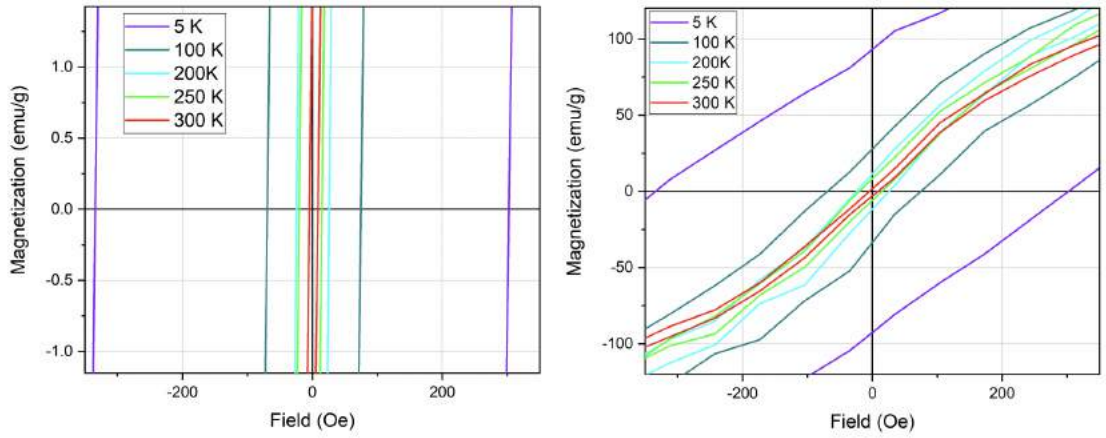

FIGURE 5.43: Obtained coercive fields and the remnant magnetization values.

Temperature (K)	H_c (Oe)	M_R (emu/g)
5	302.32	93.15
100	75.10	27.65
200	25.92	11.77
250	14.65	8.24
300	8.07	1.62

TABLE 5.2: Coercive Field and Remnant Magnetization values for each covered temperature.

Once more the H_c fields and M_R values decrease as the temperature increases. Based on these results, it is possible to see that for all the covered temperatures, the M(H) curves still present an area of hysteresis characterized by the width of the coercive fields and non-zero remanent magnetization values suggesting that under these conditions the particles present a ferromagnetic behavior.

The M(T) measurements, in its turn, are presented in Figure 5.44.The fact that the $M_{ZFC}(T)$ and $M_{FC}(T)$ curves do not overlap in the whole temperature range of the measurements, together with the existence of hysteresis in the magnetization vs applied field, M(H), curves at 300 K imply that in fact the system has not reached the superparamagnetic regime.

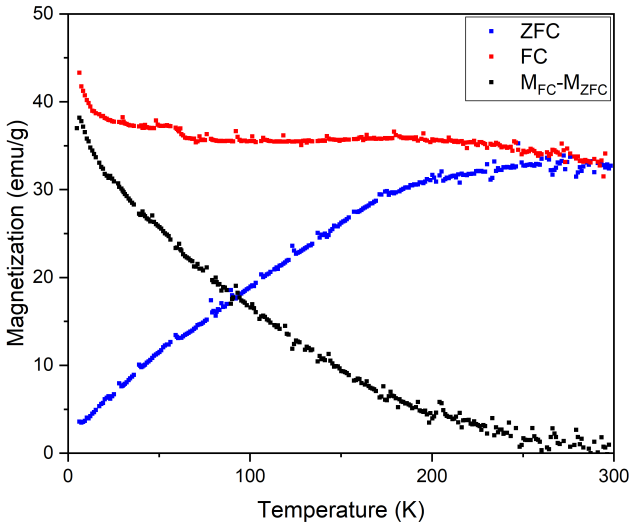

FIGURE 5.44: The M(T) measurements.

Analyzing all the characterization methods obtained for these particles, and relating them to the main objective of this work, which was the production of nanoparticles that are efficient in the conversion of energy into heat, there are some points of view that should be addressed. Firstly, in all cases, the results suggest that the superparamagnetic regime was not reached and at room temperature (300K) the synthesized nanoparticles are ferromagnetic. On one hand the superparagnetic regime can be an advantage because, by definition, superparamagnetic particles have zero coercivity and zero remnant magnetization, meaning that there is no net magnetostatic field from the nanoparticles. This means that the nanoparticles do not interact with each other and agglomeration due to magnetic interactions does not occur, enabling stabilisation in solution. For this reason, superparamagnetic particles are often considered to be desirable for biomedical applications. On the other hand, recalling Figure 3.6, that demonstrates the effectiveness of nanoparticles in terms of SAR, one can see that these regime is not the ideal for the magnetic hyperthermia case. Here, single-domain particles whose size is close to the single/multi-domain transition are desirable due to high SAR values. Even though the obtained nanoparticles are still not in this size range, when comparing the SAR for multi-domain ferromagnetic nanoparticles (our case) with the superparamagnetic one, the values are much superior suggesting that the synthesized nanoparticles should be more efficient in this kind of application. The agglomeration issue can perhaps be overcame through a subsequent strategic functionalization of the particles.

5.1.2.7 DLS/Zeta Potential Measurements

For all the experiments in which nanoparticles were successfully synthesized by femtosecond laser ablation in liquids, DLS measurements were acquired. However, in general, these measurements were not accurate regarding the size distribution of the nanoparticles. In other words, when comparing the data obtained by DLS with the size distribution taken from the SEM images, the values relative to the nanoparticle size do not match. In fact, the DLS data presents significantly larger values in all cases.

A good example illustrating this is shown in Figure 5.45 regarding the single-gold produced nanoparticles by the ablation of a bulk target in ethanol (section 5.1.1.2). While the DLS data show peaks that indicate several population groups with different average nanoparticles sizes of $\sim$165 nm, $\sim$400 nm and $\sim$715 nm, the histogram obtained by directly measuring the nanoparticles size on the SEM images presents a much inferior value

of ∼24 nm. This could be a consequence of the agglomeration of the nanoparticles. Hereupon, the DLS may not have sufficient sensitivity to distinguish between an individual particle and a population of agglomerated particles, hence assuming larger average sizes.

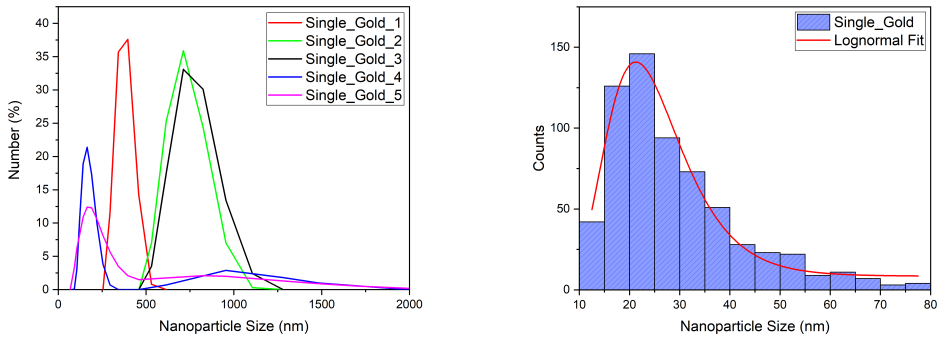

(A) (B)

FIGURE 5.45: (A) DLS data obtained for the single-gold nanoparticles, presenting different average nanoparticles sizes of ∼165 nm, ∼400 nm and ∼715 nm) (B) Histogram of the same nanoparticles obtained by directly measuring their size in the SEM images.

The measurement of the zeta potential values for both the ablations on bulk and thin-film targets are presented, respectively, in tables 5.3 and 5.4. The only case that is not included in the tables is the one related to ablation of the 3-layer thin-film target in acetone, as this material is not compatible with this type of measurement.

In general, all the solutions presented zeta potential values close to zero suggesting the presence of flocculation or coagulation in the sample due to interparticle interactions. This is in agreement with the agglomeration visible in the SEM images of all these samples, therefore confirming the higher size distribution obtained in the DLS measurments. The only sample that is not included in the 0 to ±5mV interval associated with the flocculation process is the Iron-Gold-Glass ablated in ethanol presenting a $\zeta = 24.44$mV. This one, even though is it still in the incipient stability range, it is closer to the desired ±30 mV characteristic of a stable solution.

		Zeta Potencial (mV)	Average Zeta Potencial (mV)
Thin-Film Target	Iron-Gold (ethanol)	25.1	24.44
		23.4	
		25.0	
		24.4	
		24.3	
	Gold-Iron-Gold (ethanol)	-3.29	-2.42
		-3.37	
		-0.53	
		-1.75	
		-3.16	

TABLE 5.3: Zeta-Potential values obtained in the ablation of thin-film targets.

		Zeta Potencial (mV)	Average Zeta Potencial (mV)
Bulk Target	Single Iron (ethanol)	1.08	1.30
		1.25	
		1.41	
		1.46	
		1.32	
	Single Gold (ethanol)	0.06	1.35
		-0.33	
		1.08	
		2.57	
		3.34	
	Single Iron β-CD (water)	0.01	0.09
		-0.04	
		0.12	
		0.08	
		0.28	
	Single Gold β-CD (water)	0.03	0.03
		0.01	
		0.05	
		0.09	
		-0.04	

TABLE 5.4: Zeta-Potential values obtained in the ablation of bulk targets.

Chapter 6

Gold Nanorod Photo-Induced Heating tests - Experimental Results and Discussion

This chapter includes the experimental results obtained in the photo-induced heating tests of a solution containing Gold Nanorods (AuNRs). The main goal of this work was to make a detailed analysis of the performance of these nanostructures during exposure to NIR radiation, taking into account the variation of several experimental parameters such as laser power, laser spot area, nanorods concentration and the volume of solution. The influence of each parameter was investigated regarding the sample's heating efficiency that, in its turn, was evaluated through the figure of merit Specific Absorption Rate (SAR) described in section 3.1.

6.1 Experimental Set-up/Details

Measurements were performed using a NIR continuous wave (CW) laser operating at 808 nm with a maximum output power of 2.5 W. The laser was aligned in a way that its radiation laterally crosses the walls of a glass cuvette filled with the AuNRs solution. The heating of the sample was simultaneously measured with a FLIR i7 Infrared Thermal camera and with a type-K thermocouple (Figure 6.1). The thermocouple, connected to a sourcemeter, measured the potential difference between its two extremities/tips. One of them was directly immersed in the AuNRs solution and the other was placed on an ice bath, acting as a reference. This potential difference was then converted to temperature

variation and plotted over time with a LabVIEW program given rise to the photo-induced heating curves. The equation that converted the potential difference into temperature, included in the program, was obtained from the thermocouple calibration and is given by:

$$T = 0.0823 + 26294V \tag{6.1}$$

The thermocouple calibration process included a beaker filled with water placed on a hot plate, a thermometer and a sourcemeter. As in the set-up described above, the thermocouple had one of its tips placed in an ice bath, and the other in the to be heated solution, that in this case was the water in the beaker. The water temperature values were controlled by the thermometer throughout the whole process and, as the water temperature increased, the corresponding values regarding the potential difference, read on the sourcemeter, were recorded. The recorded values were then plotted, and the equation that relates these parameters was obtained.

FIGURE 6.1: Set-up Illustration.

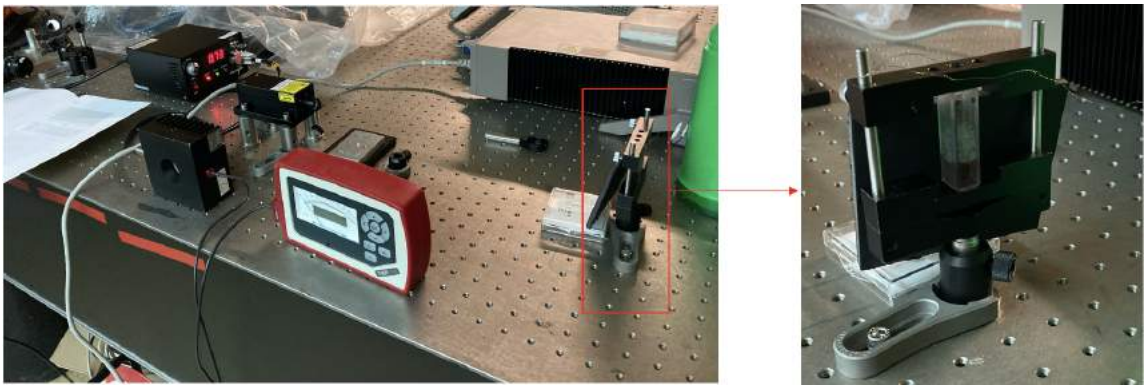

FIGURE 6.2: Photo-induced heating tests with CW 808 nm laser set-up.

The used organic-coated gold nanorods (10x41nm, SPR=808nm) were purchased from Nanopartz (Nanopartz, Loveland, CO, USA). Their aspect ratio (AR), given by the proportion between their dimensions (length/width), is approximately 4 having therefore the ideal dimensions to be excited by the presented laser (Figure 3.4b). As already mentioned, nanorods with this AR have an absorption peak at 808 nm, and therefore, when excited by a laser in this wavelength, they will absorb the laser energy and convert it to thermal energy. An image of the nanorods, along with UV-Vis spectrum showing their SPR peak around the 808 nm are presented in Figure 6.3.

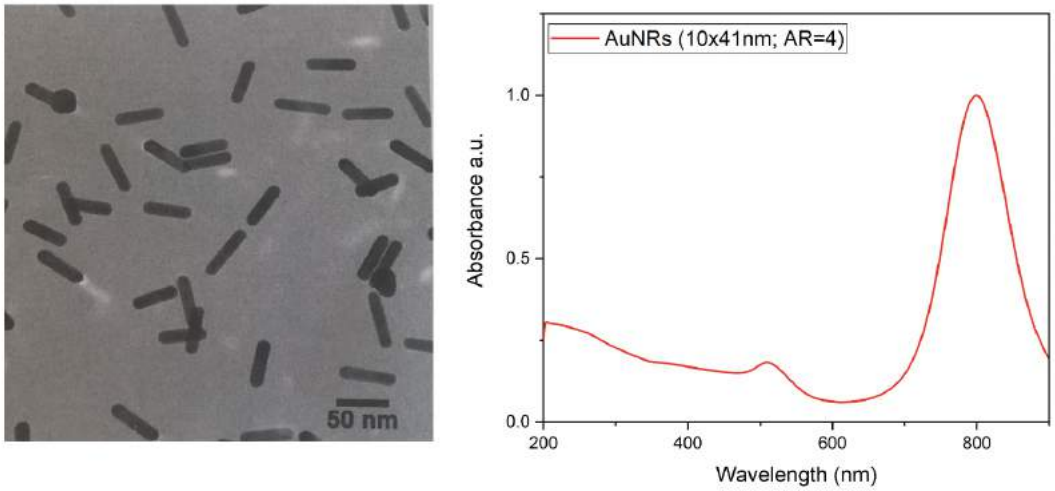

FIGURE 6.3: Gold nanorods (10x41nm) (left); UV-vis spectrum showing an SPR peak around the 808 nm (right).

During data collection several obstacles were overcame until an accurate temperature measurement was acquired. The main one was related to the thermocouple position in the solution. During the experiments it was verified that its placement had to be as centered as possible in the solution in order to obtain a temperature similar to what was being read by the IR camera. In fact, if the thermocouple was not properly centered and, for instance, was at the bottom of the cuvette it was possible to observe a discrepancy greater than 10ºC from the IR camera values. This suggests that the solution does not heat its entire volume at the same time, presenting a temperature gradient between the center of the cuvette, where the laser is focused, and the edges/walls of the same (Figure 6.4).

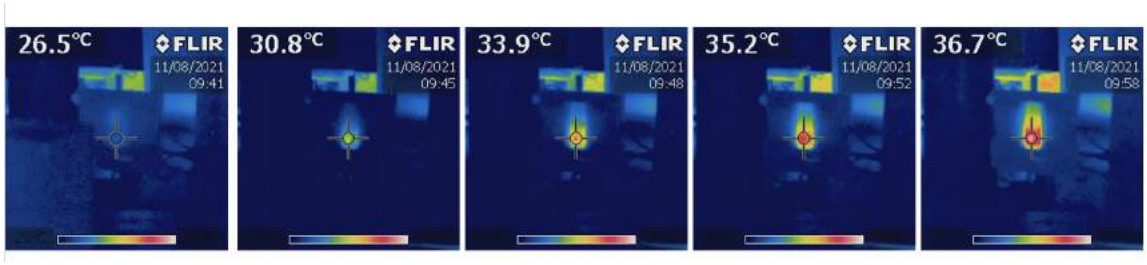

FIGURE 6.4: Infrared camera thermal images of the photo-induced heating tests.

In order to ensure that the thermocouple remained centered and immobile during data acquisition, it was secured with a pipette tip and plasticine as shown in the Figure 6.5. Before each set of measurements a test was performed to verify its position and, if necessary, adapt it until it approached the value read by the camera. Another point to be taken into account is the position of the IR camera regarding the laser, that must be placed next to and not in the opposite direction.

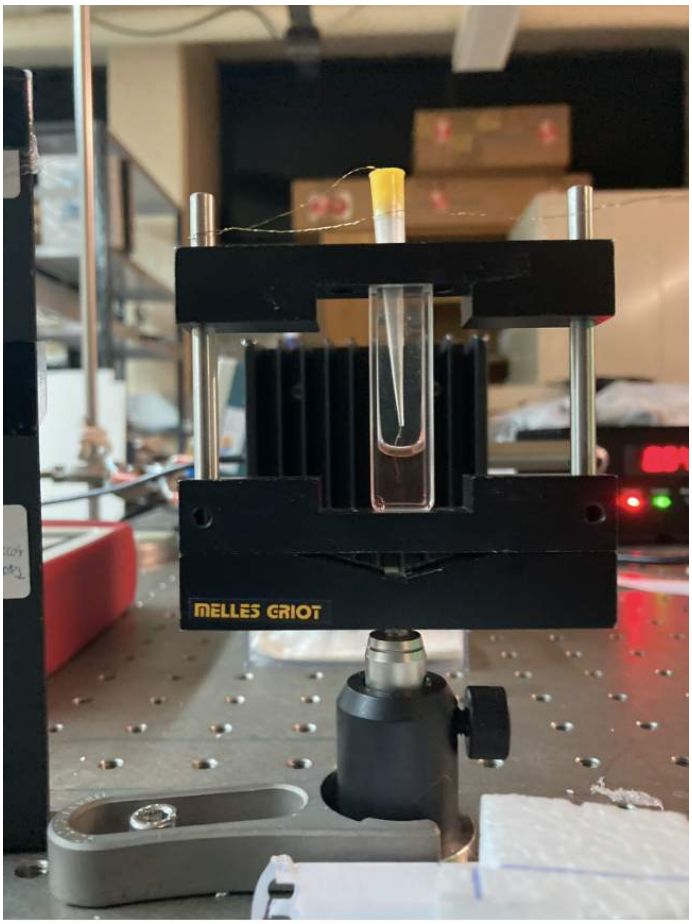

FIGURE 6.5: Thermocouple position fixed during the data acquisition.

Throughout this work the used laser output powers ranged from 0.2 to 0.8W. These values were converted into laser fluence (W/cm^2) depending on the area of the laser spot (this parameter will be discussed later). The used AuNRs concentrations were 24, 75 and 200 μg/mL in solution volumes of 0.5 and 1 mL. The measurements performed in a solution volume of 0.5 mL were made in a small volume cuvette, which has a narrower liquid support when compared to the one seen in Figure 6.5. This different cuvette required the use of a lens to focus the beam and avoid losses of intensity in its walls (Figure 6.6).

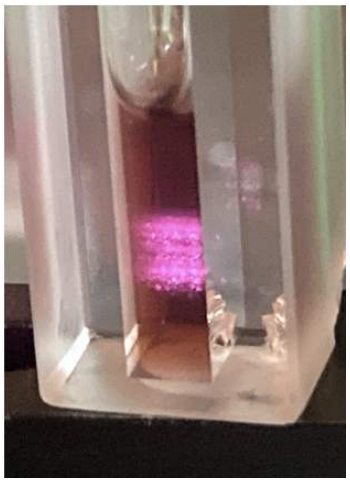

FIGURE 6.6: Laser spot area on the small volume cuvette before inserting the lens into the set-up.

6.2 Influence of the laser output power and nanorod concentration

The primary results are related to the influence of the laser output power and the gold nanorod concentration. Here, the heating curves were obtained in a $1mL$ volume solution for all the available nanorod concentrations (24, 75 and 200 μg/mL). In this case, the area of the laser spot was 0.4 cm^2, as indicated in the laser manual. For all cases, the heating curves were also obtained in an only water solution of the same volume. In this way it was possible to infer about the effective contribution of the gold nanorods in the sample heating.

The acquired data includes temperature stabilization (200 seconds), the heating of the sample until temperature saturation and the respective cooling of the same. The sample is under laser irradiation for approximately 16 minutes ($\sim$1000s). The obtained data is summarized in the Table 6.1 and the heating curves are presented in Figure 6.7.

Concentration (µg/mL)	Laser Output Power (W)	Fluence (W/cm2)	ΔT (°C)	Linear Slope	SAR (W/g)
24	0.2	0.5	8.44	0.37	64075.92
	0.4	1	15.16	0.60	104862.27
	0.6	1.5	22.33	0.87	151547.64
	0.8	2	27.38	0.92	160559.03
75	0.2	0.5	9.25	0.40	22017.45
	0.4	1	16.84	0.58	32525.42
	0.6	1.5	24.29	0.91	50982.07
	0.8	2	30.56	1.03	57640.53
200	0.2	0.5	7.91	0.09	15859.62
	0.4	1	15.19	0.17	29857.39
	0.6	1.5	22.11	0.23	39760.51
	0.8	2	28.84	0.32	55395.45

TABLE 6.1: Compiled results of the photo-induced heating tests in a sample with solution volume V=1mL; From left to right, the concentration of the AuNRs, the laser output power and the respective fluence, the temperature variation, the initial temperature as a function of time slope and the respective calculated SAR values are presented.

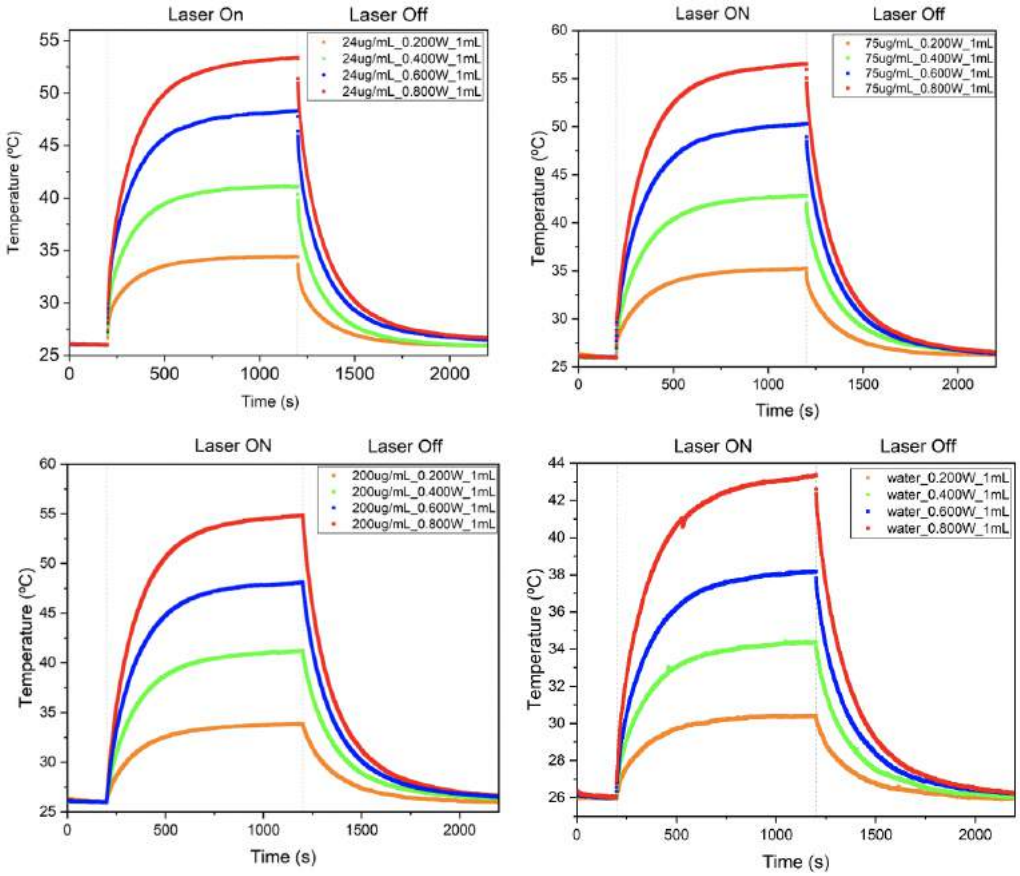

FIGURE 6.7: Heating curves obtained for all the AuNRs concentrations varying the laser output power for sample with solution volume V = 1mL.

Figure 6.8 shows an example of the heating curves with the linear fits applied in the initial temperature rise. It should be noted that the number of points chosen to apply the Linear fit was adapted to each of the curves, and therefore a fixed number of points was not maintained. In this case, the curves allowed the application of a Linear fit that encompassed the first 5 seconds of heating (10 points), however there were cases whose fit only included the first 2.5 seconds (5 points). The linear zone of the curve encompasses the time in which the heating process takes place effectively, without any loss/exchange of heat with the surroundings. In fact, the goal of this procedure is to extract the actual temperature rise caused by the laser irradiation on the nanorods. On the other hand, the saturation of the heating curve occurs generally around the 1000 seconds, meaning that at this stage the heating and the losses are already counterbalanced, keeping the temperature of the solution stable (Figure 6.7).

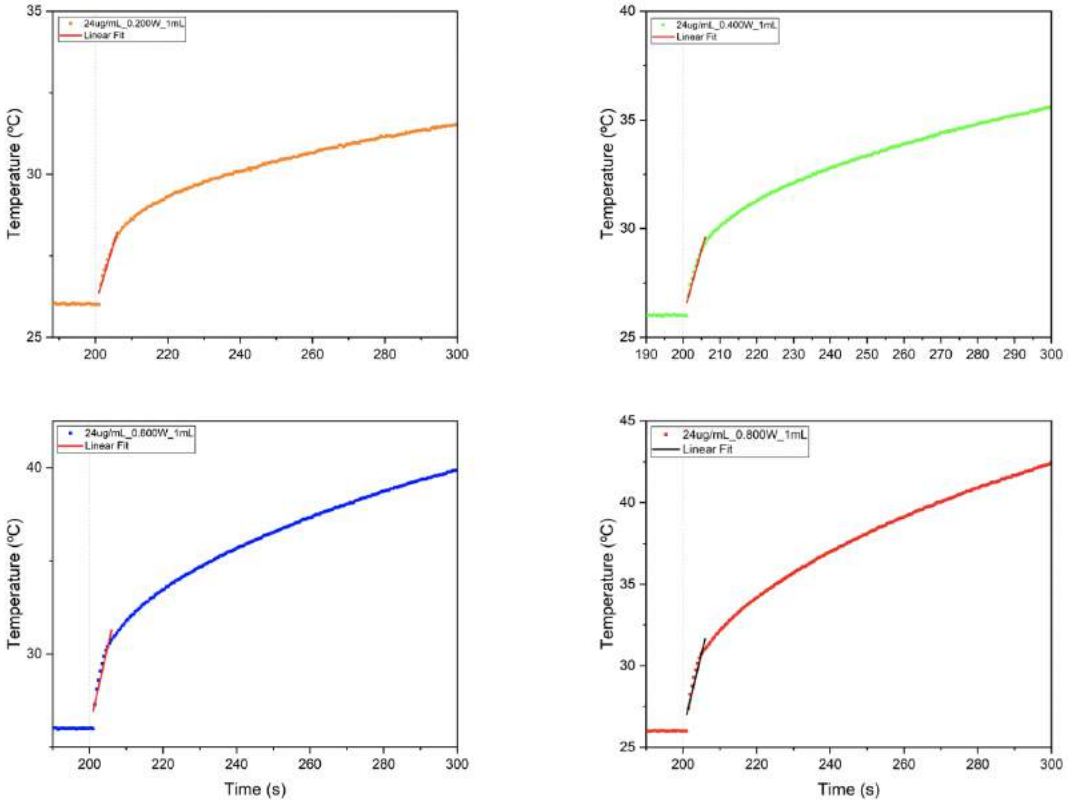

FIGURE 6.8: Example of the Linear Fits applied in the initial temperature rise for [AuNRs]= 24 μg/mL and solution volume V = 1mL.

In order to facilitate the analysis of the AuNRs performance in these experimental conditions, the temperature variation was plotted as a function of the laser output power (Figure 6.9). Here, it is possible to see that the presence of the AuNRs in the solution

significantly increase the temperature values, when compared to an only water solution with the same volume irradiated on the same experimental conditions. Observing the same Figure 6.9, it is also possible to conclude that the laser output power parameter has a clear influence on the temperature variation of the solution as the latter increases linearly with it. The highest temperature variation (ΔT = 30.56 °C) was obtained for the 75 μg/mL concentration.

Finally, an interesting conclusion is related to the fact that all concentrations have a similar temperature variation for each of used the laser output powers. The same cannot be said regarding its heating efficiency, that is evaluated as dissipated power per unit of mass of material (W/g). In this regard, taking into account the calculated SAR values, one can see that all values increase with the laser power, but the solution of 24 μg/mL clearly stands out reaching SAR values 1.6×10^5 W/g.

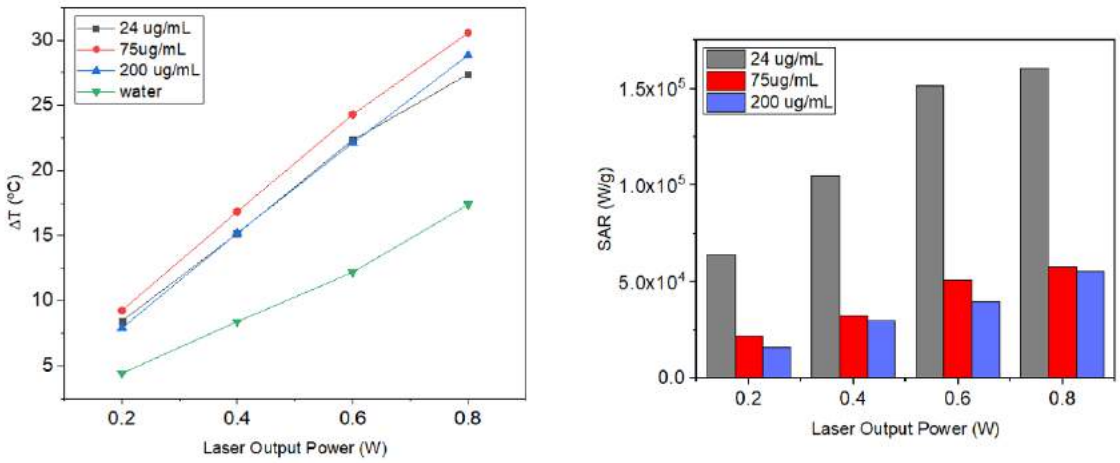

FIGURE 6.9: Temperature variation and calculated SAR values presented as a function of the Laser output power for all the AuNRs concentrations in a 1 mL volume solution.

The following analysis aims to compare the obtained experimental results with the literature, taking into account the temperature variation and the SAR calculated values as a function of nanorods concentration. In order to facilitate this comparison, the obtained experimental results will be presented in a way that matches the analysis of the selected paper published by Sangnier *et. al.* [62]. The selected paper is in line with this work, as it also evaluated the heating efficiency of AuNRs, during NIR radiation exposure. It should be noted, however, that not all experimental parameters are fully coincident. For example, while in our set-up the laser irradiates the solution laterally through the walls of the cuvette, in the paper the irradiation is done with the laser positioned directly above

the solution. Regarding the AuNRs, all the parameters were similar in both experiments, including their AR=4, 808 nm SPR peak and concentration values. Last but not least, both lasers operated at 808 nm, matching this way the AuNRs exciting conditions. The conversion of the AuNRs concentration values to mM units is presented in Table 6.2.

AuNRs Concentration (μg/mL)	AuNRs Concentration (mM)
24	0.13
75	0.39
200	1.00

TABLE 6.2: AuNR used concentrations presented in μg/mL and mM units.

The temperature variation of the sample plotted as a function of concentration is presented in Figure 6.10, for both the literature (left) and experimental (right) cases. As it possible to observe, both curves present a similar behavior suggesting that the results are in agreement with the literature. In fact, it is once again possible to verify that, regardless of the concentration used, the temperature variation does not undergo major changes. As for the variation values themselves, it is difficult to directly compare them directly since they were acquired with different laser fluences.

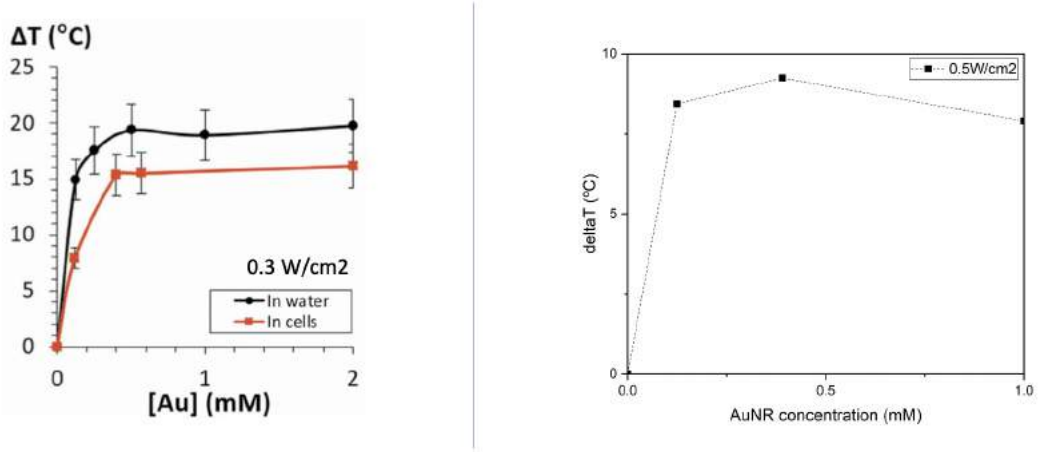

FIGURE 6.10: Temperature variation plotted as function of AuNR concentration for both the literature (left) and experimental (right) cases.

Keeping this kind of analysis, Figure 6.11 presents the SAR obtained values plotted as a function of AuNRs concentration for both the literature (left) and experimental (right) cases. Once again it is observable that the experimental results are in agreement with the literature as the curves demonstrated a similar tendency concerning the mutual dependence of these parameters.

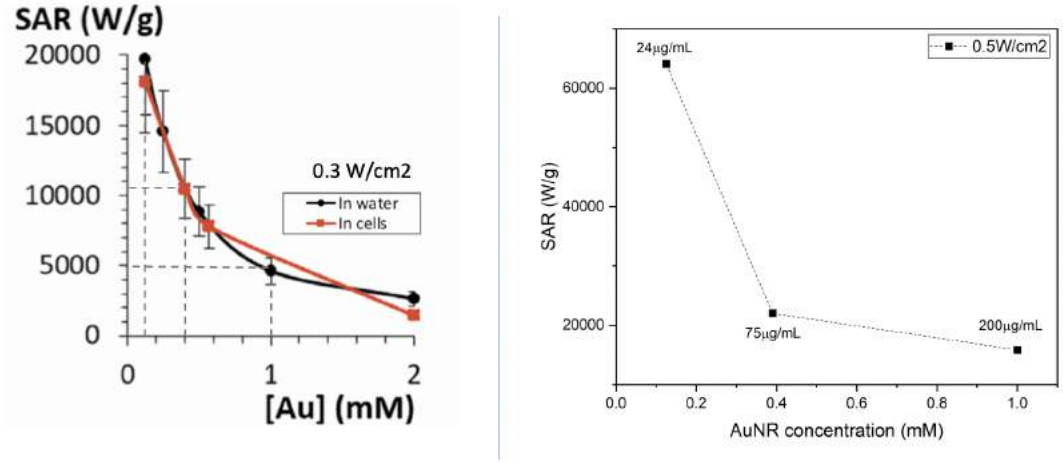

FIGURE 6.11: Obtained SAR values plotted as function of AuNR concentration for both the literature (left) and experimental (right) cases.

6.3 Influence of the laser spot area

The following results were already obtained with the focusing lens included in the set-up and therefore the size of the laser spot area was greatly reduced. In order to get an idea of this new area, and consequently of the applied fluences, its value was estimated using an appropriated camera and a program that tracked and plotted the spot dimensions. As it is possible to see in Figure 6.12, the spot presents an elliptical shape and, based on the presented dimensions, the estimated area value was $4.75 \times 10^{-4} cm^2$.

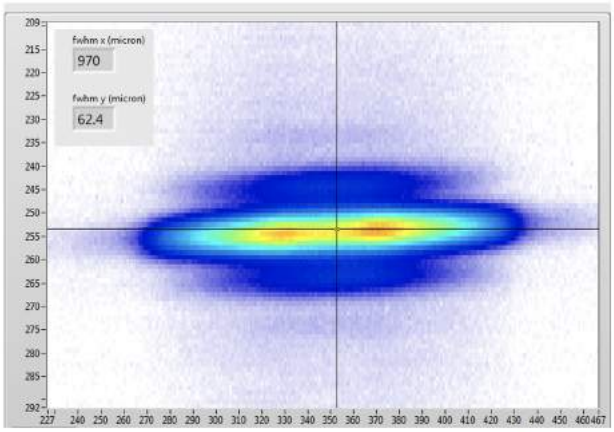

$$Laser\ Spot\ Area\ (\mu m^2) = \pi \cdot \frac{970}{2} \cdot \frac{62.4}{2} = 4.75{\times}10^{4}$$

$$Laser\ Spot\ Area\ (cm^2) = 4.75{\times}10^{-4}\ cm^2$$

FIGURE 6.12: Estimation of the laser spot area when a focusing lens is included in the set-up.

In this case, all the experimental conditions were replicated from the previous one, varying only the laser spot area which, as mentioned above, was reduced with a focusing lens. All the obtained data is summarized in Table 6.3.

Concentration (µg/mL)	Laser Output Power (W)	Fluence (W/cm2)	ΔT (ºC)	Linear Slope	SAR (W/g)
24	0.2	420.9	9.5	1.43	2.48E+05
	0.4	841.9	16.7	2.99	5.22E+05
	0.6	1262.8	23.9	4.29	7.48E+05
	0.8	1683.7	31.9	6.04	1.05E+06
75	0.2	420.9	13.0	0.89	4.96E+04
	0.4	841.9	21.3	1.52	8.47E+04
	0.6	1262.8	30.8	1.63	9.09E+04
	0.8	1683.7	37.9	2.10	1.17E+05
200	0.2	420.9	12.2	2.20	2.30E+04
	0.4	841.9	19.6	3.67	3.84E+04
	0.6	1262.8	27.4	4.53	4.74E+04
	0.8	1683.7	36.6	5.35	5.59E+04

TABLE 6.3: Compiled results of the photo-induced heating tests in a sample with solution volume V = 1 mL and with the focusing lens included in the set-up; From left to right, the concentration of the AuNRs, the laser output power and the respective fluence, the temperature variation, the initial temperature as a function of time slope and the respective calculated SAR values are presented.

With this spot area the behavior of the temperature variation was quite similar to the previous one, also increasing linearly with the laser output power. Once again the temperature variation values remained close to each other regardless of the used concentration. Concerning the SAR values, which represent the heating efficiency of the AuNRs, the same behavior is also observed although with a the greater emphasis associated with the 24 μg/mL concentration (Figure 6.13).

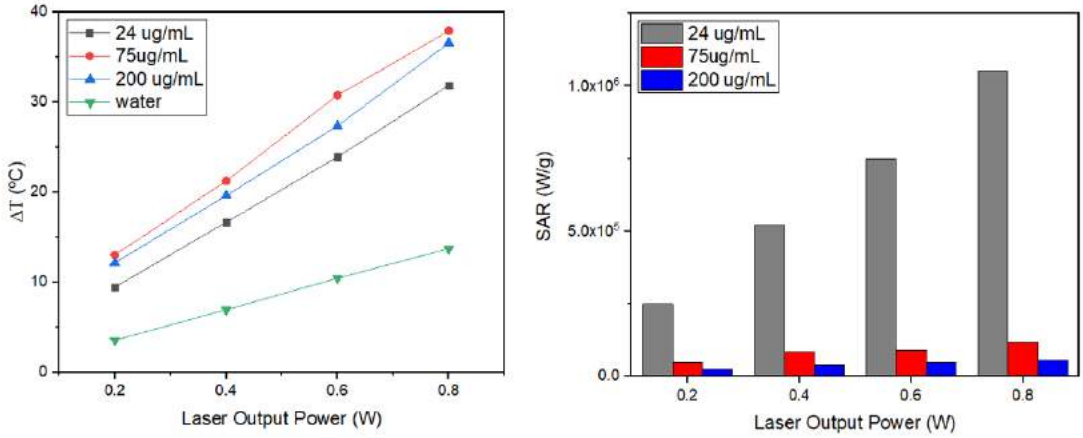

FIGURE 6.13: Temperature variation and calculated SAR values presented as a function of the laser output power for all the AuNRs concentrations in a 1 mL volume solution with the focusing lens included in the set-up.

The influence of the laser spot area regarding to temperature variation and calculated SAR values is shown in Figure 6.14. Here it is possible to observe that, in all cases, there was a higher temperature variation in the experiments in which the beam focusing lens was used. However, this variation was more evident for the 75 and 200 μg/mL concentrations that presented, respectively, a temperature variation of 7.4 and 7.8°C for the larger laser output power.

Now comparing the SAR calculated values, it is observed that in both cases the heating efficiency enlarges with the laser output power. A very evident outcome regarding the AuNRs concentration values is also visible. Here, while the lens application proves to be very relevant in the heating efficiency of the lowest concentration solution, this discrepancy is strongly attenuated as the concentration increases. This effect is especially observable for the 200 μg/mL concentration with the higher laser output power, in which the heating efficiency is very similar.

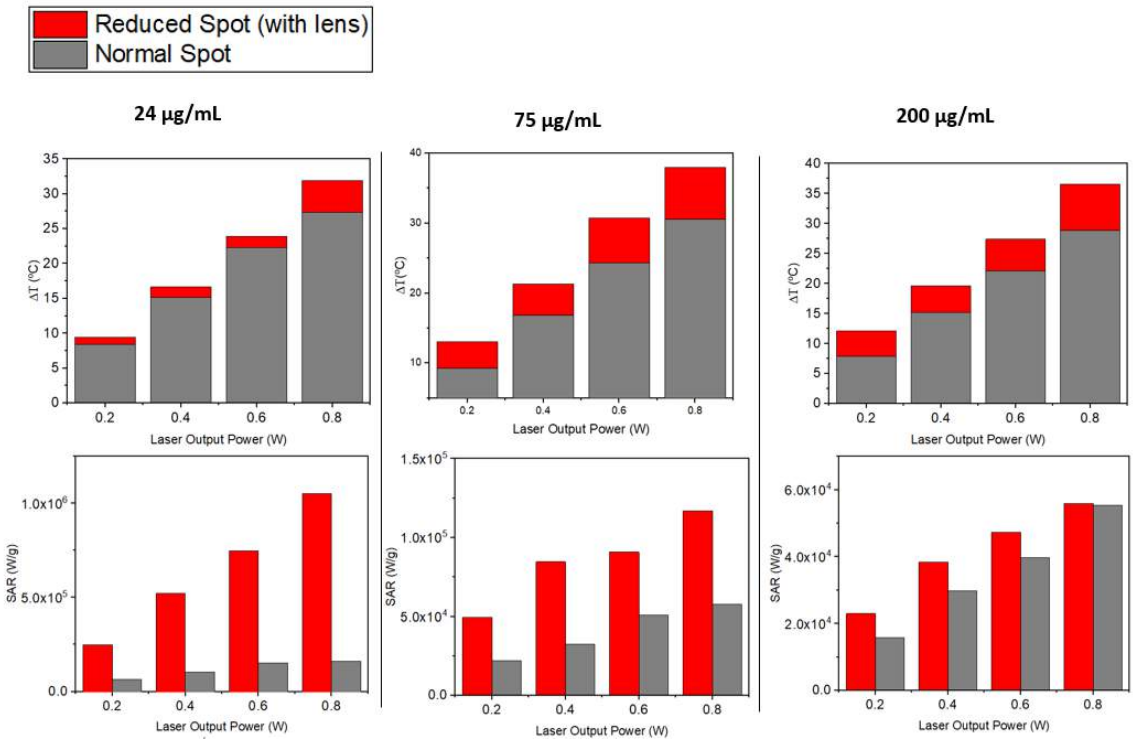

FIGURE 6.14: Influence of the laser spot area in the temperature variation and on the SAR (W/g) calculated values

It is important to refer that the insertion of the focusing lens in the set-up has a large impact on the laser spot area, that consequently reflects in large variations in the laser fluence. In this case, as the objective was to evaluate the influence of this area, the laser output powers values of the previous set of measurements were kept fixed. However, this led to laser fluence values two order of magnitude larger when compared to the ones obtained without the lens, reaching the 1683 W/cm^2. Considering the fact that preclinical PTT studies generally use laser powers densities in the 1-4 W/cm^2 range, it is important to refer that the obtained fluence values are excessive, so it would be necessary to adapt the laser output power values in order to maintain an adequate proportion between the latter the area, so that the fluence values are kept in the same value range.

6.4 Influence of the solution volume

Finally, the acquired data related to the heating of a sample with volume of 0.5 mL is presented. All the other experimental parameters were kept the same regarding the previous experiment. The obtained data is summarized in Table 6.4.

Concentration (µg/mL)	Laser Output Power (W)	Fluence (W/cm2)	ΔT (°C)	Linear Slope	SAR (W/g)
24	0.2	420.9	7.2	0.38	3.28E+04
	0.4	841.9	13.2	1.00	8.72E+04
	0.6	1262.8	18.9	1.53	1.33E+05
	0.8	1683.7	23.2	2.17	1.89E+05
75	0.2	420.9	8.3	0.19	5.27E+03
	0.4	841.9	15.0	0.41	1.15E+04
	0.6	1262.8	22.3	1.02	2.84E+04
	0.8	1683.7	29.5	2.46	6.85E+04
200	0.2	420.9	7.5	0.09	8.97E+02
	0.4	841.9	14.5	0.16	1.69E+03
	0.6	1262.8	21.3	0.22	2.34E+03
	0.8	1683.7	27.9	0.30	3.15E+03

TABLE 6.4: Compiled results of the photo-induced heating tests in a sample with solution volume V=0.5mL and with the focusing lens included in the set-up; From left to right, the concentration of the AuNRs, the laser output power and the respective fluence, the temperature variation, the initial temperature as a function of time slope and the respective calculated SAR values are presented.

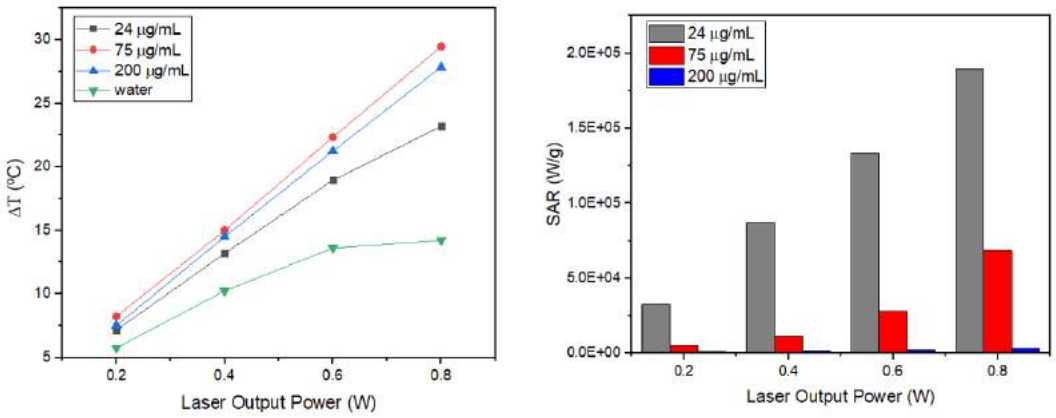

FIGURE 6.15: Temperature variation and calculated SAR values presented as a function of the Laser output power for all the nanorods concentrations in a solution with volume V = 0.5mL with the focusing lens included in the set-up.

The photo-induced temperature variation and calculated SAR values, as a function of laser output power, for a solution volume of 0.5mL are presented in Figure 6.15. Keeping the tendency verified in all previous experimental conditions, the temperature variation increases linearly with the laser output power and, once again the temperature variation values remained close to each other regardless of the used concentration. Regarding the SAR values the same behavior is also observed, although with a greater discrepancy between the 75 and 200 μg/mL concentrations. The lowest concentration remains firmly in the lead concerning the heating efficiency.

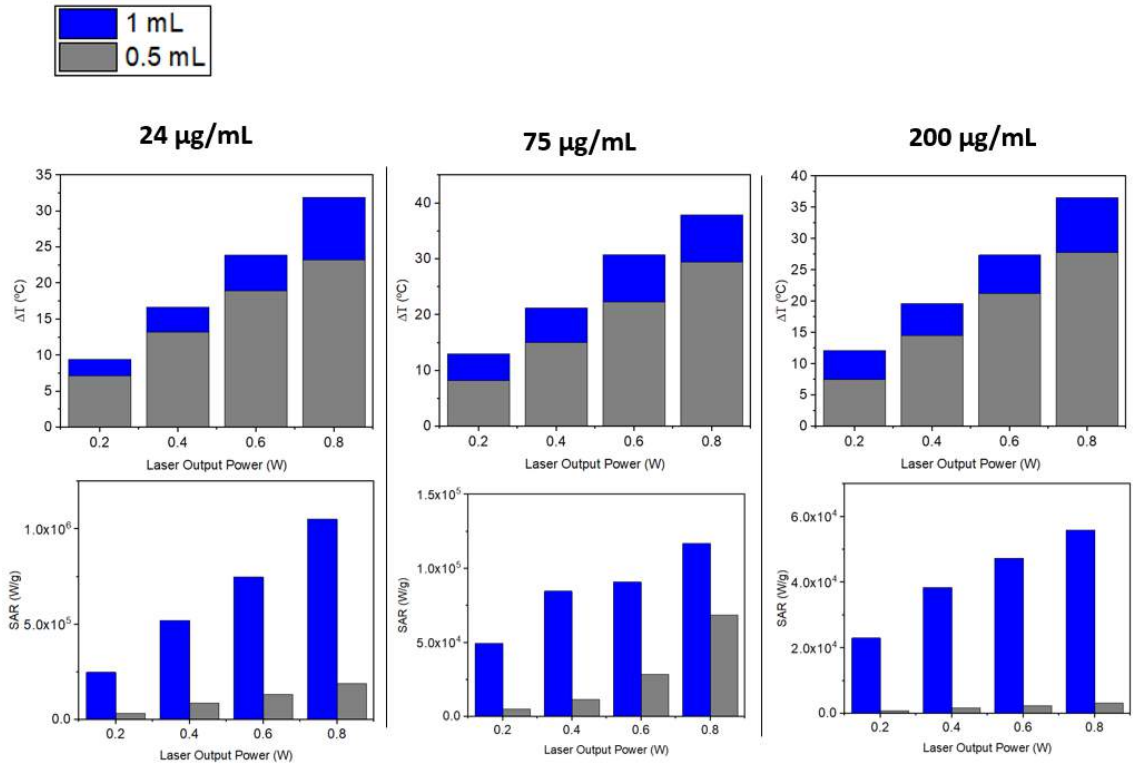

FIGURE 6.16: Influence of the solution volume in the temperature variation and SAR (W/g) calculated values

Now comparing the effect associated with volume reduction related to the variation in temperature and SAR values (Figure 6.16). Here, a constant behavior with respect to temperature variation is observed, showing in all cases higher values in the 1mL solution. Taking into account the heating efficiency, the 1 mL solution proved to be more effective when compared to the 0.5 mL solution. This effect was more evident for the concentration of 200, but a smaller discrepancy is verified for the 75μg/mL.

Chapter 7

Conclusions/Future Work

The Laser Ablation in Liquids technique has proven to be very effective for the production of nanoparticles. As it was demonstrated by the results presented in Chapter 5, nanoparticles were successfully synthesized in several configurations. One common result regarding all the successful experiments is related to the nanoparticle morphology in which a spherical shape was always obtained. Throughout this work, the influence of several experimental parameters was investigated. The main ones were the type of target and liquid solution. Starting in experiments with a bulk target, single-iron and single-gold nanoparticles were obtained, this way fulfilling the first objective of this work. Although in the case of iron the particles presented an average size above the intended ($\sim$368nm), its dimensions were easily reduced with the application of β-CD in the liquid solution. In the latter, the average size was $\sim$ 43 nm, being therefore one order of magnitude smaller. The application of β-CDs also influenced the size distribution values, presenting a narrower distribution when compared to the one obtained in the ablation of the iron target in ethanol.

Moving on to the laser ablation in thin film targets, the main conclusion is the fact that it is effectively possible to synthesize nanoparticles composed simultaneously by the two elements with a femtosecond pulsed laser. Even though the latter was only achieved by ablating the target with three deposited layers (Gold-Iron-Gold), the 2-layer ablation of the Iron-Gold case also allow the synthesis of nanoparticles. Regarding the liquid solution, acetone was the most outstanding media, remaining stable for a longer time (12 days at least).

The main focus of this work, and the biggest challenge as well, was related to the fact that this technique was investigated practically from scratch. In fact, it has never

been used in our department, at least for this purpose. Hence, a lot of time and effort was employed in order to find the ideal parameters that allowed a successful synthesis of such nanoparticles. Throughout all the ablation attempts the ablation process was optimized. Hereupon, this matter of trial and error allowed us to gain the experience regarding the experimental part of the LAL technique.

In order to obtain a full understanding regarding the dependence of the morphology and characteristics of the particles synthesized by Laser Ablation in Liquids, it is still necessary to evaluate the influence of several other experimental parameters, such as the thickness of the layers deposited on top of the glass substrate or the thickness of the liquid solution above the target, that in this work was fixed in the 3-5mm range. Regarding the laser, parameters such as the pulse energy or the repetition rate are worth to be explored. In addition to those mentioned, it would also be interesting to put the fluid in motion, in order to remove the suspended particles from the laser front.

Future tasks regarding this part of the work may include a deeper investigation, namely through TEM, of whether a Fe@Au core-shell morphology was actually obtained. Beyond that, try to achieve even more complex structures by reshaping the synthesized particles, in order to obtain a cylindrical Fe@Au core-shell morphology. This reshaping can be done during laser ablation with the help of magnetic fields [63]. Last but not least, perform a detailed analysis regarding the heating efficiency of such nanoparticles when stimulated with alternating magnetic fields (magnetic hyperthermia).

Concerning the second part of this work, a detailed analysis of the performance of nanorods during exposure to NIR radiation was carried out taking into account the variation of several experimental parameters such as the laser output power, laser spot area, nanorod concentration and volume of the sample. The photo-induced heating tests revealed, in all cases, a significant temperature increase in solutions with nanorods (ΔT=30.5°C) when compared to an aqueous solution irradiated under the same conditions (ΔT=17.3°C). This result confirms that these nanostructures, acting as photothermal agents, effectively absorbed the laser energy and converted it into thermal energy. It was also verified that, regardless of the concentration used, the maximum reached temperature was similar. The same can not be said regarding its heating efficiency, evaluated as dissipated power per unit of mass of material. In this regard, taking into account the calculated SAR values, the lowest concentration showed the most promising results. This outcome is very much important, with a special relevance for in-vivo tests, where the toxicity related to high

nanoparticles concentration is often reported as a problem. Lastly, the laser output power proved to be the key parameter in global heating of the sample. In all evaluated cases, a linearity between this parameter and the maximum temperature reached was verified. Future tasks regarding this part of the work include a similar analysis with gold nanorods with different dimensions while keeping the aspect ratio value fixed, proceeding the investigation regarding the influence of laser spot area and lastly, to complement this study with COMSOL simulations regarding the heat exchanges between nanoparticles-liquid, liquid-cuvette and cuvette-air.

Bibliography

[1] [Online]. Available: https://www.iarc.who.int/featured-news/latest-global-cancer-data-cancer-burden-rises-to-18-1-million-new-cases-and-9-6-million-cancer-deaths-in-2018/ [Cited on page 1.]

[2] J. F. Hainfeld *et al.*, "Gold nanoparticle hyperthermia reduces radiotherapy dose," *Nanomedicine: Nanotechnology, Biology and Medicine*, vol. 10, no. 8, p. 1609–1617, 2014. [Cited on page 1.]

[3] M. Bañobre-López *et al.*, "Magnetic nanoparticle-based hyperthermia for cancer treatment," *Reports of Practical Oncology Radiotherapy*, vol. 18, no. 6, p. 397–400, 2013. [Cited on pages 1 and 2.]

[4] C. Xu *et al.*, "New forms of superparamagnetic nanoparticles for biomedical applications," *Advanced Drug Delivery Reviews*, vol. 65, no. 5, p. 732–743, 2013. [Cited on pages 1 and 4.]

[5] A. Lu *et al.*, "Magnetic nanoparticles: Synthesis, protection, functionalization, and application," *Angewandte Chemie International Edition*, vol. 46, no. 8, pp. 1222–1244, 2007. [Cited on pages xix, 2, 13, 16, and 42.]

[6] L. Peixoto *et al.*, "Magnetic nanostructures for emerging biomedical applications," *Applied Physics Reviews*, vol. 7, no. 1, p. 011310, 2020. [Cited on pages 2, 3, and 4.]

[7] X. Li *et al*, "Current investigations into magnetic nanoparticles for biomedical applications," *Journal of Biomedical Materials Research Part A*, vol. 104, no. 5, p. 1285–1296, 2016. [Cited on pages 2 and 3.]

[8] C. C. Berry *et al*, "Functionalisation of magnetic nanoparticles for applications in biomedicine," *Journal of Physics D: Applied Physics*, vol. 36, no. 13, 2003. [Cited on page 3.]

[9] A. Shapira *et al*, "Nanomedicine for targeted cancer therapy: Towards the overcoming of drug resistance," *Drug Resistance Updates*, vol. 14, no. 3, p. 150–163, 2011. [Cited on page 4.]

[10] J.-E. Kim *et al*, "Magnetic nanoparticles: an update of application for drug delivery and possible toxic effects," *Archives of Toxicology*, vol. 86, no. 5, p. 685–700, 2011. [Cited on page 4.]

[11] X. Mou *et al*, "Applications of magnetic nanoparticles in targeted drug delivery system," *Journal of Nanoscience and Nanotechnology*, vol. 15, no. 1, pp. 54–62, 2015. [Cited on page 4.]

[12] G. A. Passos, *Principles of nanomagnetism*. Springer, 2018. [Cited on page 5.]

[13] V. Marghussian, *Nano-glass ceramics: processing, properties and applications*. William Andrew, 2015. [Cited on pages 6, 8, 9, and 15.]

[14] Z. Hedayatnasab, F. Abnisa, and W. M. A. W. Daud, "Review on magnetic nanoparticles for magnetic nanofluid hyperthermia application," *Materials & Design*, vol. 123, p. 174–196, 2017. [Cited on pages 6 and 7.]

[15] Z. Shaterabadi, G. Nabiyouni, and M. Soleymani, "Physics responsible for heating efficiency and self-controlled temperature rise of magnetic nanoparticles in magnetic hyperthermia therapy," *Progress in Biophysics and Molecular Biology*, vol. 133, p. 9–19, 2018. [Cited on pages xiii, 7, 10, 15, 16, and 17.]

[16] B. D. Cullity and C. D. Graham, *Introduction to magnetic materials*. IEEE/Wiley, 2009. [Cited on pages xiii, 8, 11, and 12.]

[17] A. G. Kolhatkar, D. Jamison, A. C.and Litvinov, R. C. Willson, and T. R. Lee, "Tuning the magnetic properties of nanoparticles," *International journal of molecular sciences*, vol. 14(8), p. 15977–16009, 2013. [Cited on pages xiii and 8.]

[18] A. Arora, W. Kuch, and F. Noltimg, "Optical and electric field control of magnetism," Ph.D. dissertation, 2018. [Cited on pages xiii and 9.]

[19] G. A. P. Ribeiro, "As propriedades magnéticas da matéria: um primeiro contato," *Revista Brasileira de Ensino de Física*, vol. 22, p. 299–305, 2000. [Cited on page 10.]

[20] J. M. D. Coey, *Magnetism and Magnetic Materials*. Cambridge University Press, 2009. [Cited on pages xiii, 10, 11, and 12.]

[21] M. Montazer and T. Harifi, *Nanofinishing of Textile Materials*. Woodhead Publishing, an imprint of Elsevier, 2018. [Cited on pages xiii, 12, and 15.]

[22] V. V. Mody, A. Singh, and B. Wesley, "Basics of magnetic nanoparticles for their application in the field of magnetic fluid hyperthermia," *nano Online*, 2016. [Cited on pages xiii, 13, and 14.]

[23] V. F. Cardoso, A. Francesko, C. Ribeiro, M. Bañobre-López, P. Martins, and S. Lanceros-Mendez, "Advances in magnetic nanoparticles for biomedical applications," *Adv. Healthcare Materials*, p. 1700845, 2017. [Cited on page 14.]

[24] I. Sharifi, H. Shokrollahi, and S. Amiri, "Ferrite-based magnetic nanofluids used in hyperthermia applications," *Journal of Magnetism and Magnetic Materials*, vol. 324, no. 6, p. 903–915, 2012. [Cited on page 14.]

[25] H. Urs, *Scientific and clinical applications of magnetic carriers*. Plenum Press, 1997. [Cited on page 15.]

[26] E. P. Gubin, *Magnetic Nanoparticles*. John Wiley & Sons, 2009. [Cited on page 16.]

[27] A. Giustini, *Magnetic nanoparticle surface coating and tumor microenvironment alterations for improved cancer treatment efficacy*, 2010. [Cited on pages xiii, 16, and 27.]

[28] R. Rosensweig, "Heating magnetic fluid with alternating magnetic field," *Journal of Magnetism and Magnetic Materials*, vol. 252, p. 370–374, 2002. [Cited on page 18.]

[29] X. Liu, Y. Zhang, Y. Wang, W. Zhu, G. Li, X. Ma, Y. Zhang, S. Chen, S. Tiwari, K. Shi, and et al., "Comprehensive understanding of magnetic hyperthermia for improving antitumor therapeutic efficacy," *Theranostics*, vol. 10, no. 8, p. 3793–3815, 2020. [Cited on pages xiii, 18, 26, and 28.]

[30] J. Beik, Z. Abed, F. S. Ghoreishi, S. Hosseini-Nami, S. Mehrzadi, A. Shakeri-Zadeh, and S. K. Kamrava, "Nanotechnology in hyperthermia cancer therapy: From fundamental principles to advanced applications," *Journal of Controlled Release*, vol. 235, p. 205–221, 2016. [Cited on pages xiii, 19, and 20.]

[31] A. E. et al, "Magnetic (hyper)thermia or photothermia? progressive comparison of iron oxide and gold nanoparticles heating in water, in cells, and in vivo," *Adv. Funct. Mater.*, p. 1803660 (1 of 16), 2018. [Cited on pages xiii, 19, 21, 24, and 28.]

[32] A. Granja *et al.*, "Gold nanostructures as mediators of hyperthermia therapies in breast cancer, biochemical pharmacology," *Journal Pre-proofs*, vol. 190, p. 114639, 2021. [Cited on pages 19, 22, 23, and 25.]

[33] Y. Li, U. Dhawan, H. Wang, X. Liu, H. Ku, M. Tsai, H. Yen, and R. Chung, "Theranostic iron@gold core–shell nanoparticles for simultaneous hyperthermia-chemotherapy upon photo-stimulation," *Particle & Particle Systems Characterization*, vol. 36, no. 6, p. 1800419, 2019. [Cited on page 20.]

[34] P. Lemal, C. Geers, B. Rothen-Rutishauser, M. Lattuada, and A. Petri-Fink, "Measuring the heating power of magnetic nanoparticles: an overview of currently used methods," *Materials Today: Proceedings*, vol. 4, 2017. [Cited on pages 21 and 22.]

[35] S. Anand, T. Chan, T. Hasan, and E. Maytin, "Current prospects for treatment of solid tumors via photodynamic, photothermal, or ionizing radiation therapies combined with immune checkpoint inhibition (a review)," *Pharmaceuticals*, vol. 14, no. 5, p. 447, 2021. [Cited on page 23.]

[36] Y. H. Shuren Wang, "Photothermal therapy based on magnetic nanoparticles in cancer," *J. Appl. Phys*, vol. 130, p. 070902, 2021. [Cited on page 23.]

[37] L. Cheng, C. Wang, L. Feng, K. Yang, and Z. Liu, "Functional nanomaterials for phototherapies of cancer," *Chemical Reviews*, vol. 114, no. 21, p. 10869–10939, 2014. [Cited on pages xiii and 25.]

[38] A. J. Gormley, K. Greish, A. Ray, R. Robinson, J. A. Gustafson, and H. Ghandehari, "Gold nanorod mediated plasmonic photothermal therapy: A tool to enhance macromolecular delivery," *International Journal of Pharmaceutics*, vol. 415, no. 1-2, p. 315–318, 2011. [Cited on pages xiii and 25.]

[39] B. Mehdaoui, A. Meffre, J. Carrey, S. Lachaize, L.-M. Lacroix, M. Gougeon, B. Chaudret, and M. Respaud, "Optimal size of nanoparticles for magnetic hyperthermia: A combined theoretical and experimental study," *Advanced Functional Materials*, vol. 21, no. 23, p. 4573–4581, 2011. [Cited on pages 25, 26, and 27.]

[40] "MAg.Hyperthermia kernel description," https://www.york.ac.uk/physics/research/magnetic-nanoparticle-hyperthermia-magnanotherm/introduction/, accessed: 2021-09. [Cited on pages xiii and 26.]

[41] K. Simeonidis, C. Martinez-Boubeta, L. Balcells, C. Monty, G. Stavropoulos, M. Mitrakas, A. Matsakidou, G. Vourlias, and M. Angelakeris, "Fe-based nanoparticles as tunable magnetic particle hyperthermia agents," *Journal of Applied Physics*, vol. 114, no. 10, p. 103904, 2013. [Cited on page 27.]

[42] S.-J. Cho, S. M. Kauzlarich, J. Olamit, K. Liu, F. Grandjean, L. Rebbouh, and G. J. Long, "Characterization and magnetic properties of core/shell structured fe/au nanoparticles," *Journal of Applied Physics*, vol. 95, no. 11, p. 6804–6806, 2004. [Cited on page 28.]

[43] A. Tymoczko *et al.*, "One-step synthesis of fe–au core–shell magnetic-plasmonic nanoparticles driven by interface energy minimization," *Nanoscale Horizons*, vol. 4, no. 6, p. 1326–1332, 2019. [Cited on pages xiv, 28, and 38.]

[44] V. Amendola and M. Meneghetti, "What controls the composition and the structure of nanomaterials generated by laser ablation in liquid solution?" *Physical Chemistry Chemical Physics*, 2012. [Cited on pages xiv, 31, 33, and 34.]

[45] N. Semaltianos, *Nanoparticles by Laser Ablation of Bulk Target Materials in Liquids - Handbook of Nanoparticles*. Springer, 2016. [Cited on pages xiii, 31, 32, and 34.]

[46] V. Amendola *et al.*, "Laser ablation synthesis in solution and size manipulation of noble metal nanoparticles," *Physical Chemistry Chemical Physics*, vol. 11, no. 20, p. 3805, 2009. [Cited on pages 31 and 35.]

[47] S. Hashmi and B. S. Yilbas, *Comprehensive materials processing*. Elsevier, 2014. [Cited on pages xiii, 32, 33, 36, and 37.]

[48] B. Verhoff *et al.*, "Dynamics of femto- and nanosecond laser ablation plumes investigated using optical emission spectroscopy," *Journal of Applied Physics*, vol. 112, no. 9, p. 093303, 2012. [Cited on page 35.]

[49] S. Musazzi and U. Perini, *Laser-Induced Breakdown Spectroscopy Theory and Applications*. Springer Berlin, 2016. [Cited on pages xiv, 35, and 36.]

[50] V. Amendola *et al.*, "Formation of alloy nanoparticles by laser ablation of au/fe multilayer films in liquid environment," *Journal of Colloid and Interface Science*, vol. 489, p. 18–27, 2017. [Cited on pages xiv, 37, and 38.]

[51] W. Zhou, R. Apkarian, Z. L. Wang, and D. Joy, *Fundamentals of Scanning Electron Microscopy (SEM)*. Springer New York, 2007. [Cited on pages 39 and 40.]

[52] S. Carrara, "Towards new efficient nanostructured hybrid materials for ecl applications," Ph.D. dissertation, 04 2017. [Cited on pages xiv and 39.]

[53] [Online]. Available: https://en.wikipedia.org/wiki/Energy-dispersive_X-ray_spectroscopy [Cited on pages xiv and 41.]

[54] M. Buchner *et al.*, "Tutorial: Basic principles, limits of detection, and pitfalls of highly sensitive squid magnetometry for nanomagnetism and spintronics," *Applied Physics A*, vol. 124, no. 16, p. 161101, 2018. [Cited on page 41.]

[55] C. Pereira *et al.*, "Superparamagnetic mfe2o4 (m = fe, co, mn) nanoparticles: Tuning the particle size and magnetic properties through a novel one-step coprecipitation route," *Chemistry of Materials*, vol. 24, no. 8, p. 1496–1504, 2012. [Cited on pages xiv and 42.]

[56] Q. Abbas, "Journal of nanomaterials molecular nanotechnology understanding the uv-vis spectroscopy for nanoparticles," *Journal of Nanomaterials Molecular Nanotechnology*, vol. 8, p. 3, 2019. [Cited on pages 43 and 44.]

[57] W. Mäntele and E. Deniz, "Uv–vis absorption spectroscopy: Lambert-beer reloaded," *Spectrochimica Acta Part A: Molecular and Biomolecular Spectroscopy*, vol. 173, p. 965–968, 2017. [Cited on pages 43 and 44.]

[58] M. I. Ltd, *Zetasizer Nano User Manual*, 2013. [Cited on pages xiv, 44, 45, and 46.]

[59] H. Danan, A. Herr, and A. J. P. Meyer, "New determinations of the saturation magnetization of nickel and iron," *Journal of Applied Physics*, vol. 39, no. 2, p. 669–670, 1968. [Cited on page 49.]

[60] J.-P. S. et al, "Stabilization and size control of gold nanoparticles during laser ablation in aqueous cyclodextrins," *J. AM. CHEM. SOC*, vol. 126, pp. 7176–7177, 2004. [Cited on pages 53 and 54.]

[61] J.-P. Sylvestre *et al.*, "Femtosecond laser ablation of gold in water: influence of the laser-produced plasma on the nanoparticle size distribution," *Applied Physics A*, vol. 80, no. 4, p. 753–758, 2005. [Cited on page 60.]

[62] A. P. Sangnier, A. V. D. Walle, R. Aufaure, M. Fradet, L. Motte, E. Guénin, Y. Lalatonne, and C. Wilhelm, "Photothermal therapy: Endosomal confinement of gold nanospheres, nanorods, and nanoraspberries governs their photothermal identity and is beneficial for cancer cell therapy (adv. biosys. 4/2020)," *Advanced Biosystems*, vol. 4, no. 4, p. 2070042, 2020. [Cited on page 86.]

[63] G. Shafeev, I. Rakov, K. Ayyyzhy, G. Mikhailova, A. Troitskii, and O. Uvarov, "Generation of au nanorods by laser ablation in liquid and their further elongation in external magnetic field," *Applied Surface Science*, vol. 466, p. 477–482, 2019. [Cited on page 96.]